



**University of
Zurich**^{UZH}

Sub-Seasonal and Interannual Changes in the Bare- Ice Albedo of European Alpine Glaciers

GEO 511 Master's Thesis

Author

Florent Rouilly
16-921-140

Supervised by

Dr. Hendrik Wulf
Dr. Kathrin Naegeli

Faculty representative

Prof. Dr. Livia Piermattei

30.01.2025

Department of Geography, University of Zurich

Abstract

European Alpine glaciers have been melting for decades, accelerated by a warming climate. Predictions based on mass balance models show that almost all glaciers will be gone by 2100. Bare-ice albedo, although highly variable in space and time, is often assumed to be a constant in such models. This thesis presents an approach to a comprehensive analysis of European Alpine glaciers. The correlation of albedo between ground measurements, Landsat 8/9, and Sentinel 2 satellites is analysed. The results show that satellites are well suited to measure ground albedo and the combination of Landsat 8/9 and Sentinel 2 is encouraged to improve data availability. Bare-ice albedo is investigated for sub-seasonal variability and interannual trends. Sub-seasonal variability is found on many glaciers during particularly warm summers, and only a few interannual trends are detected, some of which seem to confirm the reported surface darkening on glaciers. Finally, various surface properties and meteorological factors and their influence as drivers of bare-ice albedo change are investigated. Mean air temperature, nighttime minimum and maximum air temperature, and cumulative shortwave radiation are found to correlate best with bare-ice albedo change on European Alpine glaciers. Satellite monitoring of glaciers proves to be a valuable tool due to the accessibility of the data and the possibility to perform large-scale analyses.

Acknowledgements

I want to thank everyone around me for their support during my Master's thesis. Thank you for the advice and encouragement, as well as the distraction when I needed a break. I want to thank a few people in particular for their support:

My supervisors, Dr. Hendrik Wulf and Dr. Kathrin Naegeli, for your great support throughout all stages of my thesis. I greatly appreciate the time and effort you put into helping me develop ideas, discussing and answering my questions, and giving me constructive feedback.

Prof. Dr. Livia Piermattei for giving me the opportunity to write my thesis at your Chair of Remote Sensing of Environmental Changes.

My lecturers, Stephanie and Seraina, for reading my thesis in the final stages and giving me comments and corrections.

And Françoise, Pascale, and Fabian for keeping me company by working alongside me in the library or at home.

Table of Contents

Abstract	I
Acknowledgements	II
Table of Contents	II
List of Figures	VII
List of Tables	VIII
Abbreviations	IX
1 Introduction	1
2 Theory	3
2.1 Glacier characteristics	3
2.2 Surface energy balance	4
2.3 Glacier albedo	5
2.4 Satellite remote sensing for glacier monitoring	6
3 Study Area	8
4 Data	12
4.1 Automatic weather stations	12
4.1.1 Glacier de la Plaine Morte	12
4.1.1.1 Ablation periods 2014–2017	12
4.1.1.2 Fixed station 2016–present	13
4.1.2 Weissseespitze/Gepatschferner	14
4.1.3 Hintereisferner	14
4.2 Satellites	15
4.2.1 Landsat 8	16
4.2.2 Sentinel 2	16
4.2.3 Landsat 9	17
4.2.4 Data availability	17

5	Methods	20
5.1	AWS data	20
5.1.1	Quality control	20
5.1.2	Albedo and drivers of albedo change	21
5.2	Satellite data	21
5.2.1	Google Earth Engine	21
5.2.1.1	Cloud and cloud shadow detection	21
5.2.1.2	Classification	22
5.2.1.3	Narrowband to broadband shortwave albedo conversions	23
5.2.2	Export	24
5.2.2.1	Albedo/land surface temperature at the AWS location	24
5.2.2.2	Albedo pixel values for the whole glacier	25
5.2.2.3	Mean albedo values of elevation bands	25
5.3	Statistical analysis	27
5.3.1	RQ1: Albedo comparison	27
5.3.1.1	AWS albedo vs. satellite albedo	27
5.3.1.2	L8/9 albedo vs. S2 albedo	27
5.3.2	RQ2: Trend analysis	27
5.3.2.1	Sub-seasonal trends	27
5.3.2.2	Interannual trends	27
5.3.3	RQ3: Drivers of albedo change	28
6	Results	29
6.1	RQ1: Albedo comparison	29
6.1.1	AWS albedo vs. satellite albedo	29
6.1.1.1	AWS Glacier de la Plaine Morte	29
6.1.1.2	AWS Weissseespitze/Gepatschferner	31
6.1.2	L8/9 albedo vs. S2 albedo	32
6.2	RQ2: Trend analysis	36
6.2.1	Sub-seasonal trends	36
6.2.2	Interannual trends	38
6.3	RQ3: Drivers of albedo change	39
6.3.1	AWS Glacier de la Plaine Morte	39
6.3.2	AWS Hintereisferner	41
7	Discussion	43
7.1	RQ1: Albedo comparison	43
7.1.1	AWS albedo vs. satellite albedo	43
7.1.2	L8/9 albedo vs. S2 albedo	45
7.2	RQ2: Trend analysis	46
7.2.1	Sub-seasonal trends	46
7.2.2	Interannual trends	48

7.3	RQ3: Driver of albedo change	49
7.3.1	Land Surface Temperature	50
7.3.2	Air temperature	50
7.3.3	SW radiation	52
7.4	Limitations	52
7.4.1	Cloud detection	52
7.4.2	Surface reflectance	53
7.4.3	Classification	53
8	Conclusion	54
	Bibliography	57
	Appendices	63
A	Data	63
A.1	AWS Glacier de la Plaine Morte	63
A.2	AWS Weissseespitze/Gepatschferner	64
A.3	AWS Hintereisferner	65
B	Results	66
B.1	RQ1: Albedo comparison	66
B.1.1	AWS albedo vs. satellite albedo	66
B.2	RQ2: Glacier trends	68
B.2.1	Glacier de la Plaine Morte	68
B.2.2	Kanderfirn	69
B.2.3	Unteraargletscher	70
B.2.4	Hüfifirn	72
B.2.5	Ochsentaler Gletscher	73
B.2.6	Rhonegletscher	75
B.2.7	Grosser Aletschgletscher	76
B.2.8	Gornergletscher	78
B.2.9	Mer de Glace	80
B.2.10	Glacier Blanc	83
B.2.11	Ghiacciaio del Rutor	84
B.2.12	Vadrec del Forno	86
B.2.13	Ghiacciaio dei Forni	87
B.2.14	Ghiacciaio dell'Adamello	89
B.2.15	Vadret da Morteratsch	90
B.2.16	Gepatschferner	92
B.2.17	Hintereisferner	93
B.2.18	Gefrorene Wand Kees	95
B.2.19	Hallstätter Gletscher	96
B.2.20	Umbal Kees	97
B.2.21	Schlaten Kees	99

	B.2.22	Pasterze	100
	B.2.23	Hochalm Kees	102
	B.3	RQ3: Drivers of albedo change	104
C	Code	106
	C.1	Google Earth Engine	106
	C.2	AWS Quality Control	106
AI Declaration			107
Personal Declaration			108

List of Figures

2.1	Glacier Mass Balance	3
3.1	Study area	8
3.2	Automatic Weather Stations	10
4.1	Satellite Data Availability Gornergletscher (CH)	18
4.2	Satellite Data Availability Glacier de la Plaine Morte (CH)	18
5.1	Workflow	20
5.2	Elevation Bands Grosser Aletschgletscher	26
6.1	Albedo scatterplots of the AWS Glacier de la Plaine Morte vs. S2 for all observations from 2017 to 2024	30
6.2	Albedo scatterplots of the AWS Weissseespitze/Gepatschferner vs. S2 for all observations from 2017 to 2024	32
6.3	Sensor comparison L8/9 vs. S2	33
6.4	Sensor comparison Hintereisferner 12.07.2020	34
6.5	Sensor comparison Hintereisferner 13.04.2022	34
6.6	Scatterplot SW albedo Hintereisferner 12.07.2020	34
6.7	Scatterplot SW albedo Hintereisferner 13.04.2022	34
6.8	Sensor comparison Hintereisferner monthly mean Kendall's Tau	35
6.9	Sub-seasonal trends Grosser Aletschgletscher	36
6.10	Sub-seasonal trends Unteraargletscher	38

List of Tables

2.1	Glacier albedo	5
3.1	European Alpine glaciers used in the analysis	9
3.2	European Alpine glaciers with available AWS data	10
3.3	European Alpine glaciers used for the sensor comparison between Sentinel 2 and Landsat 8/9	11
4.1	AWS Glacier de la Plaine Morte 2014-2017 measurements	13
4.2	AWS Glacier de la Plaine Morte 2016-2024 measurements	13
4.3	AWS Weissseespitze/Gepatschferner 2017-2023 measurements	14
4.4	AWS Hintereisferner measurements	15
4.5	GEE satellite imagery collections	16
5.1	AWS metrics as drivers of bare-ice albedo change	21
5.2	GEE classification of satellite imagery	22
5.3	GEE export datasets	24
6.1	AWS albedo vs. satellite albedo correlation on Glacier de la Plaine Morte 2017–2024 for all surface classes	30
6.2	AWS albedo vs. satellite albedo correlation on Glacier de la Plaine Morte 2017–2024 for non-snow surface classes	30
6.3	AWS albedo vs. satellite albedo correlation on Weissseespitze/Gepatschferner 2017–2023 for all surface classes	31
6.4	AWS albedo vs. satellite albedo correlation on Weissseespitze/Gepatschferner 2017–2023 for non-snow surface classes	31
6.5	Results for sub-seasonal trends	37
6.6	Results for interannual trends	39
6.7	Results for drivers of albedo change on Glacier de la Plaine Morte 2016–2024	40
6.8	Subset of the results for drivers of albedo change on Glacier de la Plaine Morte 2014–2017	41
6.9	Results for drivers of albedo change on Hintereisferner 2013–2024	42

Abbreviations

AWS	Automatic Weather Station
BOA	Bottom-Of-Atmosphere
DEM	Digital Elevation Model
ESA	European Space Agency
GEE	Google Earth Engine
L8	Landsat 8
L9	Landsat 9
LST	Land Surface Temperature
LW	Longwave
MAE	Mean Average Error
m a.s.l.	Metres Above Sea Level
MODIS	Moderate Resolution Imaging Spectroradiometer
NaN	Not a Number
NASA	National Aeronautics and Space Administration
NIR	Near Infrared
RGI	Randolph Glacier Inventory
RMSE	Root Mean Square Error
S2	Sentinel 2
SLA	Snow Line Altitude
SW	Shortwave
SWIR	Shortwave Infrared
SZA	Solar Zenith Angle
TIR	Thermal Infrared
TOA	Top-Of-Atmosphere
USGS	U.S. Geological Survey
VIS	Visible Spectrum

1 Introduction

Alpine glaciers have been retreating for decades (Jouvet et al., 2011; Sommer et al., 2020), affecting many people and industries. Glacial meltwater provides a continuous runoff during the summer months, which is important for hydroelectric power generation (Jouvet et al., 2011; Sommer et al., 2020; Žebre et al., 2021). They also act as water reservoirs and can buffer the effects of droughts (Jouvet et al., 2011; Sommer et al., 2020; Ultee et al., 2022; Žebre et al., 2021). Changes in the hydrological regime affect water availability for agriculture (Davaze et al., 2018) and drinking water quality (Davaze et al., 2018; Žebre et al., 2021). In addition to their hydrological functions, glaciers are important landmarks and benefit mountain tourism (Jouvet et al., 2011; Sommer et al., 2020; Žebre et al., 2021). The retreat of glaciers leads to changes in the mountain landscape and an increase in natural hazards, endangering the region's inhabitants as well as infrastructure and tourism (Davaze et al., 2018; Jouvet et al., 2011; Sommer et al., 2020; Ritter et al., 2012; Rounce et al., 2023; Žebre et al., 2021). Projections show that if global warming continues at its current rate and no strong action is taken, most of Europe's Alpine glaciers will be completely lost by 2100 (Hock and Huss, 2021; Jouvet et al., 2011; Rounce et al., 2023; Žebre et al., 2021).

Rising temperatures are one of the main causes of increased glacier melt rates (Hock and Huss, 2021; Johnson and Rupper, 2020; Rounce et al., 2023). Melting snow exposes more bare ice, leading to a darkening of the glacier surface, as has been observed in Alpine glaciers in recent decades (Di Mauro and Fugazza, 2022; Fugazza et al., 2016; Fugazza et al., 2019; Naegeli et al., 2019). In addition, deposition of light absorbing impurities darkens the surface and increases melting of snow and bare ice (Barandun et al., 2022; Di Mauro and Fugazza, 2022; Fugazza et al., 2019). Surface darkening lowers the albedo, accelerating melt rates, as albedo feedback is a major driver of glacial melt (Fugazza et al., 2019; Fugazza et al., 2016). This makes the albedo an important parameter in modelling glacier change. The interplay between melt rates and albedo change is captured by the positive albedo feedback: the lower the albedo, the more shortwave radiation is absorbed, which increases melt and lowers the albedo even further (Barandun et al., 2022; Di Mauro and Fugazza, 2022; Johnson and Rupper, 2020; Naegeli et al., 2019).

Glacier albedo is often modelled as a constant per surface type (snow, firn, ice) in mass balance models, leading to skewed predictions in simulations (Fugazza et al., 2016; Naegeli et al., 2015). This calls for a better understanding of the albedo parameter and its sub-seasonal and interannual changes. Current research has often focused on small scales, studying albedo changes for

only one glacier (Fugazza et al., 2016; Oerlemans et al., 2009) or small areas within the European Alps (Fugazza et al., 2019; Naegeli et al., 2019). In addition, there is a lack of large-scale studies that specifically investigate bare-ice albedo rather than glacier-wide albedo (Di Mauro and Fugazza, 2022). Satellite data have been used by several studies, but either limited to a single sensor (Fugazza et al., 2016; Naegeli et al., 2019), the coarse resolution of the MODIS mission (Davaze et al., 2018; Di Mauro and Fugazza, 2022), or the use of older Landsat missions (Fugazza et al., 2019). This leaves a gap for a comprehensive analysis of a large region such as the European Alps using data from the latest satellite missions (Landsat 8/9 and Sentinel 2) combined with ground measurements from several automatic weather stations.

In this thesis, sub-seasonal and interannual changes in the bare-ice albedo of alpine glaciers are studied and the drivers of albedo changes investigated. Satellite data from Landsat 8/9 and Sentinel 2 will be compared with each other and with measurements from automatic weather stations located on individual glaciers. The first objective is to find out how well the different satellite sensors correlate with each other, and how well the satellite data correlate with ground measurements. The satellite data will then be used for a comprehensive albedo time series analysis for 23 Alpine glaciers in Europe. The second objective is to detect sub-seasonal and interannual trends. For the third objective, the bare-ice albedo for individual glaciers will be retrieved from satellite imagery to investigate different drivers of bare-ice albedo changes. Land surface temperature data from satellite imagery is a surface property that will be analysed as a driver. For the meteorological factors, average air temperature measurements and SW radiation are investigated as drivers. The results of the three objectives should improve the understanding of the drivers of bare-ice albedo changes on glaciers and show sub-seasonal and interannual trends for the glaciated European Alps. It should also demonstrate the usefulness of a combined approach using satellite and ground data to monitor glaciers and detect changes.

Three research questions are posed to achieve the above objectives.

RQ1 How well do bare-ice albedo observations from ground measurements, from Landsat 8/9, and from Sentinel 2 correlate with each other?

RQ2 What are the sub-seasonal and interannual trends in bare-ice albedo for the Alpine glaciers in Europe?

RQ3 What surface properties and meteorological factors drive changes in the albedo of bare ice?

2 Theory

2.1 Glacier characteristics

The glacier mass balance is the sum of all accumulation and ablation on a glacier. It allows a simplified division of the glacier into an accumulation zone and an ablation zone, as shown in Figure 2.1. They are separated by the equilibrium line, where annual accumulation is equal to annual ablation (Benn and Evans, 2010). European Alpine glaciers are characterised by a winter accumulation regime. This means that in winter, most of the accumulation on the glacier occurs through snowfall. Over the years, the snow is transformed into ice by metamorphosis. This is what makes the glacier grow. The ablation takes place during the summer months, mainly from June to September. During this time, the snow cover in the ablation zone melts completely, exposing the bare ice below. The ice is exposed to the atmosphere and mass is lost through melting, evaporation, sublimation, or physical abrasion by wind (Benn and Evans, 2010). However, in warm years it is possible for bare ice to be exposed in the accumulation zone (Cuffey and Paterson, 2010).

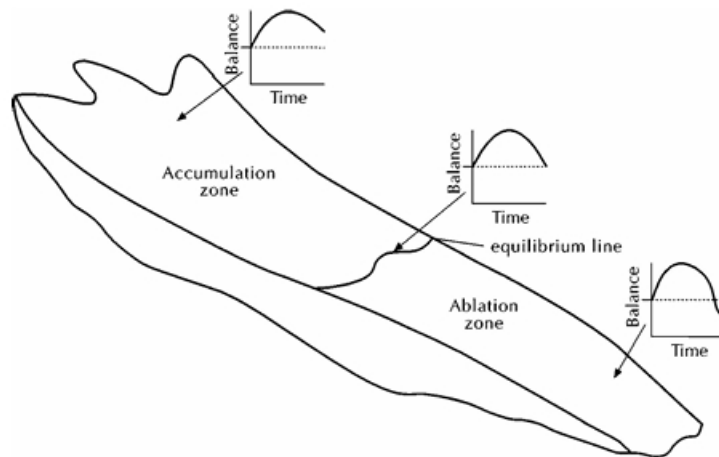


Figure 2.1: Sketch of a glacier showing the division into an accumulation zone and an ablation zone divided by the equilibrium line. (Benn and Evans, 2010)

2.2 Surface energy balance

The focus of this work is on the ablation zone and the bare ice exposed in summer. The energy surplus at the surface leads to melting. This is represented by the surface energy balance. It describes the incoming and outgoing energy fluxes at the surface of the glacier. It is described by the following equation:

$$SW + LW + QE + QH + QR - QT - M = 0 \quad (2.1)$$

Since energy cannot be gained or lost, all fluxes sum to zero. SW is the difference between incoming and outgoing shortwave (SW) radiation. Similarly, LW is the difference between incoming and outgoing longwave (LW) radiation. QE is the sensible heat flux, which is the energy transferred at the contact of the ice surface with the atmosphere. QH is the latent heat flux exchanged between the ice surface and the atmosphere by evaporation/condensation and sublimation/deposition. QR is the contribution of rain to the energy balance. The two negative terms are the energy used to change the temperature of the ice, QT , and the energy used to melt ice or freeze water, M (Benn and Evans, 2010).

These energy fluxes can be used to characterise changes in the glacier surface. The most important drivers of surface melt are the SW radiation and the heat content of the atmosphere, which influences both the LW radiation flux and the sensible heat flux. The incoming SW radiation depends on the zenith angle of the sun. This angle represents the deviation from the zenith, which is the position just above the observer. The zenith angle in turn depends on latitude, season, and time of day. At mid-latitudes, where the European Alps are located, solar radiation can reach up to 1000 W/m^2 in summer and still reach about 450 W/m^2 in winter. The SW radiation received by a glacier surface comes from direct solar radiation, diffuse radiation scattered in the atmosphere, and scattered radiation from the environment. The amount of SW radiation absorbed by the glacier depends on the surface albedo (Cuffey and Paterson, 2010). Albedo is defined as the ratio of outgoing solar radiation to incoming solar radiation (Equation 2.2). The higher the albedo, the more SW radiation is reflected. Conversely, the lower the albedo, the more SW radiation is absorbed, increasing surface melting (Cuffey and Paterson, 2010).

$$\alpha = SW_{out} / SW_{in} \quad (2.2)$$

Another important driver of glacial melt is the heat content of the atmosphere. A warm atmosphere emits more LW radiation, and the sensible heat flux at the atmosphere/glacier interface is greater (Cuffey and Paterson, 2010). The emitted LW radiation depends on the Stephan-Boltzmann equation (Benn and Evans, 2010):

$$I = \epsilon\sigma T^4 \quad (2.3)$$

Since temperature is to the power of four, the flux is much stronger for each degree increase in air temperature. In this thesis, SW radiation and air temperature are investigated as drivers of albedo change because of their large influence on the surface energy balance of a glacier. They are shown to directly influence glacier melt, which in turn influences surface albedo.

The energy budget regime of European Alpine glaciers can be characterised as follows: the glacier receives high net SW radiation in the ablation zone due to the lower albedo of the bare ice. In addition, there is a large LW radiation flux from the atmosphere due to the warm and humid air. This also leads to a large sensible heat flux at the glacier surface. On Pasterze Glacier, Austria, these factors lead to up to two metres of ice melt per month in the ablation zone (Cuffey and Paterson, 2010).

2.3 Glacier albedo

The albedo of glaciers is highly variable in space and time (Benn and Evans, 2010). Table 2.1 shows the variability from very high albedo values for fresh snow to very low values for dirty or debris-covered ice. This variability directly influences the amount of SW radiation absorbed by the glacier and contributes to glacier melt (Cuffey and Paterson, 2010).

Table 2.1: The albedo of snow and ice on a glacier. (Benn and Evans, 2010)

Surface	Albedo
Dry snow	0.80-0.97
Melting snow	0.66-0.88
Firn	0.43-0.69
Clean ice	0.34-0.51
Slightly dirty ice	0.26-0.33
Dirty ice	0.15-0.25
Debris-covered ice	0.10-0.15

The focus of this thesis is on bare ice in the ablation zone. Bare ice has a lower albedo than snow, and there are many factors that reduce the albedo even further. The crystal size of the ice influences the scattering of incoming SW radiation and thus the albedo of the ice. Melting and refreezing of the ice surface leads to changes in the ice crystals on the surface, changing the albedo. The bubble content is another factor that affects the albedo in the same way as the ice crystals, by affecting the scattering mechanisms of the ice (Cuffey and Paterson, 2010).

Meltwater can coat the ice surface, further reducing the albedo. Meltwater can accumulate in ponds on the glacier surface, drastically lowering the albedo (Fugazza et al., 2016) and increasing glacier melt where the pond is located. Meltwater can also interact with impurities on the glacier. The flowing water can lead to the accumulation of impurities in certain areas of the glacier (Cuffey and Paterson, 2010). Rain can also contribute to these phenomena. The water can cover the surface

of the glacier, reducing its albedo (Fugazza et al., 2016).

Light-absorbing impurities accumulate on the glacier surface over time. Soot (Fugazza et al., 2016), aerosols (Barandun et al., 2022; Fugazza et al., 2019; Oerlemans et al., 2009), and dust from exposed lateral moraines (Barandun et al., 2022; Oerlemans et al., 2009) are all found on glaciers. In addition, living organisms such as algae (Fugazza et al., 2019; Tedstone et al., 2020), yeasts (Fugazza et al., 2019), and various microbial communities (Fugazza et al., 2019) can grow on glaciers and cover large areas. Mineral material and biological material can form cryoconites together. These are sediments with a very dark colour that absorb SW radiation very efficiently. This causes the cryoconites to melt into the ice surface and form cryoconite holes (Cook et al., 2016). Impurities and debris that accumulate on the surface strongly increase the absorption of SW radiation and the melting of the glacier ice up to a cover thickness of two millimetres; above this thickness, the cover has the opposite effect on the ice, acting as an insulator against SW radiation and thereby reducing melt rates (Benn and Evans, 2010).

The interaction of the aforementioned factors results in a very high spatial and temporal variability of the bare-ice albedo. The annual cycle in the ablation zone starts with snow and high albedo values until the ablation season begins. The albedo gradually decreases as the bare ice is exposed and the ice begins to melt. As a result, the bare-ice albedo is usually at its lowest point at the end of the ablation season in September. Snowfall events in summer can temporarily increase the albedo and reduce surface melt. However, a thin snow cover usually does not last long and melts quickly to reveal the bare ice (Cuffey and Paterson, 2010).

2.4 Satellite remote sensing for glacier monitoring

Satellites provide a good method for remote monitoring of glacier albedo. Long-term satellite missions such as Landsat and MODIS allow for comprehensive glacier albedo time series analyses (Davaze et al., 2018; Barandun et al., 2022; Di Mauro and Fugazza, 2022; Fugazza et al., 2019; Naegeli et al., 2019). Satellite imagery provides a convenient method for monitoring glacier extent and detecting glacier retreat (Paul et al., 2020). The global coverage of satellites also makes it possible to monitor changes in glaciers on a large scale (Barandun et al., 2022; Di Mauro and Fugazza, 2022; Fugazza et al., 2019).

MODIS offers only a coarse spatial resolution of 500 metres per pixel, which is not able to capture the albedo variability found on alpine glaciers (Naegeli et al., 2017). However, the newer Landsat 8/9 (30 metres) and Sentinel 2 (10 metres) satellites provide much higher resolution, which will improve glacier albedo monitoring. This is particularly important in a warming climate with predicted large glacier mass loss and surface darkening.

Satellite albedo products have been validated with ground measurements from automatic weather

stations in several studies (Davaze et al., 2018; Fugazza et al., 2016; Naegeli et al., 2017). Good results confirm the usefulness of satellite data. The albedo products were used to investigate the relationship between glacier surface albedo and glacier mass balance (Davaze et al., 2018; Naegeli and Huss, 2017). The results show that there is indeed a relationship, encouraging the use of satellite data to remotely estimate glacier mass balance from albedo changes. This will help to monitor the mass balance of more glaciers and can complement in-situ measurements, which are very time- and resource-intensive (Davaze et al., 2018).

Satellite remote sensing has also been useful in detecting albedo trends in glaciers. Surface albedo darkening has been observed on many glaciers over the last 40 years (Di Mauro and Fugazza, 2022; Barandun et al., 2022; Fugazza et al., 2016; Fugazza et al., 2019; Naegeli et al., 2019). Identified causes of surface darkening include deposition of impurities and debris on the glacier (Barandun et al., 2022; Fugazza et al., 2016; Fugazza et al., 2019), exposure of larger bare-ice areas, and longer ablation seasons due to a warming climate (Di Mauro and Fugazza, 2022; Fugazza et al., 2019; Naegeli and Huss, 2017; Naegeli et al., 2019).

3 Study Area

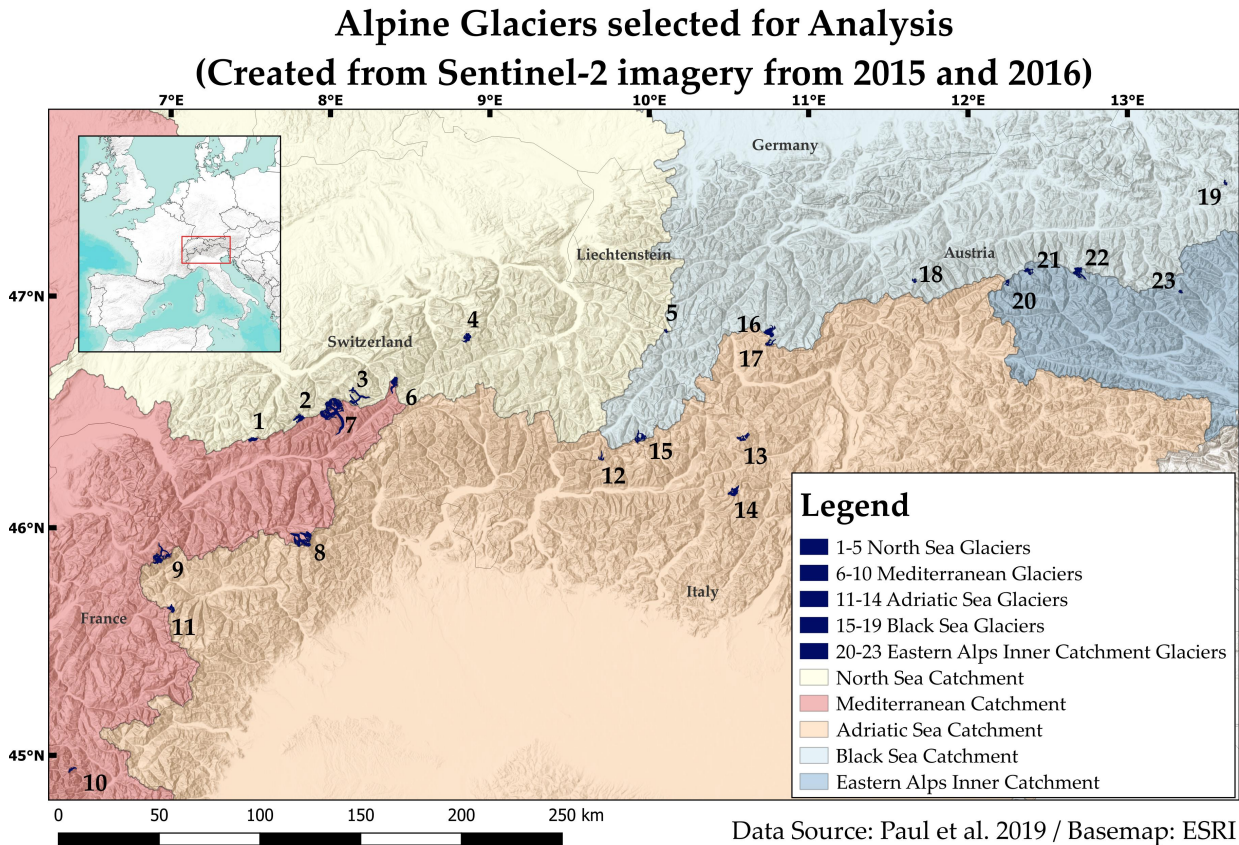


Figure 3.1: Study area overview showing the 23 selected European Alpine glaciers and the five major European Alpine water catchments (Lehner and Grill, 2013; Paul et al., 2019).

This thesis focuses on a selection of Alpine glaciers for a comprehensive analysis of changes in bare-ice albedo. The Alpine glaciers are obtained from the Paul et al. (2019) dataset. The glacier outlines are derived from Sentinel 2 images from 2015 and 2016. The Alpine region is divided into five catchments for the selection of glaciers. The catchments are derived from Lehner and Grill (2013) using the level 4 catchments from the dataset. This results in the following catchments:

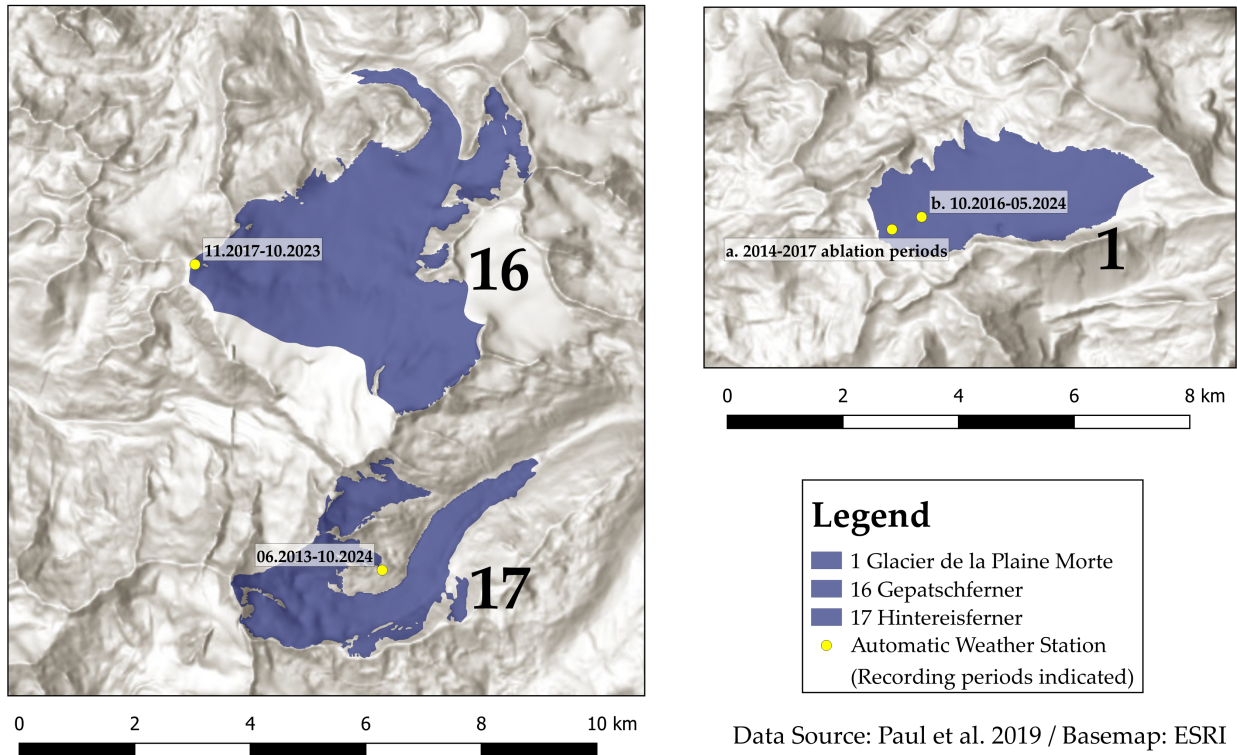
- North Sea Catchment
- Mediterranean Catchment
- Adriatic Sea Catchment
- Black Sea Catchment
- Eastern Alps Inner Catchment

Each glacier was assigned to a catchment area. Four or five glaciers were then selected for each catchment. Priority was given to larger glaciers, but the aim was to get a good distribution between north and south as well as east and west. This ensures that glaciers from all Alpine regions are represented in the trend analysis. The resulting glacier map is shown in Figure 3.1, and the glaciers are shown in more detail in Table 3.1, while an RGB image of each glacier can be found in the *Appendices* section B under subsection "RQ2: Glacier trends". This selection of 23 glaciers is used for the trend analyses in research question two, while a subset of glaciers is used for research questions one and three.

Table 3.1: Table of the European Alpine glaciers used in the analysis (Paul et al., 2019; RGI 7.0 Consortium, 2023).

Nr.	Glacier name	Mean Altitude (m a.s.l.)	Area (km ²)	Latitude WGS 84	Longitude WGS 84	Aspect
1	Glacier de la Plaine Morte	2720	6.8	46.38° N	7.51 E	320°
2	Kanderfirn	2788	11.8	46.47° N	7.80 E	285°
3	Unteraargletscher	2694	20.4	46.57° N	8.19 E	85°
4	Hüfifirn	2716	11.2	46.82° N	8.86 E	220°
5	Ochsentaler Gletscher	2847	2.2	46.85° N	10.10 E	8°
6	Rhonegletscher	2941	14.1	46.62° N	8.41 E	210°
7	Grosser Aletschgletscher	3054	77.3	46.48° N	7.97 E	145°
8	Gornergletscher	3314	40.1	45.95° N	7.81 E	321°
9	Mer de Glace	2887	28.8	45.89° N	6.94 E	17°
10	Glacier Blanc	3190	4.7	44.94° N	6.37° E	68°
11	Ghiacciaio del Rutor	2993	7.6	45.65° N	7.00° E	340°
12	Vadrec del Forno	2744	5.0	46.32° N	9.71° E	359°
13	Ghiacciaio dei Forni	3111	10.5	46.39° N	10.61° E	345°
14	Ghiacciaio dell'Adamello	2974	14.4	46.17° N	10.53° E	46°
15	Vadret da Morteratsch	3026	14.6	46.40° N	9.97° E	353°
16	Gepatschferner	3061	15.6	46.85° N	10.75° E	13°
17	Hintereisferner	3013	7.0	46.80° N	10.75° E	64°
18	Gefrorene Wand Kees	2941	3.2	47.06° N	11.67° E	354°
19	Hallstätter Gletscher	2549	2.7	47.48° N	13.61° E	40°
20	Umbal Kees	2973	4.1	47.06° N	12.25° E	228°
21	Schlaten Kees	2969	7.9	47.10° N	12.39° E	61°
22	Pasterze	2859	16.2	47.10° N	12.68° E	110°
23	Hochalm Kees	2907	2.4	47.02° N	13.33° E	64°

Alpine Glaciers with Automatic Weather Stations



Data Source: Paul et al. 2019 / Basemap: ESRI

Figure 3.2: Detailed view of the glaciers with an automatic weather station. The positions of the automatic weather stations are indicated with yellow dots with their labels showing the recording period of each station.

For the first research question, the albedo correlation between automatic weather station (AWS) data and satellite sensors is limited to glaciers with available AWS data. This is also the case for the analysis of surface properties and meteorological factors that drive changes in albedo of bare ice. The glaciers in Table 3.2 are included and can be seen in Figure 3.2.

Table 3.2: Table of the European Alpine glaciers with available AWS data.

Nr.	Glacier name	Area (km ²)	Altitude AWS (m a.s.l.)	Latitude AWS	Longitude AWS	Placement
1a.	Glacier de la Plaine Morte	6.8	2701	46.38° N	7.49° E	on ice
1b.	Glacier de la Plaine Morte	6.8	2690	46.38° N	7.50° E	on ice
16	Gepatschferner	15.6	3499	46.85° N	10.72° E	on ice/firn
17	Hintereisferner	7	3031	46.80° N	10.76° E	off glacier

The correlation of albedo values between Sentinel 2 (S2) and Landsat 8/9 (L8/9) is also performed on a subset of glaciers. The selection is based on three criteria. Size, to include only the larger glaciers of the selection from Table 3.1. Aspect, to include glaciers with different aspects to cover a range of flow directions. Finally, the availability of satellite imagery to ensure sufficient observations for analysis. The selected glaciers are listed in Table 3.3.

Table 3.3: Table of European Alpine glaciers used for the sensor comparison between Sentinel 2 and Landsat 8/9. Availability is calculated as an annual mean from the available Google Earth Engine scenes with a cloud cover of maximum 60% (Paul et al., 2019; RGI 7.0 Consortium, 2023).

Nr.	Glacier name	Area (km ²)	Aspect	Availability Sentinel 2 2018-2023	Availability Landsat 8 2014-2023	Availability Landsat 9 2022-2023
2	Kanderfirn	11.8	285°	99	15	12
3	Unteraargletscher	20.4	85°	91	30	28
6	Rhonegletscher	14.1	210°	91	30	29
7	Grosser Aletschgletscher	77.3	145°	91	30	28
8	Gornergletscher	40.1	321°	103	33	27
13	Ghiacciaio dei Forni	10.5	345°	90	15	13
16	Gepatschferner	15.6	13°	94	17	16
17	Hintereisferner	7.0	64°	90	16	16

4 Data

4.1 Automatic weather stations

This section introduces the four automatic weather stations (AWS) used in this thesis. Each AWS is introduced separately, giving an overview of its location, specifications, and data gaps. Large data gaps affect the analysis, especially when they coincide with satellite image dates. The limited availability of satellite images is further constrained when AWS data are unavailable. The data gaps are listed in more detail in the Appendices section A.

4.1.1 Glacier de la Plaine Morte

4.1.1.1 Ablation periods 2014–2017

An AWS was installed on Glacier de la Plaine Morte for four ablation periods from 2014 to 2017. The station was placed on the western edge of the glacier, as shown in Figure 3.2. It was located at an altitude of 2701 m a.s.l. The exact coordinates are given in Table 3.2. The station was installed at the beginning of July each year and provided data for about three months. In 2017, it was deployed for the shortest period until 19 September, while in 2015 it was left on the glacier until 23 October, which was the longest recording period.

The station recorded data in 10-minute intervals (Table 4.1). It was equipped with a weather transmitter (Vaisala WTX520) to measure air temperature, wind, humidity, air pressure, precipitation (rain and hail), and tilt of the station, as well as a radiometer (Kipp & Zonen CNR4) to measure incoming and outgoing SW and LW radiation (Naegeli, 2017). For this thesis, only air temperature and SW radiation measurements are used.

The AWS Glacier de la Plaine Morte 2014–2017 has a good record for the ablation periods of the four years, with only minor data gaps that are not discussed further.

Table 4.1: Measurements taken by the AWS on the Glacier de la Plaine Morte during the 2014-2017 ablation periods.

Recording Periods	Measurements	Recording Interval
09.07.2014 - 28.09.2014	Air temperature, SW radiation, LW radiation,	10 minutes
02.07.2015 - 23.08.2015	Humidity, Wind speed, Wind direction,	
04.07.2016 - 06.10.2016	Precipitation (Rain/Hail)	
06.07.2017 - 19.09.2017		

4.1.1.2 Fixed station 2016–present

A permanent AWS was installed on the Glacier de la Plaine Morte in October 2016. The station is located close to the above-mentioned seasonal AWS on the Glacier de la Plaine Morte but positioned slightly more east, as can be seen in Figure 3.2. It is at an altitude of 2690 m a.s.l.

The station records data in a one hour interval (Table 4.2). It was initially equipped with sensors to measure air temperature and humidity (Campbell Scientific CS215), wind speed and direction (Lufft), and distance from the surface to measure snow height (Campbell Scientific SR50A). In October 2017, a Kipp & Zonen CNR4 radiometer was added. This gives additional SW and LW measurements. The station has been running with this set-up until the present day, but the data examined in this thesis stops on 24 May of 2024.

Table 4.2: Measurements taken by the AWS on the Glacier de la Plaine Morte, installed in October 2016 and in operation to date.

Recording Periods	Measurements	Recording Interval
03.10.2016 - 11.10.2017	Air temperature, Humidity, Wind speed, Wind direction, Snow height	1 hour
11.10.2017 - 24.05.2024	Air temperature, SW radiation, LW radiation, Humidity, Wind speed, Wind direction, Snow height	

This AWS on Glacier de la Plaine Morte has two particularly large data gaps in the temperature record in the summers of 2019 and 2023. This limits the analysis of air temperature as a driver of

bare-ice albedo change for these years. The measurement of SW radiation is more consistent and has only one large gap in the summer of 2019, which coincides with the gap in the air temperature record.

4.1.2 Weissseespitze/Gepatschferner

The AWS on the Gepatschferner is located just below the peak of the Weissseespitze. The station was installed in October 2017 at an altitude of 3499 m a.s.l. The exact position can be seen in Figure 3.2 in the left image. It is located on the western edge of the glacier.

The station records data in 10-minute intervals (Table 4.3). It was equipped with a range of different sensors to measure air temperature and humidity (Rotronic-HC2S3), air pressure (CS106 Vaisala PTB110), wind speed and direction (Young-05103-45), incoming and outgoing SW and LW radiation (Hukseflux-NR01), snow accumulation and ice ablation with a sonic distance sensor (CS-SR50a), and ice temperature (CS225). However, only the air temperature and SW radiation are used for the analysis in this thesis. The station remains on the glacier all year, however, there were slight changes to its position over the years. In 2019, the station tilted and fell over at the end of August, leading to a data gap in September 2019, and in 2022, it needed to be repositioned mid-summer due to the fast ablation (Baldo, 2024).

The AWS Weissseespitze/Gepatschferner has all data gaps present in both the air temperature and the SW radiation records. Two large gaps are noteworthy, at the end of the ablation period in 2019 and at the beginning of the ablation period in 2023.

Table 4.3: Measurements taken by the AWS Weissseespitze/Gepatschferner from October 2017 to date.

Recording Periods	Measurements	Recording Interval
31.10.2017 - 10.12.2023	Air temperature, SW radiation, LW radiation, Humidity, Air pressure, Wind speed, Wind direction, Snow accumulation, Ice ablation, Ice temperature	10 minutes

4.1.3 Hintereisferner

The AWS Hintereisferner is not located on the glacier itself but next to it at an altitude of 3026 m a.s.l., as seen in Figure 3.2 in the left image. The old station was installed in October 2010 and recorded data until October 2020. As L8 only became operational in 2013, the data used starts on 1 June 2013 (Table 4.4).

The recording interval was set at 10 minutes. It measured air temperature and humidity (Vaisala HMP45AC, replaced by Campbell Scientific EE181 in November 2019), incoming and outgoing

SW and LW radiation (Kipp&Zonen CNR4), soil temperature (Campbell Scientific T107), air pressure (Setra CS100), and wind speed and direction (Young 05103).

The station was repositioned in November 2020 and some sensors were changed or added. Air temperature and humidity are now measured with a different sensor (Campbell Scientific EE181). A sonic distance sensor (Campbell Scientific SR50) was installed to measure snow height, a solid particle flux measurement sensor to capture snowdrift (ISAW FlowCapt FC4), and a precipitation sensor (Ott Pluvio2L). The other sensors and the recording interval remain unchanged.

The new station is still in operation, and for this thesis, records until the end of October 2024 are used. Since the station is not positioned on ice and the SW measurements do not represent those of the glacier ice, glacier albedo cannot be derived from the data and only the air temperature data are used for the analysis.

AWS Hintereisferner is not stationed on the glacier, but next to it. Only the air temperature record is used to investigate air temperature as a driver of bare-ice albedo change during the ablation periods. A first large gap is present during the 2016 ablation season from May to the end of August, and a second large gap is present at the beginning of the 2019 ablation season until July.

Table 4.4: Measurements taken by the AWS Hintereisferner, installed in October 2010 and in operation to date.

Recording Periods	Measurements	Recording Interval
01.06.2013 - 01.10.2020	Air temperature, SW radiation, LW radiation, Soil temperature, Air pressure, Wind Speed, Wind direction	10 minutes
10.11.2020 - 31.10.2024	Air temperature, SW radiation, LW radiation, Soil temperature, Air pressure, Wind Speed, Wind direction, Snow height, Snowdrift, Precipitation	

4.2 Satellites

The satellite data used in this thesis are retrieved from the Google Earth Engine (GEE) catalogue. Specifically, Landsat 8 and 9 from NASA and USGS and Sentinel 2 from ESA are used. Each is briefly introduced, followed by a section on data availability in general. GEE provides atmospherically corrected orthorectified surface reflectance data, which are used for the thesis. It is processed to remove shadows and clouds. In addition, an albedo band is added to each scene following the

narrowband to broadband conversions presented below in *Methods* (chapter 5). An overview of the three GEE collections used can be found in Table 4.5.

Table 4.5: Specifications of the satellite datasets used from the Google Earth Engine Data Catalogue.

Satellite	Dataset Availability	Revisit Time	Spatial Resolution
Landsat 8	April 2013 - present	16 days	30 metres
Sentinel 2	March 2017 - present	5 days	10 metres (VIS & NIR) 20 metres (SWIR)
Landsat 9	October 2021 - present	16 days	30 metres

4.2.1 Landsat 8

Landsat 8 (L8) was the first of the three satellites to be launched in 2013. It is equipped with two sensors: the Operational Land Imager (OLI) and the Thermal Infrared Sensor (TIRS). The entire system has 11 spectral bands across the two sensors. The OLI sensor has 9 bands. Bands two to seven cover the range from visible (VIS) to near infrared (NIR) and shortwave infrared (SWIR), and all have a spatial resolution of 30 metres. Band one is used for aerosol detection and band nine for cirrus cloud detection, both also at 30 metres. Band eight is a panchromatic band and provides better spatial resolution at 15 metres. The TIRS sensor has a coarser spatial resolution at 100 metres and provides two bands in the thermal infrared (TIR) spectrum (U.S. Geological Survey, 2019). A combination of the VIS, NIR, and SWIR bands is used to calculate the narrowband to broadband albedo of a pixel. The different equations are discussed below in *Methods* (chapter 5). A spatial resolution of 30 metres per pixel can be achieved for the L8 albedo products.

L8 has a local overpass time of 10:00 a.m. \pm 15 minutes. It has a theoretical revisit time of 16 days (U.S. Geological Survey, 2019). However, because cloud cover can obscure the view, the empirical revisit time of a given glacier is usually longer.

4.2.2 Sentinel 2

The Sentinel 2 (S2) satellite system consists of a twin satellite configuration. Two S2 satellites orbit the Earth in opposite positions: Sentinel 2A was launched in 2015, followed by Sentinel 2B in 2017 (European Space Agency, n.d.[b]). They carry the same sensor and fly in the same orbit, working together as a system. The S2 satellites each carry one sensor: the Multi-Spectral Instrument (MSI). This sensor has 13 spectral bands in the VIS, NIR, and SWIR spectra. The VIS bands and one NIR band have a spatial resolution of 10 metres. Four additional bands in the spectrum between VIS and NIR have a resolution of 20 metres. The SWIR bands also have a resolution of 20 metres. Finally, three bands used for aerosol, water vapour, and cirrus detection have a resolution of 60 metres (European Space Agency, n.d.[a]). A spatial resolution of 10 metres per pixel can be achieved with S2 using the narrowband to broadband algorithms presented below in *Methods* (chapter 5).

The S2 satellites have a local overpass time of 10:30 a.m., which is very similar to that of L8. S2 provides a 5-day revisit time at the equator due to the twin-satellite setup. At mid-latitudes,

where the study area is located, the revisit time is even better with about 2-3 days (European Space Agency, 2015). However, this is also affected by clouds, resulting in a longer empirical revisit time.

4.2.3 Landsat 9

Landsat 9 (L9) is the latest of the satellites to be launched. It was launched in 2021 and carries the OLI-2 and TIRS-2 sensors. These are improved versions of L8's OLI and TIRS sensors, but have the same spectral setup (U.S. Geological Survey, 2022). This means that the same spatial resolution of 30 metres per pixel can be achieved for the L9 albedo product using the narrowband to broadband conversions. L9 has the same local overpass time of 10:00 a.m. \pm 15 minutes and operates at an 8-day offset from L8. On its own it also has a 16-day revisit time, but in tandem L8 and L9 provide an 8-day revisit time (U.S. Geological Survey, 2022). As mentioned, the empirical revisit time is longer due to cloud coverage, but overall, L9 offers an improvement to the Landsat mission.

4.2.4 Data availability

The theoretical revisit times given for L8, L9, and S2 can be used as an indication of data availability. However, the actual empirical revisit time depends mainly on three factors: the latitude of the area studied, the location with respect to the flight paths, and the highly variable cloud cover. The European Alps are located at a latitude where the flight paths of the satellites overlap. This means that a given glacier can be covered by two different flight paths. This increases the revisit time for that particular glacier. An increase in revisit time means that double the number of scenes are available per glacier compared to when it is covered by just one flight path.

Overall speaking for the glaciers investigated in this thesis, some have considerably more satellite scenes available than others, resulting in a more comprehensive analysis. As an example, this difference in data availability is illustrated by the comparison of the data availability for Gornergletscher, shown in Figure 4.1, and Glacier de la Plaine Morte, shown in Figure 4.2. The two glaciers are both located in the Swiss Alps and are only about 50 kilometres apart in direct distance. However, Gornergletscher is covered by two flight paths while Glacier de la Plaine Morte is only covered by one. Gornergletscher has about twice as many scenes per year, but the numbers vary from year to year as they are empirical. Nevertheless, it illustrates the advantage of having a glacier covered by two flight paths.

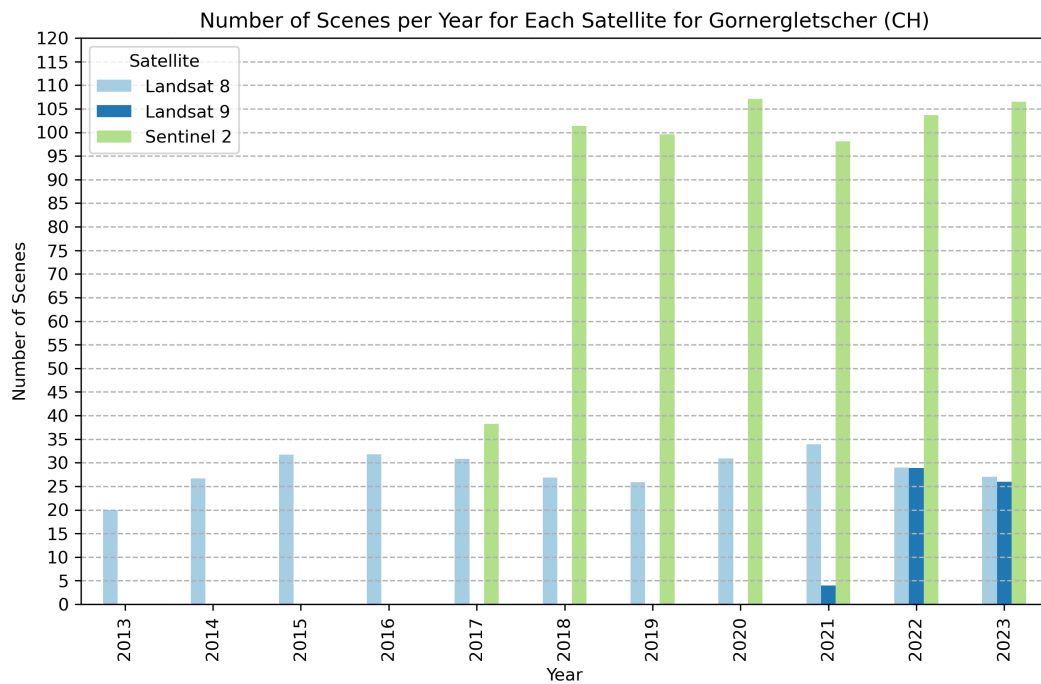


Figure 4.1: The number of available scenes per year for the area of the Gornergletscher (CH) with a cloud cover below 60%.

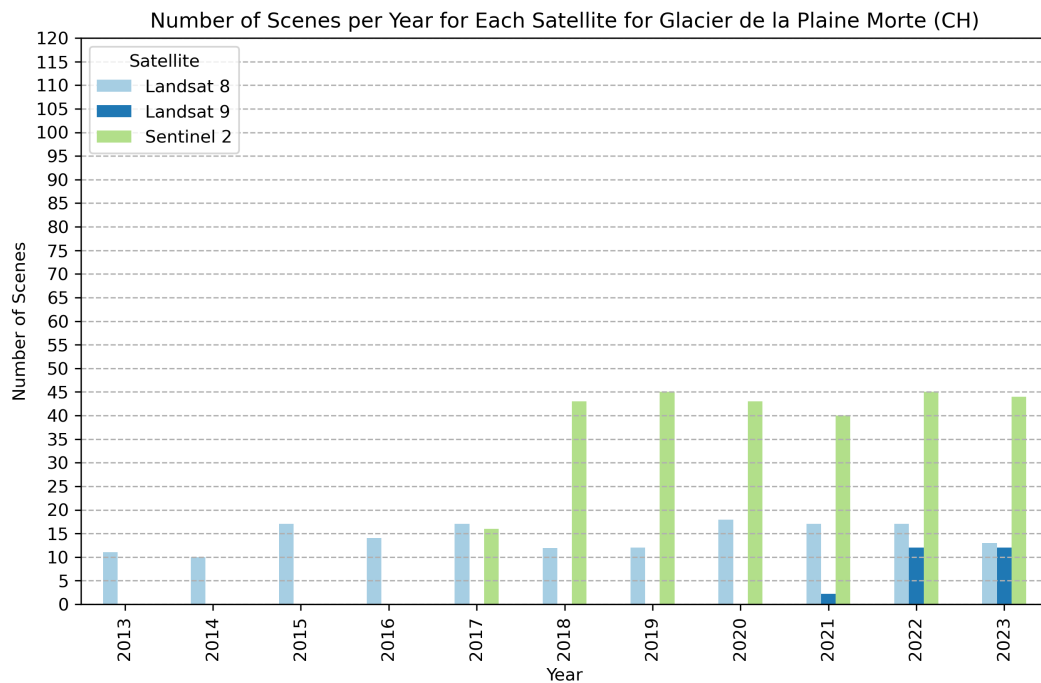


Figure 4.2: The number of available scenes per year for the area of the Glacier de la Plaine Morte (CH) with a cloud cover below 60%.

This thesis looks at the years from the launch of L8 in 2013 to 2024. For the first four years until 2016, satellite data are limited to L8 and its theoretical revisit time of 16 days. For a glacier covered by two paths, such as Gornergletscher in Figure 4.1, this results in about 30 scenes per full year of coverage. 2013 has less data because the system did not record for the whole year. In 2017, S2 became fully operational with the launch of Sentinel 2B. This doubles the number of scenes available for that year. From 2018 onwards, data availability increases significantly as S2 now records data throughout the year. For both Gornergletscher in Figure 4.1 and Glacier de la Plaine Morte in Figure 4.2, the availability of S2 scenes is three to four times that of L8 scenes due to the shorter revisit time. More data become available with the launch of L9 in 2021. The availability of L9 data is the same as that of L8. With their tandem flight schedule, they double the available Landsat scenes, which is most important for thermal data, only collected by L8 and L9 and not by S2.

5 Methods

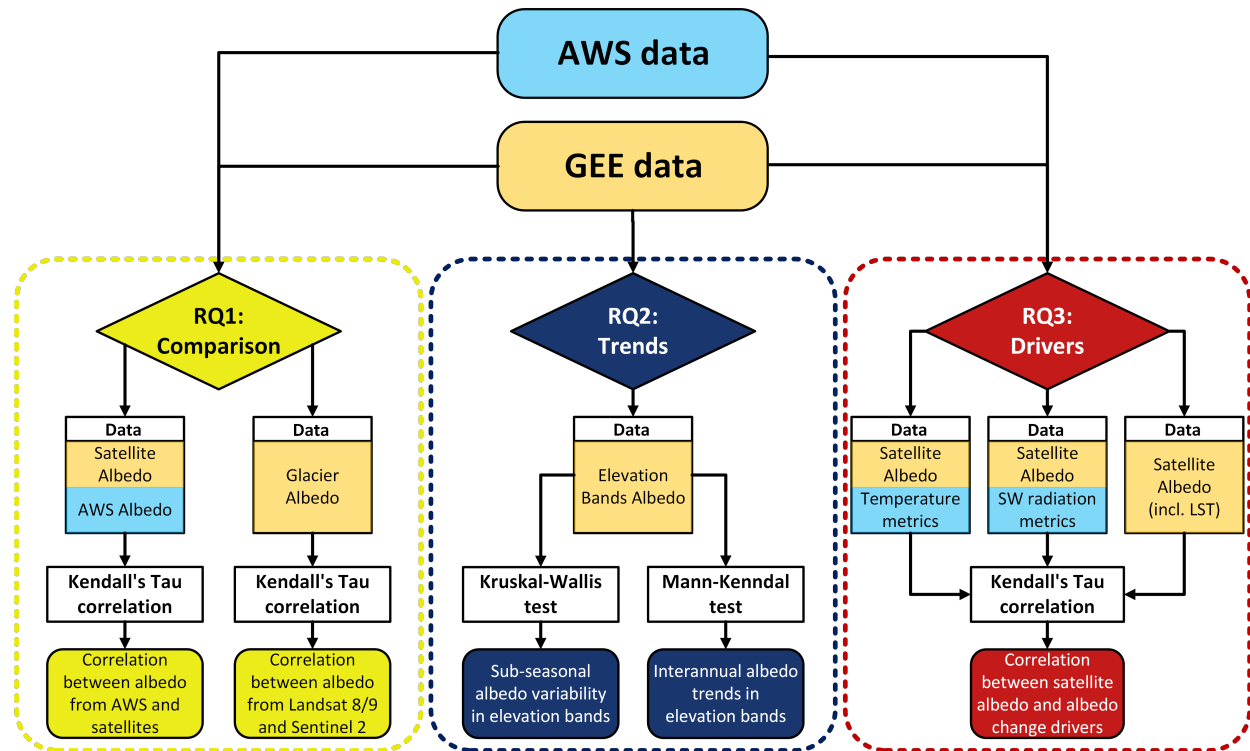


Figure 5.1: The workflow guiding the research questions of this thesis.

5.1 AWS data

The processing of the AWS data was done using Python 3.10 in Spyder 5.5.1, via Anaconda Navigator 2.4.0. The code was developed for AWS Weissseespitze/Gepatschferner and is linked in section C.

5.1.1 Quality control

The AWS data are quality controlled to remove erroneous data values. The air temperature measurements and the incoming and outgoing SW radiation values are checked. The script flags missing or Not a Number (NaN) values, such as those outside the range of the sensors used to measure them, or specifically for SW radiation, if the measured outgoing SW radiation is greater than the incoming SW radiation. The flags can be used at a later stage to identify the faulty records and exclude them from further analysis.

5.1.2 Albedo and drivers of albedo change

In the same step as the quality control, the AWS SW albedo used for research question one and a set of potential drivers of albedo change investigated in research question three are calculated. The calculation of albedo and drivers requires the quality controlled AWS data and a list of satellite observations. The albedo and the drivers are calculated separately for each satellite observation in the corresponding dataset. The time ranges correspond to the hours before the satellite image was taken. The calculated metrics are listed in Table 5.1. For the number of temperature crossings of the zero mark, crossings from positive to negative and from negative to positive are counted separately and summed up.

Table 5.1: The metrics calculated from the AWS data using satellite timestamps. They are listed with the corresponding time ranges.

Metric	Time range
SW albedo	Record closest to the satellite timestamp
Mean temperature	6h/12h/24h/48h/72h
Temperature range	12h/24h/48h
Hours with negative temperatures	12h/24h/48h
Nighttime minimum and maximum	Night before (10 p.m. - 6 a.m.)
Number of crossings of the zero degree mark	12h/24h/48h
Cumulative SW radiation	6h/24h/48h/72h

5.2 Satellite data

The satellite datasets are processed in the GEE to remove clouds and cloud shadows, to add an albedo band, to classify each pixel, and finally to generate the necessary data output for export. The methods to achieve these steps are explained in more detail below.

5.2.1 Google Earth Engine

The code used in the GEE is linked in the *Appendices* section C.

5.2.1.1 Cloud and cloud shadow detection

Cloud and cloud shadow detection works differently for L8/9 and S2. **Landsat** uses the **CFMask** algorithm to create a Quality Assessment (QA) band that is added to each image (Landsat Missions, n.d.). This algorithm uses a multi-pass approach to identify clouds, cloud shadows, and clear sky pixels. It uses the VIS, NIR, SWIR, and TIR bands of L8/9. In the first pass, potential cloud pixels (PCPs) are identified using several different spectral tests. Only if a pixel has a "true" result in each test is it considered a PCP.

The second pass distinguishes between water and land, based on their distinct differences in reflectance and temperature. A potential cloud layer is created separately for water and land using the information from the pixels identified as clear sky in the first pass. These are used for the temperature probability test, which uses the thermal information to distinguish clouds from water or land.

For water surfaces, a brightness probability test is conducted that uses the SWIR1 band, assuming

that water has a very low reflectance in this band. The temperature and brightness probabilities are then used to determine the probability that a pixel is cloudy and over water. For land pixels, a variability probability is calculated. This uses the spectral variability between NIR and VIS, SWIR and VIS, and within the VIS spectrum. The variability probability is combined with the temperature probability to give a cloud probability for land pixels. The final step is to combine the PCPs with the cloud probability of water or land to produce the final cloud layer.

The reflectance in the NIR band is used to calculate the cloud shadow layer. A flood-fill transformation is applied to the NIR band, and then the NIR band from the original image is subtracted from the flood-fill. This produces the potential cloud shadow layer (Zhu and Woodcock, 2012).

S2 uses an additional dataset called **Cloud Score+** provided by Google through the GEE. Instead of using decision trees like CFMask, it relies on weakly supervised deep learning. The first step is to train the model on images of the same location but under different cloud conditions. This helps it to learn the difference between land and atmosphere. In the second step, the model is further developed to predict the Atmospheric Similarity Index Measure (ASIM) between image pairs. In the final step, the model is trained with short time series of videos from sample locations to eventually be able to evaluate individual images on their atmospheric conditions and produce the Cloud Score+ Quality Assessment score. This results in a continuous and accurate detection of clouds and cloud shadows (Pasquarella et al., 2023; Pasquarella, 2023).

5.2.1.2 Classification

The same classification is used for all satellite images. Each pixel is classified into one of nine classes, which can be seen in Table 5.2. Each class has a number of spectral tests that are performed. The VIS, NIR, and SWIR bands are used. For some classes a digital elevation model (DEM) is also used if topography is relevant, such as for water or shadows. The results of the tests are combined into a test score for each class. The test scores are then used to assign each pixel to the class with the highest score. This results in a classification layer that is saved as an additional band to the image.

Table 5.2: The classes available in the GEE classification used in this thesis. The numbers use 0-based indexing.

Class	Number
Unclassified	0
Snow	1
Vegetation	2
Debris	3
Ice	4
Water	5
Shadow	6
Snow Shadow	7
Cloud	8

5.2.1.3 Narrowband to broadband shortwave albedo conversions

L8/9 and S2 have multi-spectral sensors. Therefore, narrowband to broadband conversion formulae are required to convert the measurements to shortwave albedo. Several different formulae exist for this task. In this paper, six different formulae are used and compared.

Liang (2000) provides a general formula (Equation 5.1) that was developed for Landsat 5/7, but has shown good results for L8/9 as well as S2 (Naegeli et al., 2017). The formula is designed to work for different surface types and atmospheric conditions.

$$\alpha_{SW,Liang} = 0.356 \cdot \alpha_{Blue} + 0.130 \cdot \alpha_{Red} + 0.373 \cdot \alpha_{NIR} + 0.085 \cdot \alpha_{SWIR1} + 0.072 \cdot \alpha_{SWIR2} - 0.0018 \quad (5.1)$$

Feng et al. (2024) suggest a different formula (Equation 5.2). It was developed and validated for the Greenland ice sheet in Feng et al. (2023). They used Landsat 4-8 and S2 data for their study. In Feng et al. (2024) they present a slightly adapted formula that has been tested on several Arctic and Alpine glaciers and ice caps. This is the formula used for comparison in this paper.

$$\alpha_{SW,Feng} = 0.7963 \cdot \alpha_{Blue} + 2.2724 \cdot \alpha_{Green} - 3.8252 \cdot \alpha_{Red} + 1.4343 \cdot \alpha_{NIR} + 0.2503 \quad (5.2)$$

Olmedo et al. (2016) used narrowband to broadband conversion formulae in the context of agriculture to model the land surface energy balance. In their work, they developed a formula (Equation 5.3) with different coefficients for Landsat 8. However, this formula was only applied to L8/9 data and not to S2 data. For this work, the formula is applied to L8/9 data only.

$$\begin{aligned} \alpha_{SW,Olmedo} = & 0.246 \cdot \alpha_{Blue} + 0.146 \cdot \alpha_{Green} + 0.191 \cdot \alpha_{Red} \\ & + 0.304 \cdot \alpha_{NIR} + 0.105 \cdot \alpha_{SWIR1} + 0.008 \cdot \alpha_{SWIR2} \end{aligned} \quad (5.3)$$

In their study, **Bonafoni and Sekertekin (2020)** worked on a new formula (Equation 5.4) for S2. They developed new coefficients to calculate shortwave albedo in rural and urban environments. Their formula was tested and validated for S2 data and is used in this thesis for S2 only.

$$\begin{aligned} \alpha_{SW,Bonafoni \text{ and } Sekertekin} = & 0.2266 \cdot \alpha_{Blue} + 0.1236 \cdot \alpha_{Green} + 0.1573 \cdot \alpha_{Red} \\ & + 0.3417 \cdot \alpha_{NIR} + 0.1170 \cdot \alpha_{SWIR1} + 0.0338 \cdot \alpha_{SWIR2} \end{aligned} \quad (5.4)$$

The last two formulae (Equation 5.5 and Equation 5.6) are from **Li et al. (2018b)**. They developed new coefficients for snow-free and snow-covered conditions using different spectra from digital libraries, excluding artificial materials. The formulae have been tested and validated using S2

data. Therefore, they are only used for S2 in this thesis.

$$\begin{aligned} \alpha_{SW, Li\ Snow-free} = & 0.2688 \cdot \alpha_{Blue} + 0.0362 \cdot \alpha_{Green} + 0.1501 \cdot \alpha_{Red} \\ & + 0.3045 \cdot \alpha_{NIR} + 0.1644 \cdot \alpha_{SWIR1} + 0.0356 \cdot \alpha_{SWIR2} - 0.0049 \end{aligned} \quad (5.5)$$

$$\begin{aligned} \alpha_{SW, Li\ Snow} = & -0.1992 \cdot \alpha_{Blue} + 2.3002 \cdot \alpha_{Green} - 1.9121 \cdot \alpha_{Red} \\ & + 0.6715 \cdot \alpha_{NIR} - 2.2728 \cdot \alpha_{SWIR1} + 1.9341 \cdot \alpha_{SWIR2} - 0.0001 \end{aligned} \quad (5.6)$$

5.2.2 Export

The satellite data are exported from the GEE for analysis after clouds and cloud shadows have been removed, it has been classified and the albedo band has been added to each scene. The scenes are also filtered by the cloud cover property. Each scene has a cloud cover percentage that indicates how many pixels of the scene are covered by clouds. Different cloud cover percentages were tested for this thesis. A maximum cloud cover of 60% gave good results while keeping data availability high. The exports can be divided into three datasets, which are listed in Table 5.3 and introduced in the following three sections. The code can be found in the *Appendices* section C.

Table 5.3: A list of the short names of the three GEE datasets and the corresponding section in which they are presented.

Section Number	Dataset Short Name
5.2.2.1	Satellite Albedo
5.2.2.2	Glacier Albedo
5.2.2.3	Elevation Bands Albedo

5.2.2.1 Albedo/land surface temperature at the AWS location

This first dataset is used for the correlation analysis between AWS measured albedo and satellite-retrieved albedo, as well as the correlation between satellite albedo and the different drivers of albedo change. It is different for L8/9 and S2. For **L8/9**, the albedo and land surface temperature (LST) of the pixel at the location of the AWS are exported. The export for **S2** includes only the albedo, both for the pixel at the AWS location and a mean albedo value of a 3x3 pixel neighbourhood around the AWS location. The class is also added to the export in order to be able to distinguish it later in the analysis and use only the ice class measurements for the correlation analysis with the drivers.

Satellite data are exported for all AWS locations. The start point is the starting date of the AWS dataset and the end point is the end of the AWS dataset. As the correlation analysis is class independent, all images falling within this time frame are used for the data export.

This dataset will be referred to as the Satellite Albedo.

5.2.2.2 Albedo pixel values for the whole glacier

This dataset is used for the correlation analysis between L8/9 and S2. For the selection of glaciers in Table 3.3, all L8/9 and S2 satellite images taken on the same day are used. From these images, the glaciers are extracted using their outlines from the Randolph Glacier Inventory 7.0 (RGI 7.0 Consortium, 2023) database available through the GEE. The albedo values of all pixels within the glacier outlines are exported along with their exact coordinates, which are used for correlation analysis.

Data are exported for the years 2017-2024, after S2 became fully operational and started providing data.

5.2.2.3 Mean albedo values of elevation bands

The third GEE dataset is used for the interannual and sub-seasonal trend analysis of bare ice on a selection of European Alpine glaciers (Table 3.1). The analysis is performed using elevation bands as illustrated in Figure 5.2, where the elevation bands of Grosser Aletschgletscher are shown as an example. An elevation band is defined as all pixels with an elevation value between the threshold values z_{min} and z_{max} . The elevation values of z_{min} and z_{max} are chosen to be 100 metres apart for each band, except for the band that reaches z_{max} . The bands are calculated in 100 metre steps from z_{min} . The threshold value z_{max} is often not at a perfect 100 metre step for the last elevation band. This cuts the last band short of 100 metres elevation difference. ESA's Copernicus GLO-30 DEM is used to generate the elevation bands (European Space Agency and Airbus, 2022). The DEM is directly accessible in GEE.

The elevation bands start at the lowest elevation of the glacier and extend over the lower 2/3 of the glacier elevation up to the theoretical snow line altitude (SLA). The higher elevations of the glacier are excluded under the assumption that they are snow-covered throughout the year. As this thesis only examines trends in bare-ice albedo, the snow-covered areas are of no interest. Furthermore, the threshold of 2/3 for the SLA was chosen to make it less computationally intensive and to allow the data to be exported from GEE.

The theoretical SLA was empirically tested using data from Grosser Aletschgletscher. Satellite data from 2013–2024 was used to determine the empirical SLA for each image. The mean and median of the empirical SLA exceeded that of the chosen SLA at 2/3 of the glacier's altitude range in some images, but was lower in about 85% of the images.

The elevation bands of each glacier are used to calculate the mean ice albedo per elevation band. Since only bare-ice measurements are of interest, the mean ice albedo is calculated using only pixels classified as ice, and a threshold was set to include the mean ice albedo only if enough pixels were classified as ice. First, a count of all classified pixels in that elevation band is defined. Second, the number of pixels classified as debris is subtracted from this count. Debris is considered static and should be excluded from the analysis. By excluding debris, elevation bands partially

Grosser Aletschgletscher (CH)

15.09.2024

Sentinel 2 accessed with GEE

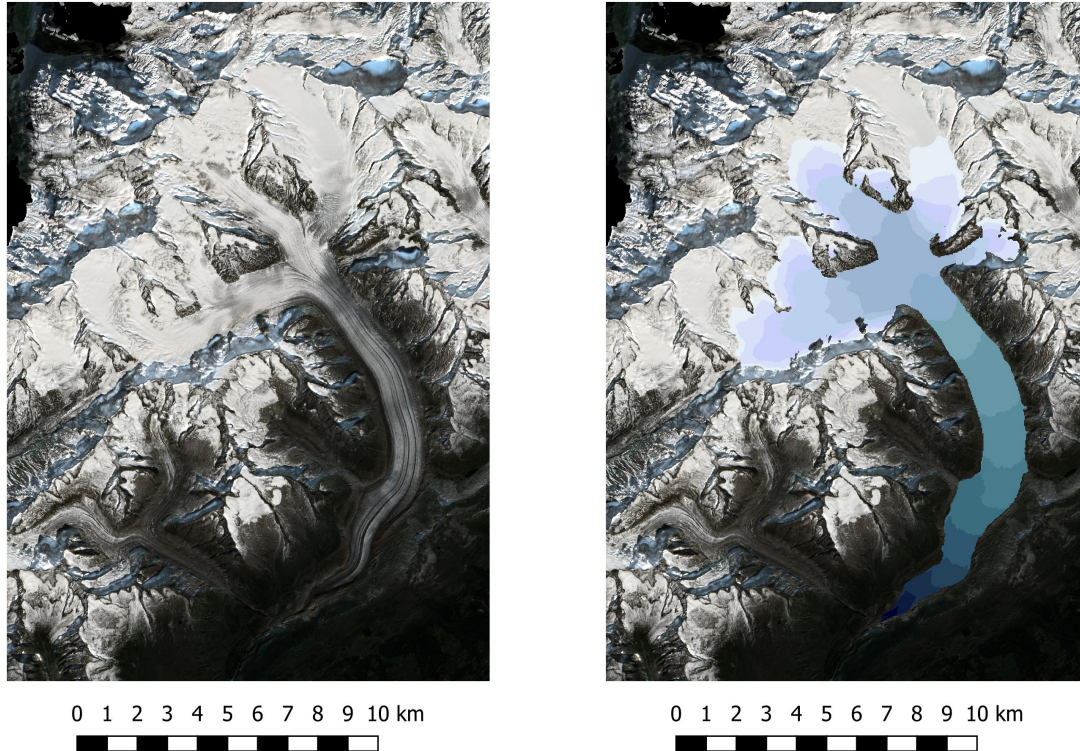


Figure 5.2: Satellite image of Grosser Aletschgletscher on the left and elevation bands used for trend analysis on the right, in different shades of blue. The darkest shade marks the lowest elevation, while the lightest shade marks the highest elevation.

covered by debris may still have enough ice class pixels to be included. Finally, a count of all pixels classified as ice is defined. Only if the number of pixels classified as ice is greater than or equal to half of the total number of classified pixels, excluding debris pixels, is the mean ice albedo included in the export. In cases where the pixel count threshold is not met, the mean ice albedo is not included.

L8/9 and S2 data is used in combination for this export. Furthermore, as only bare-ice data are of interest, the export is limited to the months June–October for the years 2013–2024.

5.3 Statistical analysis

Statistical analysis was performed using Python 3.10 in Spyder 5.5.1, accessed via Anaconda Navigator 2.4.0.

5.3.1 RQ1: Albedo comparison

5.3.1.1 AWS albedo vs. satellite albedo

The Satellite Albedo dataset and the AWS measured albedo are compared in a correlation analysis. This is done using **Kendall's Tau correlation coefficient**, a non-parametric rank correlation (Schaeffer and Levitt, 1956). This means that no assumptions are made about the data, such as normality or homoscedasticity. The use of ranks makes it more resistant to outliers and a robust test (Croux and Dehon, 2010). It can also be used for small sample sizes (Sexton et al., 2021). This is important, as data availability can be an issue when working with satellite data.

The correlation analysis is complemented by two measures of error. The root mean square error (RMSE) and the mean average error (MAE) are both calculated for the data. The RMSE is more sensitive to outliers and can better capture the scatter in the data (Chai and Draxler, 2014).

5.3.1.2 L8/9 albedo vs. S2 albedo

The glacier albedo dataset is used to compare the albedos retrieved by L8/9 and S2. For each date with both L8/9 and S2 imagery, all glacier pixels are used in the correlation analysis. **Kendall's Tau correlation coefficient** is also used for this analysis as the data are not normally distributed.

5.3.2 RQ2: Trend analysis

5.3.2.1 Sub-seasonal trends

The elevation bands albedo dataset is used for the sub-seasonal trend analysis. The **Kruskal-Wallis test** is used to analyse whether there are significant albedo differences between the months of a year (Kruskal and Wallis, 1952; Yu et al., 2006). This is a non-parametric test, meaning that no assumptions are made about the structure and distribution of the data (Cabral Júnior and Lucena, 2020; Kruskal and Wallis, 1952). This is advantageous for small sample sizes, which is the case here due to the limited availability of satellite data (Shih and Hung, 2020).

5.3.2.2 Interannual trends

The test for interannual trends is also performed using the elevation bands albedo dataset. The **Mann-Kendall test** is used to detect monotonic trends in the data (Meals et al., 2011; Neeti and Eastman, 2011). The monotonic trend regression analysis shows whether albedo values are increasing or decreasing over time. This is a non-parametric test that makes no assumptions about the data being tested (Cabral Júnior and Lucena, 2020). As mentioned above, this is well suited to the small sample sizes at hand.

5.3.3 RQ3: Drivers of albedo change

To investigate the potential drivers of albedo change listed in Table 5.1, **Kendall's Tau correlation coefficient** is also used. The temperature and radiation metrics are compared with the Satellite Albedo dataset to detect correlations. The AWS Hintereisferner is an exception as it does not use the Satellite Albedo dataset but the elevation bands albedo dataset. This is because the station is located off-ice next to the glacier. The metrics are compared with the mean albedos from the elevation bands.

6 Results

6.1 RQ1: Albedo comparison

6.1.1 AWS albedo vs. satellite albedo

The narrowband to broadband shortwave albedo conversions from Liang (2000) and Feng et al. (2024) gave the best correlation results in all comparisons. In addition, for S2 it proved useful to use the albedo mean of a 3x3 pixel neighbourhood around the location of the AWS. The full results can be found in the corresponding results section in the *Appendices* section B. Due to the difficulty of classifying ice in some cases, all observations not classified as snow were treated as ice on the assumption that they had not been correctly classified. These are referred to as non-snow observations.

6.1.1.1 AWS Glacier de la Plaine Morte

The correlation analysis between the AWS albedo and the satellite albedo for the Glacier de la Plaine Morte AWS 2017–2024 shows high correlations for both the Liang (2000) and Feng et al. (2024) conversions for S2 and L8/9. The results are given in Table 6.1. A notable difference is seen in the error measures, where Feng et al. (2024) shows large errors for S2 and L8/9. They are between 0.13 to 0.15 larger than the error measures for Liang (2000).

Figure 6.1 shows scatterplots of AWS albedo against satellite albedo for Liang (2000) and Feng et al. (2024). Both plots show less scatter in the lower albedo region of 0–0.4. For higher albedo values around 0.8 the scatter is greater. Furthermore, the regression line for the Liang (2000) data is much closer to perfect fit. The Feng et al. (2024) data deviate more from perfect agreement as the albedo increases.

When only non-snow observations are considered, the correlation becomes better for both Liang (2000) and Feng et al. (2024). The results in Table 6.2 show significant results for all combinations except the Feng et al. (2024) conversion used on L8/9 data. The errors are smaller for the non-snow values compared to all observations in Table 6.1. However, the same pattern is seen where the Liang (2000) conversion leads to lower errors than the Feng et al. (2024) conversion.

Table 6.1: Correlation results of the AWS Glacier de la Plaine Morte albedo values with the satellite retrieved albedo values for pixels of all classes. The strength of correlation is highlighted in green and high errors (above 0.15) are shown in red.

Glacier de la Plaine Morte 2016-2024 (all observations)		Kendall's Tau	Significance $\alpha = 0.05$	Strength of Correlation	Mean Average Error	Root Mean Square Error
Sentinel 2	Liang 2000	0.53	yes	high	0.08	0.12
	Feng et al. 2024	0.59	yes	high	0.23	0.25
Landsat 8/9	Liang 2000	0.58	yes	high	0.10	0.12
	Feng et al. 2024	0.58	yes	high	0.24	0.26

Table 6.2: Correlation results of the AWS Glacier de la Plaine Morte albedo values with the satellite retrieved albedo values for pixels not classified as snow. The strength of correlation is highlighted in green and high errors (above 0.15) are shown in red.

Glacier de la Plaine Morte 2016-2024 (not snow)		Kendall's Tau	Significance $\alpha = 0.05$	Strength of Correlation	Mean Average Error	Root Mean Square Error
Sentinel 2	Liang 2000	0.69	yes	high	0.07	0.13
	Feng et al. 2024	0.70	yes	very high	0.13	0.17
Landsat 8/9	Liang 2000	0.62	yes	high	0.06	0.07
	Feng et al. 2024	0.41	no	-	0.16	0.17

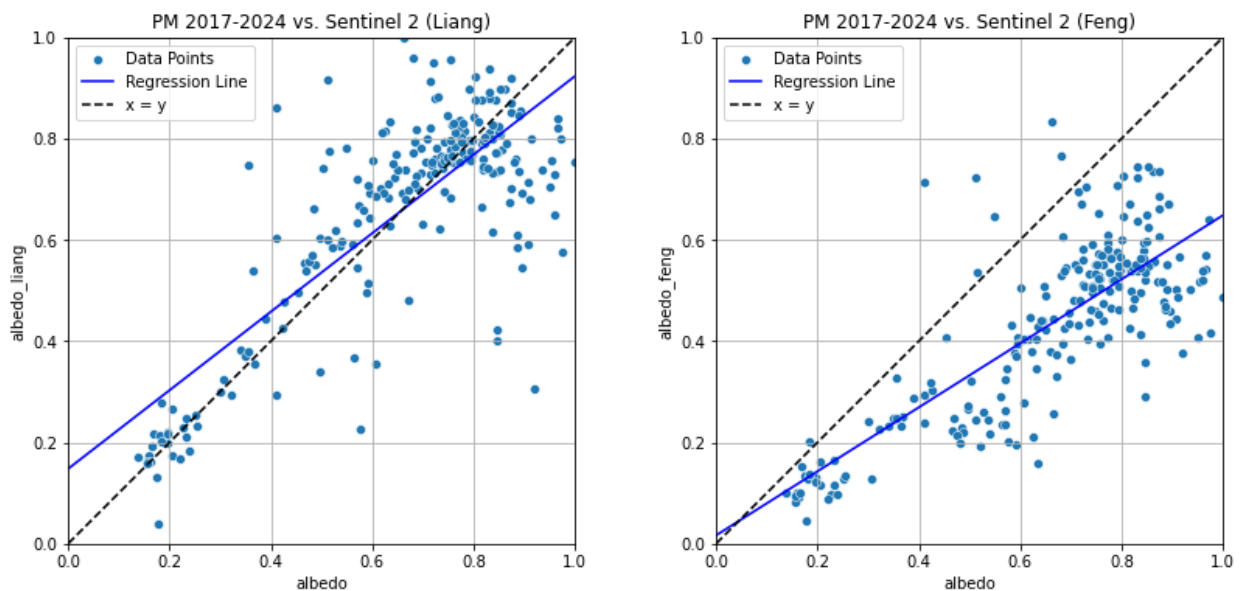


Figure 6.1: Albedo scatterplots for AWS Glacier de la Plaine Morte vs. S2 (2017—2024). The satellite albedo was calculated using Liang (2000)'s narrowband to broadband conversion (left) and Feng et al. (2024)'s conversion (right).

6.1.1.2 AWS Weissseespitze/Gepatschferner

The correlation between the AWS Weissseespitze/Gepatschferner albedo and S2 or L8/9 is low to moderate using all satellite observations. Furthermore, the error measures are quite large as shown in Table 6.3. For S2, Feng et al. (2024) shows better correlation results but also higher error measures. For L8/9, Liang (2000) shows better correlation results and has lower error measures.

The scatterplots in Figure 6.2 show that the dataset is dominated by large albedo values. Again, Feng et al. (2024) on the right shows a larger deviation from perfect agreement for higher albedo values around 0.7. Overall, however, the plots show a large scatter of the data. More so for lower albedo values. The larger values around 0.7 are more clustered around the $x=y$ line for Liang (2000) and below that line for Feng et al. (2024).

The correlation is better when only non-snow observations are used. However, only the results for S2 are significant. Feng et al. (2024) again has a higher correlation than Liang (2000), but also with larger error measures. In general, the error measures are large for both conversions.

Table 6.3: Correlation results of the AWS Weissseespitze/Gepatschferner albedo values with the satellite retrieved albedo values for pixels of all classes. The strength of correlation is highlighted in green and high errors (above 0.15) are shown in red.

Weissseespitze/Gepatschferner 2017-2023 (all observations)		Kendall's Tau	Significance $\alpha = 0.05$	Strength of Correlation	Mean Average Error	Root Mean Square Error
Sentinel 2	Liang 2000	0.21	yes	low	0.11	0.15
	Feng et al. 2024	0.25	yes	low	0.21	0.24
Landsat 8/9	Liang 2000	0.33	yes	moderate	0.17	0.20
	Feng et al. 2024	0.29	yes	low	0.22	0.27

Table 6.4: Correlation results of the AWS Weissseespitze/Gepatschferner albedo values with the satellite retrieved albedo values for pixels not classified as snow. The strength of correlation is highlighted in green and high errors (above 0.15) are shown in red.

Weissseespitze/Gepatschferner 2017-2023 (not snow)		Kendall's Tau	Significance $\alpha = 0.05$	Strength of Correlation	Mean Average Error	Root Mean Square Error
Sentinel 2	Liang 2000	0.42	yes	moderate	0.19	0.28
	Feng et al. 2024	0.57	yes	high	0.26	0.32
Landsat 8/9	Liang 2000	0.60	no	-	0.26	0.31
	Feng et al. 2024	0.47	no	-	0.43	0.48

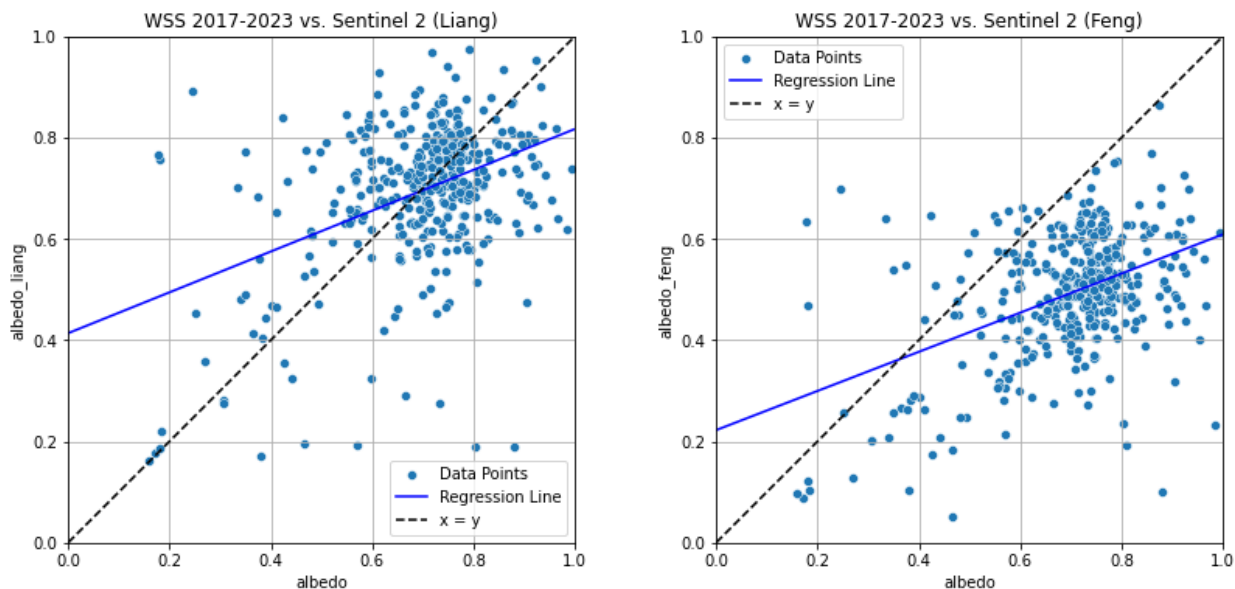


Figure 6.2: Albedo scatterplots for AWS Weisseespitze/Gepatschferner vs. S2 (2017—2024). The satellite albedo was calculated using Liang (2000)’s narrowband to broadband conversion (left) and Feng et al. (2024)’s conversion (right).

6.1.2 L8/9 albedo vs. S2 albedo

The results of the correlation analysis between L8/9 albedo and S2 albedo are shown in Figure 6.3. The orange dots show the mean Kendall’s Tau for each glacier. The values show a moderate correlation for all glaciers except Kanderfirn, where it is slightly lower. The three east-facing glaciers, Hintereisferner, Unteraargletscher, and Aletschgletscher, have the highest correlation values. Gepatschferner and Ghiacciaio dei Forni both have a northern aspect and lower correlation values. Rhonegletscher, with its south-westerly aspect, also has a comparatively low correlation. Kanderfirn has the lowest correlation value and an approximate western aspect.

All glaciers have higher mean Kendall’s Tau values when only observations with at least 50% of the maximum available pixels per glacier are used. These results are shown in blue in Figure 6.3. This difference is greater for the four glaciers Hintereisferner, Unteraargletscher, Grosser Aletschgletscher, and Rhonegletscher. The first three of these glaciers have a high correlation. Gepatschferner, Kanderfirn, and Ghiacciaio dei Forni do not show a large increase in correlation coefficient compared to using all observations. They already had the lowest correlation values when using all observations.

Hintereisferner is taken as an example of the eight glaciers. Figure 6.4 shows a day with a very high correlation (Kendall’s Tau = 0.80). The SW albedo is shown for both S2 and L8. The images look very similar in the darker parts of the glacier and differ only slightly in the brighter areas. S2 appears brighter in the light areas. The corresponding scatterplot is shown in Figure 6.6. The values are clustered close to the $x=y$ line for low albedos up to 0.3 and for high albedos from 0.6 to 1, but there is considerable scatter. The regression line shows that for higher albedos, S2 has higher values than L8.

Pixelwise Correlation Between Sentinel 2 and Landsat 8/9 Images Captured on the Same Day (2017–2024)

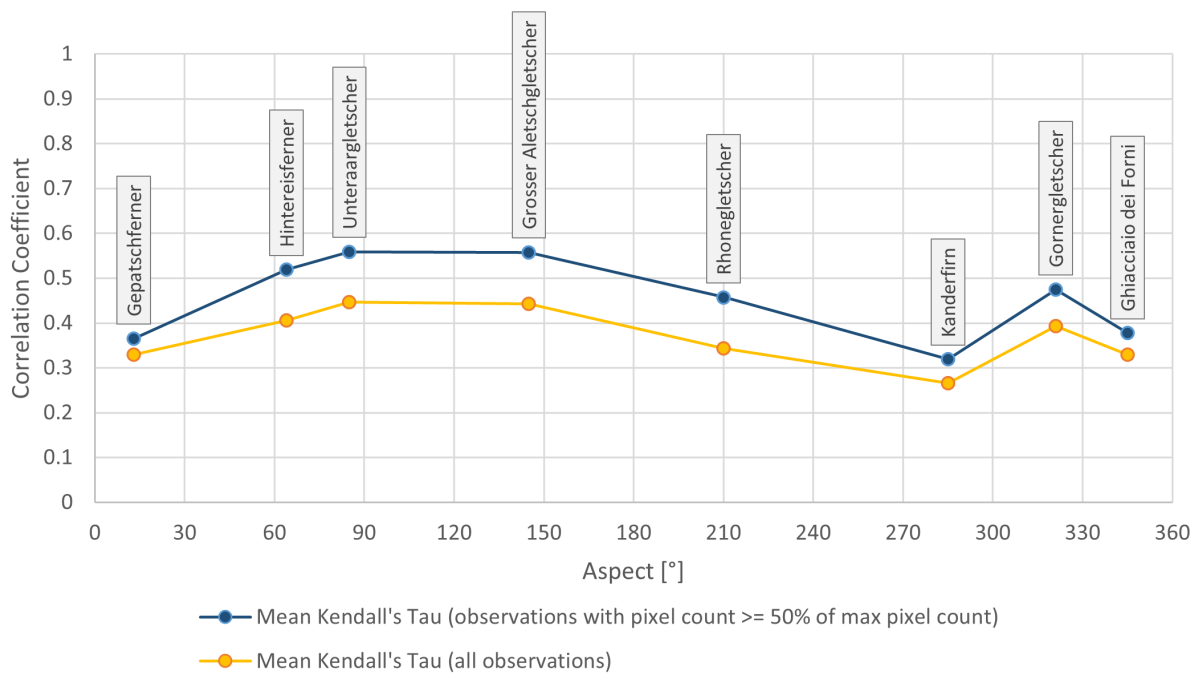


Figure 6.3: Pixelwise correlation results between S2 and L8/9 images (2017–2024). Orange points show the mean Kendall’s Tau for each glacier, while blue points represent the mean Kendall’s Tau for observations using at least 50% of the maximum available pixels per glacier, with pixel counts varying by glacier.

In Figure 6.5 a day with a low correlation between S2 and L8 is shown. The glacier has a mostly high albedo, except for the lowest regions in the north-east. For the rest of the glacier, the two images show opposite patterns, with brighter regions in one image appearing darker in the other. In general, the L8 image on the right appears brighter than the S2 image. This is the opposite of the image with a high correlation in Figure 6.4. The scatterplot for the bad correlation is shown in Figure 6.7. There is a lot of scatter in the data. Most of the data points have a high albedo. However, there is no clustering of points along the $x=y$ axis, but rather a dense cloud in the 0.7–0.9 albedo region on both axes.

Figure 6.8 shows the observations grouped by month with a monthly mean added. The values are lowest in the winter months from November to March. They are higher in summer with a peak in July. October has the second highest mean, closely followed by June.

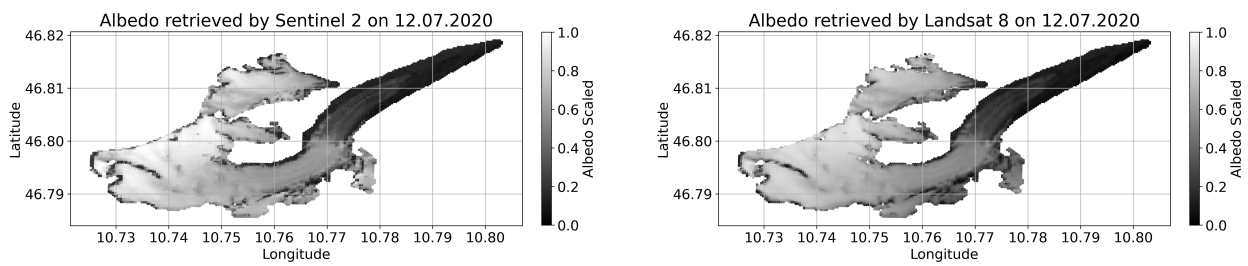


Figure 6.4: A comparison of SW albedo on Hintereisferner on 12 July 2020, captured by S2 (left) and L8 (right). This day demonstrates a very high correlation between the sensors (Kendall's Tau = 0.80).

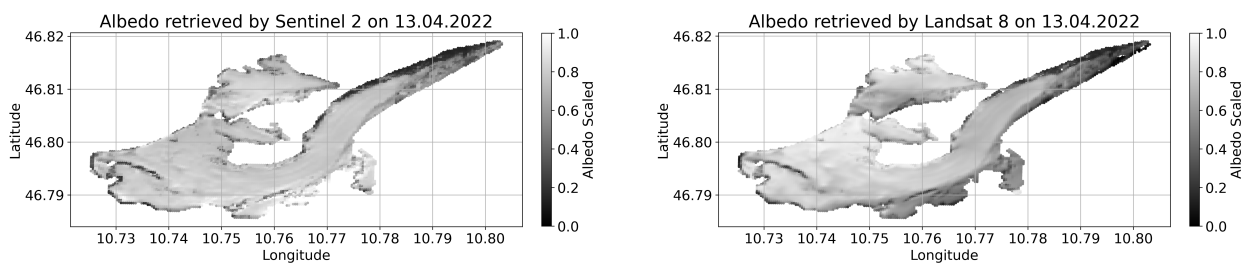


Figure 6.5: A comparison of SW albedo on Hintereisferner on 13 April 2022, captured by S2 (left) and L8 (right). This day demonstrates a low correlation between the sensors (Kendall's Tau = 0.17).

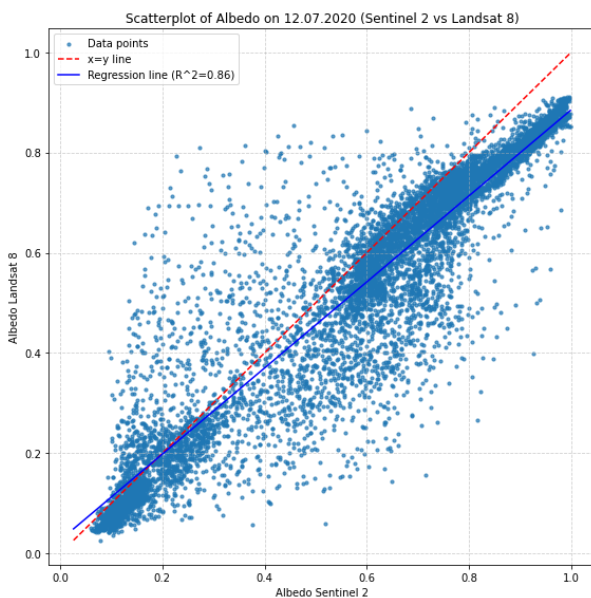


Figure 6.6: Scatterplot of SW albedo on Hintereisferner on 12 July 2020, captured by S2 and L8, showing a strong correlation (Kendall's Tau = 0.80).

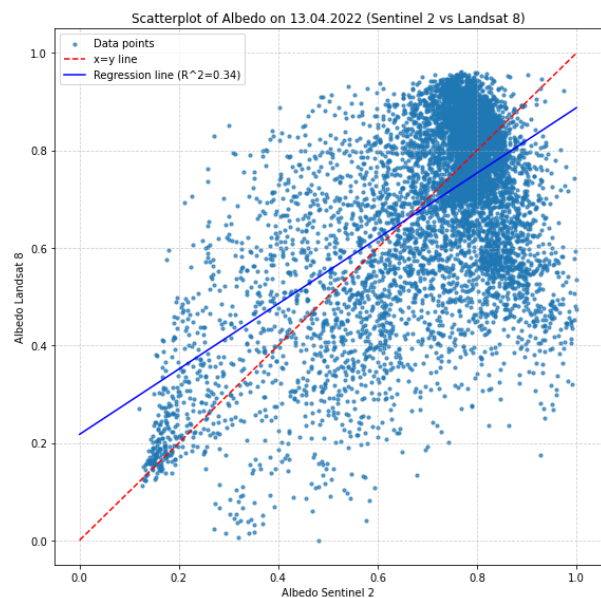


Figure 6.7: Scatterplot of SW albedo on Hintereisferner on 13 April 2022, captured by S2 and L8, showing a low correlation (Kendall's Tau = 0.17).

Monthly Pixelwise Correlation Between Sentinel 2 and Landsat 8/9 Images Captured on the Same Day (2017-2024) for Hintereisferner

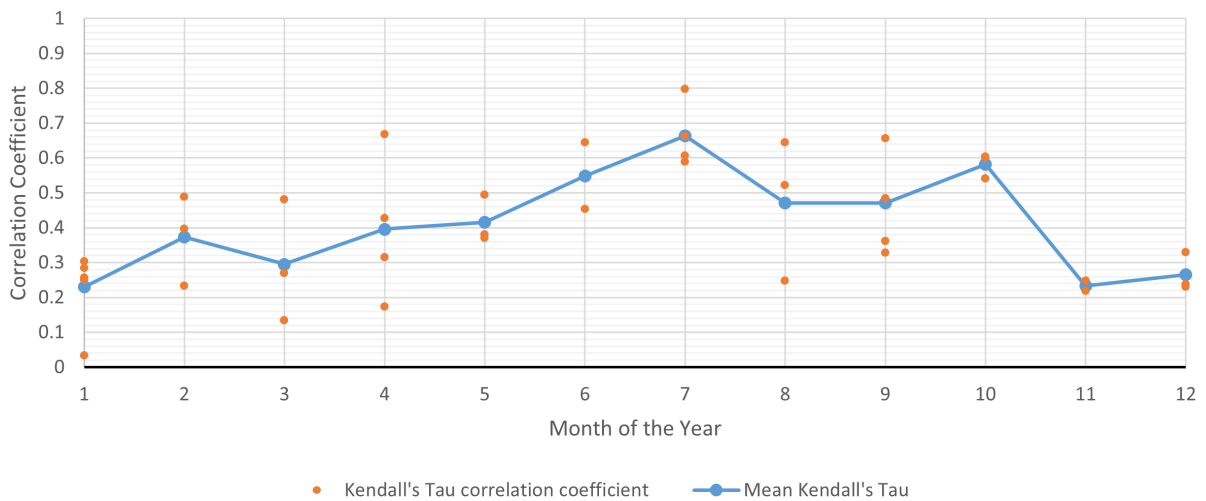


Figure 6.8: Pixelwise correlation results between S2 and L8/9 images (2017–2024) for Hintereisferner. Observations are grouped by month. Orange points show Kendall’s Tau for each observation, while blue points show the monthly mean Kendall’s Tau.

6.2 RQ2: Trend analysis

The results have been condensed to fit into a single table. The full results for each glacier can be found in the corresponding results section in the *Appendices* section B.

6.2.1 Sub-seasonal trends

No sub-seasonal trends are detected from 2013 to 2016. In 2017, Grosser Aletschgletscher, Gornergletscher, and Glacier Blanc all show sub-seasonal variability in about 20% of their elevation bands. In 2018, 14 out of 23 glaciers show sub-seasonal variability. Kanderfirn shows sub-seasonal albedo variability in 50% of its elevation bands and Grosser Aletschgletscher in 47%. Gornergletscher (38%), Gepatschferner (40%), and Hallstätter Gletscher (40%) are three other glaciers with a large number of bands with sub-seasonal variability.

From 2019 to 2021, seven to eight glaciers show elevation bands with sub-seasonal trends. In the following two years, 2022 and 2023, there are many glaciers with sub-seasonal albedo variabilities. A total of 15 glaciers show sub-seasonal variability in 2022. Ten glaciers show variability in more than two thirds of their elevation bands. The year 2023 has 17 glaciers with sub-seasonal albedo variability, the most of any year from 2013 to 2024. Five glaciers have 50% or more of their elevation bands affected by variability. In 2024 the number of glaciers with sub-seasonal albedo variability is reduced to seven. For five of them the percentage of affected bands is between 24% and 35%.

Grosser Aletschgletscher shows albedo variabilities for all years from 2018 to 2024. The results are visualised in Figure 6.9, where elevation bands with sub-seasonal albedo variability are shown in blue. For most years, the elevation bands in the middle sections show significant albedo variability. In 2018 and 2022, a large number of bands from the lower to the higher sections show albedo variability. 2023 shows a distinct pattern where only the elevation bands in the higher sections show significant albedo variability. Figure 6.10 shows the albedo variabilities for Unteraargletscher from 2018 to 2024. In 2018, 2021, and 2022 many bands in the middle section show albedo variabilities. In 2023, bands in higher sections show albedo variability, similar to Grosser Aletschgletscher in the same year.

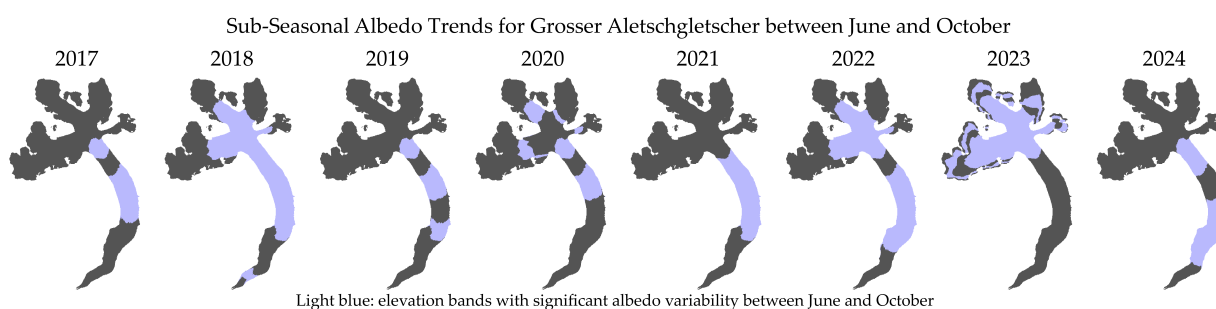


Figure 6.9: The results of the sub-seasonal trend analysis for Grosser Aletschgletscher for the years 2017 to 2024. The elevation bands that show significant albedo variability between June and October are shown in light blue.

Table 6.5: The sub-seasonal trends for each glacier as a percentage of elevation bands that show significant albedo differences within one year.

Glacier name	2013	2014	2015	2016	2017	2018	2019	2020	2021	2022	2023	2024
Glacier de la Plaine Morte	0%	0%	0%	0%	0%	0%	0%	0%	0%	0%	0%	0%
Kanderfirn	0%	0%	0%	0%	0%	50%	17%	0%	0%	33%	0%	0%
Unteraargletscher	0%	0%	0%	0%	0%	29%	7%	0%	29%	36%	21%	7%
Hüfirn	0%	0%	0%	0%	0%	27%	9%	18%	9%	18%	45%	0%
Ochsentaler Gletscher	0%	0%	0%	0%	0%	0%	0%	0%	0%	0%	0%	0%
Rhonegletscher	0%	0%	0%	0%	0%	0%	10%	0%	0%	40%	20%	0%
Grosser Aletschgletscher	0%	0%	0%	0%	18%	47%	18%	18%	29%	41%	29%	35%
Gornergletscher	0%	0%	0%	0%	19%	38%	0%	19%	6%	50%	44%	25%
Mer de Glace	0%	0%	0%	0%	0%	6%	0%	0%	0%	35%	6%	24%
Glacier Blanc	0%	0%	0%	0%	18%	9%	9%	0%	9%	45%	27%	27%
Ghiacciaio del Rutor	0%	0%	0%	0%	0%	0%	0%	0%	0%	0%	0%	0%
Vadrec del Forno	0%	0%	0%	0%	0%	13%	0%	13%	13%	13%	63%	13%
Ghiacciaio dei Forni	0%	0%	0%	0%	0%	13%	0%	0%	0%	25%	0%	0%
Ghiacciaio dell'Adamello	0%	0%	0%	0%	0%	17%	0%	83%	0%	67%	83%	0%
Vadret da Morteratsch	0%	0%	0%	0%	0%	0%	7%	7%	0%	36%	50%	0%
Gepatschferner	0%	0%	0%	0%	0%	40%	10%	10%	40%	10%	40%	30%
Hintereisferner	0%	0%	0%	0%	0%	11%	0%	44%	0%	33%	44%	0%
Gefrorene Wand Kees	0%	0%	0%	0%	0%	0%	0%	0%	0%	0%	80%	0%
Hallstätter Gletscher	0%	0%	0%	0%	0%	40%	0%	0%	0%	20%	40%	0%
Umbal Kees	0%	0%	0%	0%	0%	0%	0%	0%	0%	0%	0%	0%
Schlaten Kees	0%	0%	0%	0%	0%	20%	0%	0%	0%	0%	10%	0%
Pasterze	0%	0%	0%	0%	0%	0%	0%	10%	0%	0%	20%	0%
Hochalm Kees	0%	0%	0%	0%	0%	0%	0%	0%	0%	0%	67%	0%

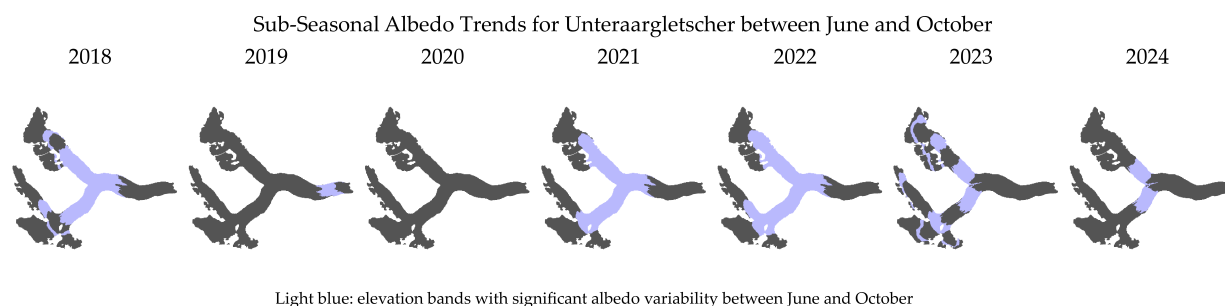


Figure 6.10: The results of the sub-seasonal trend analysis for Unteraargletscher for the years 2018 to 2024. The elevation bands that show significant albedo variability between June and October are shown in light blue.

6.2.2 Interannual trends

9 of the 23 glaciers have at least one elevation band in which an interannual albedo trend from 2013 to 2024 was detected. These nine glaciers are listed in Table 6.6. Positive values indicate increasing albedo, while negative values indicate decreasing albedo over time. Mer de Glace is the only glacier that shows a trend in June. It has a perfect negative trend of -1 for the elevation band at 1786.59–1886.59 m a.s.l. Hufifirn, Gornergletscher, Glacier Blanc, and Ghiacciaio dei Forni all show an albedo trend in one elevation band in August. All except Glacier Blanc show a strong trend of decreasing albedo, while Glacier Blanc shows a clear trend of increasing albedo. The trends are all detected in elevation bands above 2500 m a.s.l. The elevation band at Gornergletscher with a decreasing trend ranges from 2981.58 to 3081.58 m a.s.l. and is the only one to reach over 3000 m a.s.l. Most trends are recorded in September. Five glaciers each have one elevation band with an increase in albedo over the years. Gornergletscher has three elevation bands ranging from 2481.58 to 2781.58 m a.s.l., all of which show an increase in albedo. Over all glaciers, only positive trends are detected in September. In general, Mann-Kendall test result values range from 0.67 to a perfect correlation of 1, positive or negative. This indicates high to perfect correlations.

Table 6.6: Interannual trends for the glaciers with detected trends. For each trend result, the elevation band where it was detected is listed as well as the test coefficient. A positive value represents an increase of albedo over the years 2013–2024 while a negative value represents a decrease of albedo in the same time range.

Glacier name	June	July	August	September
Hüfifirn			2537.16 (-1.0)	
Grosser Aletschgletscher				2378.35 (0.71)
Gornergletscher			2981.58 (-0.79)	2481.58 (0.71) 2581.58 (0.86) 2681.58 (0.71)
Mer de Glace	1786.59 (-1.0)			2186.59 (0.71)
Glacier Blanc			2645.61 (0.67)	
Ghiacciaio dei Forni			2692.90 (-0.81)	
Vadret da Morteratsch				2704.46 (0.87)
Hintereisferner				2613.27 (1.0)
Hallstätter Gletscher				2290.61 (0.71)

6.3 RQ3: Drivers of albedo change

The results for the AWS Weissseespitze/Gepatschferner are shown in the corresponding results section in the *Appendices* section B. They are not discussed here because none of the results are significant and because of the small number of observations available for analysis. For the AWS Glacier de la Plaine Morte from 2014 to 2017, only a subset of the relevant results is shown. The full results can also be found in the corresponding results section in the *Appendices* section B.

6.3.1 AWS Glacier de la Plaine Morte

Significant relationships are found for mean air temperature, nightly minimum and maximum air temperature, and cumulative SW radiation at the AWS Glacier de la Plaine Morte from 2016 to 2024. The results are presented in Table 6.7. The mean air temperature metrics and the nighttime minimum and maximum show low correlations with the satellite-derived albedo. All the correlation coefficients are negative. Similar results can be seen for the AWS Glacier de la Plaine Morte 2014–2017. Only a small number of observations (7) were available for analysis. The mean air temperature shows significant results at $\alpha = 0.10$ for the 6h and 72h periods. The correlation is high for both time periods. With $\alpha = 0.15$, the 12h period also shows a significant result with a high correlation. The nighttime minimum air temperature also has a significant result with $\alpha = 0.10$, showing a high correlation.

The cumulative SW radiation for the AWS 2016–2024 shows a low correlation with the satellite-

retrieved albedo for the 6h and 24h time ranges. Moderate correlations are found for the 48h and 72h time periods. The 72h period has the highest correlation of all. As for the temperature metrics, all correlation coefficients are negative.

The correlation analysis for the air temperature range only shows significant results for 24h and 48h for $\alpha = 0.15$. However, the correlation is low for both. The negative air temperature hours are only tested with a small number of observations. They are significant for $\alpha = 0.10$. For the 12h and 24h periods the correlation is high, while for 48h it is moderate. The number of zero degree crossings is also only tested with a small number of observations. The results are significant for 12h ($\alpha = 0.10$) and 24h ($\alpha = 0.15$) showing a very high (12h) and a high (24h) correlation. The land surface temperature was only tested with 12 observations. The analysis results are not significant and no correlation was found.

Table 6.7: The results of the analysis of the drivers of albedo change for the AWS Glacier de la Plaine Morte for the years 2016–2024. This table shows the results for the station in place on the glacier since 2016.

Glacier de la Plaine Morte 2016-2024	Kendall's Tau	Significance $\alpha = 0.05$	Strength of Correlation	Number of Observations
Mean Temp. 6h	-0.24	yes	low	47
Mean Temp. 12h	-0.27	yes	low	47
Mean Temp. 24h	-0.26	yes	low	47
Mean Temp. 48h	-0.26	yes	low	47
Mean Temp. 72h	-0.26	yes	low	47
Temp. Range 12h	0.09	no	none	47
Temp. Range 24h	0.15	yes (0.15)	low	47
Temp. Range 48h	0.16	yes (0.15)	low	47
Neg. Temp. Hours 12h	0.69	yes (0.10)	high	6
Neg. Temp. Hours 24h	0.69	yes (0.10)	high	6
Neg. Temp. Hours 48h	0.48	yes (0.10)	moderate	9
Nighttime Min. Temp.	-0.28	yes	low	47
Nighttime Max. Temp.	-0.29	yes	low	47
Zero Deg. Cross. 12h	-0.77	yes (0.10)	very high	5
Zero Deg. Cross. 24h	-0.58	yes (0.15)	high	6
Zero Deg. Cross. 48h	0.15	no	low	9
Σ SW Rad. 6h	-0.29	yes	low	50
Σ SW Rad. 24h	-0.28	yes	low	50
Σ SW Rad. 48h	-0.31	yes	moderate	50
Σ SW Rad. 72h	-0.34	yes	moderate	50
Land Surf. Temp.	0.03	no	none	12

Table 6.8: The results of the analysis of the drivers of albedo change for the AWS Glacier de la Plaine Morte for the years 2014–2017. This table shows the results for the station that was on the glacier during the ablation periods 2014–2017.

Glacier de la Plaine Morte 2014-2017	Kendall's Tau	Significance $\alpha = 0.05$	Strength of Correlation	Number of Observations
Mean Temp. 6h	-0.62	yes (0.10)	high	7
Mean Temp. 12h	-0.52	yes (0.15)	high	7
Mean Temp. 24h	-0.43	no	moderate	7
Mean Temp. 48h	-0.43	no	moderate	7
Mean Temp. 72h	-0.62	yes (0.10)	high	7
Nighttime Min. Temp.	-0.62	yes (0.10)	high	7
Nighttime Max. Temp.	-0.43	no	moderate	7

6.3.2 AWS Hintereisferner

The metrics from the AWS Hintereisferner were used in combination with the elevation bands albedo dataset. Several elevation bands showed significant results. The elevation band at 2613–2713 m a.s.l. has the most significant results and is shown as an example.

The relationship between the mean albedo of the elevation band and the mean air temperature at the station shows significant results and a moderate correlation for all time periods. The correlation coefficient is slightly lower for 6h and 12h than for the others. The highest value is found for the 48h period (-0.35), closely followed by the 24h period (-0.34). The air temperature range of the last 12h, 24h, and 48h shows significant results but only a low correlation. The minimum and maximum nighttime air temperatures have very similar correlation coefficients. The minimum is classified as moderate correlation and the maximum as low correlation, but the difference is only 0.01. They are just at the transition from low to moderate correlation. The correlation coefficients for mean air temperature, air temperature range, and nighttime minimum and maximum air temperatures are all negative. For the zero degree crossings, only the 48h period has a significant result for $\alpha = 0.10$. At this level a low correlation is found. The other two time ranges do not show significant results.

The correlation results for the cumulative SW radiation all show a low correlation with very similar correlation coefficients for all time ranges. All coefficients are negative.

Table 6.9: The results of the analysis of the drivers of albedo change for the AWS Hintereisferner for the years 2013–2024. This table shows the results for the elevation band from 2613 to 2713 m a.s.l.

Hintereisferner 2613-2713 m a.s.l. 2013-2024	Kendall's Tau	Significance $\alpha = 0.05$	Strength of Correlation	Number of Observations
Mean Temp. 6h	-0.31	yes	moderate	139
Mean Temp. 12h	-0.30	yes	moderate	139
Mean Temp. 24h	-0.34	yes	moderate	138
Mean Temp. 48h	-0.35	yes	moderate	137
Mean Temp. 72h	-0.34	yes	moderate	137
Temp. Range 12h	-0.15	yes	low	139
Temp. Range 24h	-0.14	yes	low	138
Temp. Range 48h	-0.15	yes	low	137
Neg. Temp. Hours 12h	-	-	-	0
Neg. Temp. Hours 24h	-	-	-	0
Neg. Temp. Hours 48h	-	-	-	0
Nighttime Min. Temp.	-0.30	yes	moderate	139
Nighttime Max. Temp.	-0.29	yes	low	139
Zero Deg. Cross. 12h	0.11	no	low	21
Zero Deg. Cross. 24h	0.01	no	none	23
Zero Deg. Cross. 48h	0.20	yes (0.10)	low	40
Σ SW Rad. 6h	-0.20	yes	low	140
Σ SW Rad. 24h	-0.18	yes	low	140
Σ SW Rad. 48h	-0.20	yes	low	140
Σ SW Rad. 72h	-0.20	yes	low	140

7 Discussion

7.1 RQ1: Albedo comparison

The comparison of the different albedo datasets is addressed by the following research question:

- How well do bare-ice albedo observations from ground measurements, from Landsat 8/9, and from Sentinel 2 correlate with each other?

7.1.1 AWS albedo vs. satellite albedo

The correlation analysis between AWS albedo and satellite-retrieved albedo shows a clear relationship. The narrowband to broadband conversions of Liang (2000) and Feng et al. (2024) showed the best results for L8/9 and S2 independent of surface class. This was the case on Glacier de la Plaine Morte and Weissseespitze/Gepatschferner.

At AWS Glacier de la Plaine Morte, Feng et al. (2024) showed slightly better correlation results than Liang (2000) for S2 using all surface classes, whereas they were at the same level for L8/9 (Table 6.1). However, Feng et al. (2024) has much larger MAE and RMSE values. The scatterplots in Figure 6.1 show that there is a considerable amount of scatter in both datasets. This is captured by the large RMSE, which gives more weight to outliers, while the MAE gives equal weight to all errors (Chai and Draxler, 2014). Both conversions perform better when only non-snow observations are used (Table 6.2). Furthermore, the errors are smaller for these observations. Only Feng et al. (2024) using L8/9 data did not give a significant result.

The Liang (2000) conversion has been tested for its usefulness in several studies. Liang et al. (2003) validates the conversion through a correlation analysis with Landsat 7 data. The results are much better than those obtained in this thesis, but here L8/9 and S2 were used, which have different sensors. Traversa et al. (2021) carried out a validation for L8 and the use of the conversion for snow surfaces. They found a higher correlation and lower error terms. Their methods were slightly different as they first cleaned their data of anomalous data. They used data from different test sites and concluded that there were also differences from site to site. However, all the data from all the sites performed better than the data used in this thesis. Naegeli et al. (2017) also looked at the conversion by Liang (2000). They obtained better results for both L8 and S2. Their experimental

setup was different from the one used in this thesis, as they calculated the glacier-wide albedo for a bare ice summer scene per sensor. In this thesis, using only non-snow observations gave better results than when including snow observations as well. The scatterplots in Figure 6.1 also show that large scatter is mostly observed for high albedo values greater than 0.4.

Feng et al. (2024) did a validation for their conversion. They got better results, but only focused on summer albedo. They also mention the occurrence of more outliers for higher albedo values. However, the large error obtained in the analysis in this thesis remains without explanation. The scatterplot for Feng et al. (2024) in Figure 6.1 shows that high albedo values are largely underestimated. The Feng et al. (2024) conversion does not use the SWIR bands. Ice and snow both have low reflectance in the SWIR spectrum (Gore et al., 2019) but with slightly higher values for snow. The omission of the SWIR bands in Feng et al. (2024) may explain why the conversion performed similarly to Liang (2000) in the low albedo range (non-snow), but much worse in the high albedo range (snow). Inclusion of the SWIR band in the conversion may be beneficial for snow albedo calculations.

The analysis with AWS Weissseespitze/Gepatschferner data gave lower correlations and larger error values for all observations (Table 6.3) and for non-snow observations (Table 6.4). Feng et al. (2024) also performed better on S2 data and Liang (2000) on L8/9 data. The results for non-snow observations and L8/9 did not yield a significant correlation due to the low number of observations. The poorer correlation results and higher error values may be due to the large number of high albedo observations as seen in Figure 6.2. The station is located at a higher altitude than AWS Glacier de la Plaine Morte and therefore has a higher number of snow observations.

Both conversions yielded lower correlation coefficients than previous studies have shown. However, there are several possible factors that could explain the lower correlations found. Previous studies applied different preprocessing measures to the satellite data to exclude erroneous data (Feng et al., 2024; Naegeli et al., 2017; Traversa et al., 2021). Furthermore, the illumination angle was not considered, which could be a source of error due to the strong anisotropic scattering of snow and ice (König et al., 2001; Naegeli et al., 2017). This anisotropic behaviour is more pronounced in winters with large angles of solar incidence (Bindschadler et al., 2008; Rütte et al., 2021), which could explain why the inclusion of snow observations led to worse correlations and more scatter in the data. In addition, the atmospheric correction of satellite data tends to be more error-prone over bright targets (Kokhanovsky et al., 2020), introducing a further uncertainty for snow observations.

7.1.2 L8/9 albedo vs. S2 albedo

The moderate to high correlations found between L8/9 and S2 scenes acquired on the same day indicate that the sensors can be used in combination even for challenging targets such as snow and ice. The average correlation is better for all glaciers when using only observations where at least 50% of the maximum number of pixels were available for analysis (Figure 6.3). Scenes with lower pixel counts indicate the presence of clouds. Even after filtering for clouds and cloud shadows, the scenes may still be contaminated (Foga et al., 2017), which could lead to poorer correlation results. Clouds can change appearance quickly in the 20 minutes between the L8/9 and S2 passes. Figure 6.3 seems to show a pattern when the observed glaciers are sorted by aspect. The best correlations are observed for east-facing glaciers, while west-facing glaciers show the worst results. Snow and ice both scatter incoming radiation largely anisotropically with strong forward scattering (König et al., 2001; Rütte et al., 2021). This is even more pronounced for large solar zenith angles (SZA) (Bindschadler et al., 2008; Rütte et al., 2021). The sun illuminates the scenes from the east as the satellites pass the glaciers in the morning. The combination of eastern illumination and the slope of the glaciers could lead to larger local solar incidence angles for west-facing glaciers, while the local solar incidence angles would be smaller for east-facing glaciers. This could lead to more anisotropic scattering on west-facing glaciers. However, this hypothesis should be tested on more glaciers with either an eastern or western aspect.

Several studies have found good correlations between L8 and S2 (Arekhi et al., 2019; Li et al., 2018a; Mandanici and Bitelli, 2016). The results are generally better than those obtained in this thesis. However, there are possible explanations. They used different statistical measures. Kendall's Tau used in this thesis usually has lower values compared to other correlation coefficients such as Spearman's Rho or Pearson's R (Winter et al., 2016; Fredricks and Nelsen, 2007). They also did not use snow or ice surfaces for their tests. Snow and ice are difficult to measure correctly by satellites due to their anisotropic scattering (König et al., 2001; Rütte et al., 2021). The anisotropic scattering behaviour of both surfaces changes due to several factors such as wetness (Hannula and Pulliainen, 2019; Knap and Reijmer, 1998; König et al., 2001; Naegeli et al., 2017), surface roughness (Aoki et al., 2000; König et al., 2001), impurities (Aoki et al., 2000; Knap and Reijmer, 1998; Naegeli et al., 2017), and SZA (Aoki et al., 2000; Bindschadler et al., 2008). The complexity of the scattering functions may be a source of error for both surfaces and may explain the results obtained in this analysis.

The results from Hintereisferner are presented in more detail as an example and show a seasonal difference in the observed correlation. The best correlation was obtained on a summer day (Figure 6.4), when large parts of the glacier tongue were snow-free and had a low albedo. One of the worst correlations (Figure 6.5) was obtained in spring, when the glacier appears to be largely snow-covered except for some of the lowest parts of the ablation zone. Figure 6.8 shows that the correlation is usually better for summer observations compared to winter and spring. This could be due to the increased forward scattering for larger SZAs that occur in winter compared to sum-

mer when the Sun is closer to the zenith.

The scatterplots showing the good (Figure 6.6) and bad (Figure 6.7) correlation reveal that the correlation is better when there are more low albedo values below 0.4. Ice theoretically has a more anisotropic scattering behaviour than snow (Ji et al., 2022). However, the much higher albedo of snow could make a difference by making the backscatter from snow more difficult to capture correctly. The combination of high snow albedo, large forward scatter, and sloping terrain can lead to large amounts of terrain reflections, increasing the diffuse radiation measured by the sensor (Rütte et al., 2021). Diffuse radiation is a source of uncertainty because it causes the measured radiation to be higher than what is actually reflected by the surface directly.

In addition to scattering anisotropy and the SZA, several other sources of uncertainty could lead to lower correlation results. The processing of top-of-atmosphere (TOA) satellite data includes atmospheric correction. Different algorithms are used for L8/9 and S2 to provide the surface reflectance data for GEE. This could lead to different results, especially for difficult bright targets such as snow (Kokhanovsky et al., 2020). Furthermore, the surface reflectance data were not corrected for different local angles of solar incidence caused by the terrain slope (Bindschadler et al., 2008; Fugazza et al., 2016) and no compensation for the anisotropy effect was applied (Fugazza et al., 2016; Naegeli et al., 2017). Such preprocessing of the satellite data could prove beneficial and should be considered in further research to improve the correlation.

7.2 RQ2: Trend analysis

The discussion of the trend analysis addresses the following research question:

- What are the sub-seasonal and interannual trends in bare-ice albedo for the Alpine glaciers in Europe?

7.2.1 Sub-seasonal trends

The lack of sub-seasonal trends from 2013 to 2016 is most likely due to data availability. Only L8 was operational during these years. The lower number of available L8 scenes compared to S2 has already been mentioned in chapter 4. This is further supported by the appearance of sub-seasonal trends in 2017, when S2 started providing satellite imagery.

2018 is the first year in the analysis in which a large number of glaciers show sub-seasonal variability in albedo. 14 of the 23 glaciers analysed show significant albedo variability within the months of June to October. The 2018 ablation season started as usual in June. The summer months were characterised by unusually high temperatures and the strong melting continued into October (GLAMOS, 2020; MeteoSchweiz, 2019). The strong melting due to warm temperatures and the long ablation season could be two reasons why sub-seasonal albedo variabilities were found on many glaciers. The long exposure of bare ice allows more deposition of impurities (Fugazza et al.,

2019) as well as more weathering of the surface by meteorological factors (Naegeli et al., 2019). In addition, the altitude of the snow line can vary considerably from year to year (Naegeli et al., 2019). Regions that are normally above the snow line can become snow-free, revealing cleaner ice. Weathering and deposition of impurities will change the albedo, which could lead to significant differences. SLA is expected to increase in the future due to global warming (Naegeli and Huss, 2017), which could lead to surface darkening and more sub-seasonal albedo variability of ice at higher elevations.

The most sub-seasonal variabilities in bare-ice albedo are found in 2022 and 2023. 15 glaciers show significant albedo variability in 2022, followed by 17 glaciers in 2023, with 13 glaciers affected in both years. Both years were unusually warm (MeteoSchweiz, 2023; MeteoSchweiz, 2024). In Switzerland, warm temperatures and heat waves dominated the summer of 2022 from May onwards (MeteoSchweiz, 2023). Warm temperatures in May could have led to an early start of the ablation season, followed by strong melting during the heat waves. This explains why all Swiss glaciers used in the analysis, with the exception of Glacier de la Plaine Morte, show variability in bare-ice albedo in some of their elevation bands. Glacier de la Plaine Morte is a plateau glacier and covers a smaller elevation range than most other glaciers (Huss et al., 2013). This may be one reason why it behaves differently from the other glaciers extending over larger elevations.

2023 was another unusually warm year. Switzerland experienced a strong heat wave in August, with high temperatures recorded in the Alps (MeteoSchweiz, 2024). The warm temperatures will have increased glacier melt, leading to variability in the albedo of bare ice (Naegeli et al., 2019). These two years show the relationship between warm temperatures and sub-seasonal changes in bare-ice albedo. This is supported by the warm temperatures in 2018, when a large number of glaciers with significant bare-ice albedo variability were found. Warm temperatures seem to lead to more sub-seasonal variability, which is important to consider with ongoing global warming.

There seems to be a regional pattern in the selection of glaciers analysed. All glaciers in the Eastern Alps (numbers 18–23 in Figure 3.1) show less sub-seasonal albedo variability. Furthermore, all trend results, except Pasterze in 2020, are within the mentioned unusually warm years 2018, 2022, or 2023. This shows that the eastern glaciers are also affected by these anomalously warm temperatures, especially in 2023, but otherwise show less variability. A more comprehensive analysis of these eastern glaciers might reveal more about the sub-seasonal variability of the albedo of their ice.

The visual results of Grosser Aletschgletscher (Figure 6.9) and Unteraargletscher (Figure 6.10) seem to be consistent with the temperature anomalies mentioned above. The warm years 2018 and 2022 are associated with a high number of elevation bands showing sub-seasonal bare-ice albedo variability. 2023 appears to be slightly different. The lower regions seem to be less affected, while the bands at higher elevations show variability. On Grosser Aletschgletscher, high surface melt in 2018, 2022, and 2023 can also be seen in the largely negative summer mass balance (GLAMOS, 2024). The summer of 2022 had a particularly large negative summer mass balance and a very

high SLA. This was also the year with the second highest number of elevation bands showing sub-seasonal variability. Only 2018 had a higher number, for which the long ablation lasting into October could be one of the reasons.

The years 2019–2020 appear visually similar in terms of the number of bands affected by sub-seasonal variability. However, the summer mass balances were quite different, with 2019 having a number comparable to the warm summer of 2023, while the summer mass balance in 2021 was much less negative. Summer temperatures appear to be an important factor in the sub-seasonal albedo variability, but there is still uncertainty in the results. Several steps in the analysis could introduce uncertainty in the satellite albedo data used, such as cloud and cloud shadow filtering, narrowband to broadband albedo conversion, and bare ice classification. In addition, the use of elevation bands and their mean albedo could be less precise than when investigating sub-seasonal phenomena on a finer scale (Naegeli et al., 2019).

7.2.2 Interannual trends

There are no clear trend patterns, although several glaciers show an interannual trend in at least one elevation band. Mer de Glace is the only glacier showing a trend in June. A clear decreasing trend in bare-ice albedo was found in the lowest elevation band of those with enough observations for analysis. The three elevation bands at even lower elevations may no longer be on the glacier due to glacier retreat. The decreasing bare-ice albedo found could be due to the accumulation of light absorbing impurities over the years (Di Mauro and Fugazza, 2022). In addition, Di Mauro et al. (2017) found a trend towards an earlier start to the ablation season, which could lead to the lower June bare-ice albedo at Mer de Glace.

No trends were found in July, while four glaciers each have an elevation band with a trend of decreasing albedo in August. The accumulation of light absorbing impurities over the years could be responsible for this (Di Mauro and Fugazza, 2022). This is coupled with longer ablation seasons due to warmer temperatures. The surface is snow-free for longer, leading to more deposition of impurities on the bare ice surface (Fugazza et al., 2019), which accumulate over the years and lead to surface darkening.

Warmer temperatures could also be a temporary factor. Increased surface melt could lead to the formation of a thin film of water on the surface, reducing the albedo at the time the satellite image was taken (Naegeli et al., 2019).

Glacier Blanc shows a trend of increasing bare-ice albedo in August across one elevation band. An increase in bare-ice albedo in September is also observed for elevation bands on Grosser Aletschgletscher, Gornergletscher, Mer de Glace, Vadret da Morteratsch, Hintereisferner, and Hallstätter Gletscher. This is in contrast to the darkening of glacier ice observed on many European Alpine glaciers in several studies (Di Mauro and Fugazza, 2022; Fugazza et al., 2016; Fugazza et al., 2019; Naegeli et al., 2019). Di Mauro and Fugazza (2022) found an increase in the length of the ablation season across the European Alps in the study, but summer snowfall events could still lead to temporary increases in albedo. However, the surface must still be classified as snow to be

included in the analysis of this thesis. If the snow cover is thin enough or already melting, this could be the case.

In addition, the albedo captured by the satellite image is only a snapshot and does not necessarily represent the conditions on the glacier over a longer period of time. Glacier albedo is influenced by meteorological factors such as precipitation (rain or snow), air temperature, and the amount of received solar radiation in the days preceding the satellite image (Fugazza et al., 2016; Naegeli et al., 2019). These factors are highly variable in time and hinder the detection of long-term trends. In theory, the bare-ice albedo should be lowest at the end of September, which also marks the end of the ablation season. Brock et al. (2000) suggested that the albedo increase between the July and August observations was due to the removal of impurities by rainfall and subsequent run-off. However, it remains an open question why several elevation bands showed an increase in bare-ice albedo in September. A more detailed analysis of the late summer bare-ice albedo may explain the observed albedo increase in some elevation bands.

Most elevation bands across all glaciers showed no trends. The use of mean albedo per elevation band may be a reason for this. Naegeli et al. (2019) conducted their study on Landsat data from an even longer time frame (1999–2016) and still found trends only at the pixel level. Fugazza et al. (2019) also conducted their study using Landsat data at the pixel level and found some evidence of darkening. The elevation bands used in the analysis in this thesis may be too coarse to capture more subtle interannual trends. Another reason for the lack of significant trends could be the selection of satellite scenes. Fugazza et al. (2019) and Naegeli et al. (2019) both used a small selection of satellite images, whereas in this thesis the aim was to include as many scenes as possible. As mentioned above, cloud and cloud shadow filtering, narrowband to broadband albedo conversion, and lack of anisotropy and slope compensation could be other reasons for lack of results. A smaller selection of carefully preprocessed images could improve the results, but requires more time and effort, especially for a large scale analysis such as this. Furthermore, due to the large interannual variability of snow cover (Naegeli et al., 2019), robust trends may only be detected over longer time periods.

7.3 RQ3: Driver of albedo change

The research question guiding the analysis of the drivers of albedo change is the following:

- What surface properties and meteorological factors drive changes in the albedo of bare ice?

Land surface temperature was investigated as a surface property, while air temperature and SW radiation were investigated as meteorological factors. All three potential drivers are discussed separately.

7.3.1 Land Surface Temperature

No correlation was found between LST and ice albedo on Glacier de la Plaine Morte from 2016 to 2024. It should be noted that only 12 observations were available for this period, so data availability is an uncertainty for the result. The measured LST values are all around 273 Kelvin, with no notable pattern. One possible explanation could be the thermal structure of the glacier. If the ice is at melting point during the ablation season, the LST should always be around 273 Kelvin and not show large variations. Theoretically, glacier ice cannot be warmer than the melting point, as all excess energy is used for melting. Therefore, if the temperature of the glacier is at the melting point, the small differences in LST could also be partly due to scattered LW radiation and not correlated with changes in ice albedo. Glacier de la Plaine Morte often had positive air temperatures day and night during the ablation seasons 2016–2024. The resulting constant energy surplus keeps the ice surface at melting point and drives the melting of the ice. Even when temperatures were negative, they were usually not much below freezing and not for long. However, these findings are from the empirical record and different LST patterns could be found in further studies. The above findings from Glacier de la Plaine Morte could be extended to polythermal glaciers, which are common in the European Alps (Benn and Evans, 2010). This type of glacier is characterised by being largely composed of warm ice (at melting point), with only small sections of cold ice (below melting point) at the highest elevations in the accumulation area. Theoretically, warm ice with a surface at melting point should not show much variability in LST. Therefore, observing LST may not be a suitable metric for investigating the drivers of albedo change. Further research would be needed to provide a more conclusive answer.

7.3.2 Air temperature

The results for air temperature metrics as drivers of albedo change show low to moderate correlations, indicating a relationship. For Glacier de la Plaine Morte, mean air temperature and nighttime minimum and maximum air temperature showed a low correlation. Mean air temperature was not dependent on the time frame used, as the values are all very similar. Mean air temperature also gave significant results for the elevation band 2613–2713 m a.s.l. on Hintereisferner. The correlations are slightly better and can be classified as moderate. Furthermore, the mean air temperature shows a better correlation for longer time periods of 24h–72h. This could be an indication that looking at longer time periods helps to better capture albedo differences. For the AWS Glacier de la Plaine Morte stationed on the ice from 2014 to 2017, some mean air temperature metrics (6h, 12h, 72h) also show significant correlations at lower significance levels of 0.10 or 0.15. The observed correlations are all high, but due to the small number of observations, the validity of these results must be questioned. Nevertheless, they also support the usefulness of mean air temperature as a metric.

All mean air temperature correlation coefficients are negative, indicating that higher mean air temperatures correlate with lower albedo values. This is consistent with the assumption that higher air temperatures lead to surface melting, which lowers the albedo.

Temperature range as a metric showed only low correlations for all datasets tested. Furthermore, for Glacier de la Plaine Morte 2016–2024, the results were only significant for the 24h and 48h time ranges and $\alpha = 0.15$. It seems that the temperature range is less suitable for investigating air temperature as a driver of albedo change.

The nighttime minimum and maximum air temperature metrics resulted in higher correlation coefficients than the air temperature range. The results are close to the transition from low to moderate correlation for both the AWS Glacier de la Plaine Morte 2016–2024 and the AWS Hintereisferner. They seem to be able to capture albedo differences caused by the air temperature of the previous night. For AWS Glacier de la Plaine Morte 2016–2024, the correlation coefficients for nighttime temperatures are slightly higher than those for mean air temperature. The opposite is true for AWS Hintereisferner, where the mean air temperature metrics have slightly higher correlation coefficients. However, the differences are small and it seems that the mean air temperature and the nighttime minimum and maximum temperatures are equally suitable as metrics. The AWS Glacier de la Plaine Morte 2014–2017 showed a significant result for $\alpha = 0.10$ for the nighttime minimum temperature. A high correlation was found. As for all results from this station, only 7 observations were used for the analysis, which limits the validity of the results.

The number of hours with negative temperatures only yielded significant results for $\alpha = 0.10$ for AWS Glacier de la Plaine Morte 2016–2024. The analysis was limited to very few observations due to the generally warm air temperatures at Glacier de la Plaine Morte during the summer. The correlations for the 12h and 24h periods are both high, but with only six observations. For the 48h period, nine observations were used, resulting in a moderate correlation. For the AWS Hintereisferner no hours with negative temperatures were recorded. It seems that the metric of negative air temperature hours could be used to capture air temperature as a driver of albedo change, but it is better suited to glaciers that often experience negative air temperatures in summer. The number of zero degrees Celsius crossings shows a similar picture for AWS Glacier de la Plaine Morte. For the 12h and 24h time frames, the analysis resulted in very high ($\alpha = 0.10$) and high ($\alpha = 0.15$) correlations, but with a very low number of observations for both. The situation is quite different for AWS Hintereisferner, where more observations were available for analysis, but no significant correlation was detected for the 12h and 24h time frames. Only the 48h time frame showed a low correlation for $\alpha = 0.10$. The results for this metric are inconclusive. As for the negative temperature hours metric, it seems that an analysis on a glacier that often experiences negative air temperatures during the summer might give more conclusive results.

It appears that air temperature has a measurable effect on ice albedo and can be used as a meteorological factor driving changes in ice albedo. Mean air temperature and nighttime minima and maxima appear to be the most appropriate metrics for investigating air temperature as a driver. Careful preprocessing and validation of the satellite data used may be beneficial to the results of future studies. Uncertainties caused by different illumination geometries should be compensated for in the data. In addition, the albedo correlations between AWS and satellite imagery found in

this paper were not as good as those found in other studies. This uncertainty carries over to the analysis of albedo change drivers, as the satellite albedo may not capture the ground truth correctly.

Metrics involving negative temperatures do not seem to be suitable for the glaciers analysed, because of the warm air temperatures on the glaciers during summer. They may prove useful for glaciers where air temperatures often fall below zero degrees Celsius in summer.

7.3.3 SW radiation

Cumulative SW radiation has been found to have a measurable relationship with bare-ice albedo change. Theoretically, SW radiation is considered to be one of the most important drivers of glacier albedo change (Cuffey and Paterson, 2010). The cumulative SW radiation metric yielded significant results for AWS Glacier de la Plaine Morte 2016–2024 and for the Hintereisferner elevation band for all time periods considered. For AWS Glacier de la Plaine Morte, the correlation is stronger for the longer time ranges, which may indicate that monitoring SW radiation over a longer time frame better captures albedo change. This pattern is not present for the elevation band of Hintereisferner, where all correlation coefficients indicate a low correlation. However, as albedo is highly spatially variable (Benn and Evans, 2010), it is possible that the approach of using the mean albedo of the elevation band coupled with off-ice AWS data fails to capture albedo variability. Nevertheless, a relationship between cumulative SW radiation and albedo was found and the usability of off-ice data could be tested in further work.

7.4 Limitations

Preprocessed satellite data present a limitation to the analysis due to the accompanying uncertainties. Cloud detection and the processing to achieve surface reflectance data work well in general but do have their limitations. This is also the case for the classification employed which yielded good results but had difficulties in some cases. These three factors are discussed separately in the following.

7.4.1 Cloud detection

Cloud detection can be a difficult task, especially over bright targets such as snow and some ice surfaces. Foga et al. (2017) examined the CFMask algorithm for L8. They found high commission errors for these surfaces, meaning that snow and ice were misclassified as clouds in some cases. The opposite was true for cloud shadows, which had higher omission errors, i.e., they were not detected. Newer methods, such as the one used to produce the CloudScore+ dataset for S2, give better results compared to the FMask approach (Pasquarella et al., 2023). However, it is important to remember that cloud detection is never perfect and leaves some uncertainty in the data.

7.4.2 Surface reflectance

The use of surface reflectance data always introduces uncertainty into the analysis through atmospheric correction. To obtain a surface reflectance product, TOA data must be processed to bottom-of-atmosphere (BOA) level. This involves correcting for atmospheric effects such as aerosols and water vapour. This step is performed by Sen2Cor for S2 and the Land Surface Reflectance Code (LaSRC) for L8/9. Li et al. (2018a) evaluated the performance of Sen2Cor for S2 data and found a general overestimation of surface reflectance. Due to incorrectly retrieved aerosol optical thickness (AOT) and water vapour (WV), the surface reflectances produced by Sen2Cor are typically higher than ground measurements. This is the case for all bands and especially over bright targets where the AOT and WV retrieval is more erroneous (Li et al., 2018a; Kokhanovsky et al., 2020). This is particularly relevant when working with snow/ice surfaces, as is done in this thesis. In addition, it was found that the two algorithms perform differently at different SZAs. They perform worse for large SZAs such as in winter (Chen and Zhu, 2022). Varying topography can increase the effect of the low sun if the local angle of solar incidence is even larger due to sloping terrain. This could limit the correct retrieval of surface reflectance, particularly in winter. There seems to be a lack of studies validating surface reflectance products specifically for snow and ice surfaces. This would be interesting as both targets are difficult to capture correctly.

7.4.3 Classification

Classification of the satellite images was difficult over some of the darker ice areas. This was particularly evident at the location of AWS Weissseespitze/Gepatschferner. The station was located on bare ice due to high ablation rates on the glacier during the last few ablation seasons, when the glacier was completely snow-free. However, during this time no observations were classified as ice, only as other classes (unclassified, water, snow shadow, cloud). Most of the observations that appeared to be misclassified were classified as "unclassified" or "water". "Unclassified" is the result of inconclusive spectral signatures where the classification could not assign a class to the pixels. For the "water" pixels, it appears that in some cases dark ice was misclassified as water. Dirty ice has a low reflectance (see Table 2.1) and in summer, liquid water can form a film on the surface, further lowering the albedo by changing the reflectance function. This could lead to the spectral signature being identified as water. Nevertheless, on Glacier de la Plaine Morte the classification gave much better results for ice and it also worked to retrieve mean bare-ice albedo values for the elevation bands. Therefore, the results on AWS Weissseespitze/Gepatschferner should be investigated further.

8 Conclusion

The focus of this thesis was on investigating bare-ice albedo on European Alpine Glaciers. Three research questions were posed at the beginning to achieve that objective:

RQ1 How well do bare-ice albedo observations from ground measurements, from Landsat 8/9, and from Sentinel 2 correlate with each other?

RQ2 What are the sub-seasonal and interannual trends in bare-ice albedo for the Alpine glaciers in Europe?

RQ3 What surface properties and meteorological factors drive changes in the albedo of bare ice?

The first part of RQ1 was to investigate how well bare-ice albedo observations from AWS ground measurements correlate with satellite albedo. High correlations were found on Glacier de la Plaine Morte, suggesting that satellite data can be used to estimate bare-ice albedo on glaciers. Furthermore, the narrowband to broadband albedo conversion of Liang (2000) gave the best results and is a reliable albedo conversion for narrowband satellite data. The results at AWS Weissseespitze/Gepatschferner showed lower correlations, which could be due to the high number of snow observations. In addition, snow surfaces were more difficult for satellites to detect correctly. The high snow albedo values showed more scatter, which could be due to the anisotropic scattering behaviour of snow, and more difficulties in atmospheric correction over bright targets. For further work, it is advisable to correct the data for illumination effects and to carefully select the bare-ice scenes by hand to eliminate the classification as an uncertainty. Nevertheless, the results show that satellite albedo products can be used to estimate bare-ice albedo well. The albedo can be used as an input parameter for glacier mass balance modelling for remote monitoring of glaciers.

The second part of RQ1 was to examine the correlation between Landsat 8/9 and Sentinel 2 data. They correlate well, but show some seasonal differences. Correlations are higher during the ablation season, when more of the glacier surface is snow-free. In winter, snow cover and large solar zenith angles seem to limit the correlation. In addition, east-facing glaciers have better results than west-facing glaciers, which could be investigated in further studies. Correcting the satellite data for anisotropy effects and illumination angles to remove these factors as uncertainties would

be recommended for further work. Nevertheless, the results obtained show that Landsat 8/9 and Sentinel 2 data can be used in combination, especially for retrieving bare-ice albedo during the ablation season.

RQ2 is concerned with detecting sub-seasonal and interannual trends in bare-ice albedo for European Alpine glaciers. The analysis of sub-seasonal bare-ice albedo variability showed that prolonged warm temperatures in the ablation season lead to more variability. This pattern is observed in all Alpine regions. However, in years without such high temperatures, glaciers in the Eastern Alps show less variability than the other glaciers in the study area. This regional difference could be the focus of further studies. In general, monitoring sub-seasonal bare-ice variability on glaciers seems to be an interesting topic for the future, especially considering the warming climate and the expected large impacts on glaciers. The results of this thesis show that bare-ice albedo should not be modelled as a constant throughout an ablation season. Ignoring albedo variability would distort the results of mass balance models.

Only a few glaciers had elevation bands with detectable interannual trends. Decreasing bare-ice albedo in June and August could be attributed to surface deposition of impurities. In addition, an earlier start to the ablation season could enhance this effect in June. Longer ablation seasons, which are expected in the future, will keep the surface snow-free for a longer period of time and expose the bare ice to more deposition of impurities. The observed albedo increases in September remain an open question. The influence of meteorological factors at the time the satellite images were acquired could be one explanation. Another reason may be the scale, as the use of elevation bands may be too coarse for smaller scale trends. Further work may benefit from performing the analysis at the pixel level, as has been done previously. It might also be useful to focus on a smaller region and devote more resources to preprocessing satellite data to obtain clean and verified bare-ice data.

Returning to RQ2, sub-seasonal variability in bare-ice albedo is found on many glaciers and should be taken into account in mass balance models. Furthermore, even at the scale of elevation bands, there are discernible interannual trends, some of which are consistent with reported ongoing glacier ice darkening. Both results highlight the importance of glacier monitoring to detect ongoing trends and make accurate predictions for the future.

For the final research question RQ3, different metrics were used to investigate the factors driving changes in the albedo of bare ice. Air temperature and SW radiation were identified as important drivers. The most useful metrics were mean air temperature, nighttime minimum and maximum air temperature, and cumulative SW radiation. There is no clear pattern as to which time periods are most appropriate. However, longer time frames of 24-72 hours tend to show slightly better correlation results. It should also be noted that air temperature and SW radiation metrics showed a relationship with bare-ice albedo when off-ice AWS data were used in combination with elevation band mean albedo. This may be useful for glaciers where an AWS is stationed close to, but not on the glacier. Further work could investigate the best performing metrics from this analysis and the impact of different time periods to see if longer time periods are preferable. Also, more

off-ice AWS could be used to test the validity of this approach.

As far as the other metrics are concerned, the LST and air temperature metrics that include negative temperatures do not seem to be suitable as metrics. The former because of the warm ice on the glaciers studied and the latter because of the generally warm air temperatures during the ablation seasons. They may be more useful in colder climates where the ice is cooler and may show more temperature variability. Air temperature and SW radiation were confirmed as drivers of bare-ice albedo change, despite the limited availability of satellite data. These findings could be used to extend the work to more glaciers with available weather stations to test which metrics work best to capture bare-ice albedo change.

This thesis shows the importance of monitoring glaciers due to the variability of the bare-ice albedo. Capturing this variability is essential to achieve better results in glacier change modelling. Satellite remote sensing is well suited for the task as it is less time consuming than field work, allows large study areas to be examined, and is very accessible as satellite data from the Landsat and Sentinel missions are freely available. Combining satellite data with AWS data is a useful approach to validating results. Not only can AWS data be used to validate the satellite data, in combination the satellite images provide snapshots of the conditions on the glacier at that moment, while the accompanying AWS data can provide complementary information about the meteorological circumstances leading up to those snapshots.

Bibliography

- Aoki, T., Aoki, T., Fukabori, M., Hachikubo, A., Tachibana, Y., and Nishio, F. (2000). "Effects of snow physical parameters on spectral albedo and bidirectional reflectance of snow surface." *Journal of Geophysical Research* 105 (D8), pp. 10219–10236. DOI: 10.1029/1999JD901122.
- Arekhi, M., Goksel, C., Balik Sanli, F., and Senel, G. (2019). "Comparative Evaluation of the Spectral and Spatial Consistency of Sentinel-2 and Landsat-8 OLI Data for Igneada Longos Forest." *ISPRS International Journal of Geo-Information* 8 (2), p. 56. DOI: 10.3390/ijgi8020056.
- Baldo, A. (2024). "Surface energy balance and melt events at Weißseespitze ice core site / by Anna Baldo." MA thesis. Innsbruck: Universität Innsbruck. URL: <https://ulb-dok.uibk.ac.at/ulbtirolhs/content/titleinfo/9818821> (Accessed: 28.01.2025).
- Barandun, M., Bravo, C., Grobety, B., Jenk, T., Fang, L., Naegeli, K., Rivera, A., Cisternas, S., Münster, T., and Schwikowski, M. (2022). "Anthropogenic influence on surface changes at the Olivares glaciers; Central Chile." *Science of The Total Environment* 833, p. 155068. DOI: 10.1016/j.scitotenv.2022.155068.
- Benn, D. I. and Evans, D. J. A. (2010). *Glaciers & glaciation*. 2nd ed. London: Hodder education.
- Bindschadler, R., Vornberger, P., Fleming, A., Fox, A., Mullins, J., Binnie, D., Paulsen, S. J., Granne-man, B., and Gorodetzky, D. (2008). "The Landsat Image Mosaic of Antarctica." *Remote Sensing of Environment* 112 (12), pp. 4214–4226. DOI: 10.1016/j.rse.2008.07.006.
- Bonafoni, S. and Sekertekin, A. (2020). "Albedo Retrieval From Sentinel-2 by New Narrow-to-Broadband Conversion Coefficients." *IEEE Geoscience and Remote Sensing Letters* 17 (9), pp. 1618–1622. DOI: 10.1109/LGRS.2020.2967085.
- Brock, B. W., Willis, I. C., and Sharp, M. J. (2000). "Measurement and parameterization of albedo variations at Haut Glacier d’Arolla, Switzerland." *Journal of Glaciology* 46 (155), pp. 675–688. DOI: 10.3189/172756500781832675.
- Cabral Júnior, J. B. and Lucena, R. L. (2020). "Analysis of Precipitation using Mann-Kendall and Kruskal-Wallis Non-Parametric Tests." *Mercator (Fortaleza)* 19. URL: <https://www.scielo.br/j/mercator/a/SbktK54ZrRRWsXdcrH9PQYj/?lang=en> (Accessed: 21.08.2024).
- Chai, T. and Draxler, R. R. (2014). "Root mean square error (RMSE) or mean absolute error (MAE)? – Arguments against avoiding RMSE in the literature." *Geoscientific Model Development* 7, pp. 1247–1250. DOI: 10.5194/gmd-7-1247-2014.
- Chen, J. and Zhu, W. (2022). "Comparing Landsat-8 and Sentinel-2 top of atmosphere and surface reflectance in high latitude regions: case study in Alaska." *Geocarto International* 37 (20), pp. 6052–6071. DOI: 10.1080/10106049.2021.1924295.

- Cook, J., Edwards, A., Takeuchi, N., and Irvine-Fynn, T. (2016). "Cryoconite: The dark biological secret of the cryosphere." *Progress in Physical Geography: Earth and Environment* 40 (1), pp. 66–111. DOI: 10.1177/0309133315616574.
- Croux, C. and Dehon, C. (2010). "Influence functions of the Spearman and Kendall correlation measures." *Statistical Methods & Applications* 19, pp. 497–515. DOI: 10.1007/s10260-010-0142-z.
- Cuffey, K. and Paterson, W. S. B. (2010). *The physics of glaciers*. 4th ed. Burlington, MA: Butterworth-Heinemann/Elsevier.
- Davaze, L., Rabatel, A., Arnaud, Y., Sirguey, P., Six, D., Letreguilly, A., and Dumont, M. (2018). "Monitoring glacier albedo as a proxy to derive summer and annual surface mass balances from optical remote-sensing data." *The Cryosphere* 12, pp. 271–286. DOI: 10.5194/tc-12-271-2018.
- Di Mauro, B., Baccolo, G., Garzonio, R., Giardino, C., Massabò, D., Piazzalunga, A., Rossini, M., and Colombo, R. (2017). "Impact of impurities and cryoconite on the optical properties of the Morteratsch Glacier (Swiss Alps)." *The Cryosphere* 11, pp. 2393–2409. DOI: 10.5194/tc-11-2393-2017.
- Di Mauro, B. and Fugazza, D. (2022). "Pan-Alpine glacier phenology reveals lowering albedo and increase in ablation season length." *Remote Sensing of Environment* 279, p. 113119. DOI: 10.1016/j.rse.2022.113119.
- European Space Agency (n.d.[a]). *S2 Mission*. URL: <https://sentiwiki.copernicus.eu/web/s2-mission> (Accessed: 04.01.2025).
- (n.d.[b]). *Sentinel-2*. URL: https://www.esa.int/Applications/Observing_the_Earth/Copernicus/Sentinel-2 (Accessed: 04.01.2025).
- (2015). *Sentinel-2 User Handbook*. URL: https://sentinel.esa.int/documents/247904/685211/Sentinel-2_User_Handbook (Accessed: 17.09.2024).
- European Space Agency and Airbus (2022). *Copernicus DEM*. DOI: 10.5270/ESA-c5d3d65.
- Feng, S., Cook, J. M., Anesio, A. M., Benning, L. G., and Tranter, M. (2023). "Long time series (1984–2020) of albedo variations on the Greenland ice sheet from harmonized Landsat and Sentinel 2 imagery." *Journal of Glaciology* 69 (277), pp. 1225–1240. DOI: 10.1017/jog.2023.11.
- Feng, S., Cook, J. M., Onuma, Y., Naegeli, K., Tan, W., Anesio, A. M., Benning, L. G., and Tranter, M. (2024). "Remote sensing of ice albedo using harmonized Landsat and Sentinel 2 datasets: validation." *International Journal of Remote Sensing* 45 (19-20), pp. 7724–7752. DOI: 10.1080/01431161.2023.2291000.
- Foga, S., Scaramuzza, P. L., Guo, S., Zhu, Z., Dilley, R. D., Beckmann, T., Schmidt, G. L., Dwyer, J. L., Joseph Hughes, M., and Laue, B. (2017). "Cloud detection algorithm comparison and validation for operational Landsat data products." *Remote Sensing of Environment* 194, pp. 379–390. DOI: 10.1016/j.rse.2017.03.026.
- Fredricks, G. A. and Nelsen, R. B. (2007). "On the relationship between Spearman's rho and Kendall's tau for pairs of continuous random variables." *Journal of Statistical Planning and Inference* 137 (7), pp. 2143–2150. DOI: 10.1016/j.jspi.2006.06.045.
- Fugazza, D., Senese, A., Azzoni, R. S., Maugeri, M., and Diolaiuti, G. A. (2016). "Spatial distribution of surface albedo at the Forni Glacier (Stelvio National Park, Central Italian Alps)." *Cold Regions Science and Technology* 125, pp. 128–137. DOI: 10.1016/j.coldregions.2016.02.006.

- Fugazza, D., Senese, A., Azzoni, R. S., Maugeri, M., Maragno, D., and Diolaiuti, G. A. (2019). "New evidence of glacier darkening in the Ortles-Cevedale group from Landsat observations." *Global and Planetary Change* 178, pp. 35–45. DOI: 10.1016/j.gloplacha.2019.04.014.
- GLAMOS (2020). "The Swiss Glaciers 2017/18 and 2018/19: Glaciological Report No. 139/140." *Glaciological Report No. 139/140 of the Cryospheric Commission of the Swiss Academy of Sciences (SC-NAT)*. Ed. by A. Buder, M. Huss, and A. Linsbauer, p. 155. DOI: 10.18752/GLREP_139-140.
- (2024). *Swiss Glacier Mass Balance (release 2024)*. DOI: 10.18750/MASSBALANCE.2024.R2024.
- Gore, A., Mani, S., R.P., H., Shekhar, C., and Ganju, A. (2019). "Glacier surface characteristics derivation and monitoring using Hyperspectral datasets: a case study of Gepang Gath glacier, Western Himalaya." *Geocarto International* 34 (1), pp. 23–42. DOI: 10.1080/10106049.2017.1357766.
- Gugerli, R., Salzmann, N., Huss, M., and Desilets, D. (2019). "Continuous and autonomous snow water equivalent measurements by a cosmic ray sensor on an alpine glacier." *The Cryosphere* 13 (12), pp. 3413–3434. DOI: 10.5194/tc-13-3413-2019.
- Hannula, H.-R. and Pulliainen, J. (2019). "Spectral reflectance behavior of different boreal snow types." *Journal of Glaciology* 65 (254), pp. 926–939. DOI: 10.1017/jog.2019.68.
- Hock, R. and Huss, M. (2021). "Chapter 9 - Glaciers and climate change." *Climate Change (Third Edition)*. Ed. by T. M. Letcher. Elsevier, pp. 157–176. DOI: 10.1016/B978-0-12-821575-3.00009-8.
- Huss, M., Voinesco, A., and Hoelzle, M. (2013). "Implications of climate change on Glacier de la Plaine Morte, Switzerland." *Geographica Helvetica* 68, pp. 227–237. DOI: 10.5194/gh-68-227-2013.
- Ji, W., Hao, X., Shao, D., Yang, Q., Wang, J., Li, H., and Huang, G. (2022). "A New Index for Snow/Ice/Ice-Snow Discrimination Based on BRDF Characteristic Observation Data." *Journal of Geophysical Research: Atmospheres* 127 (3), e2021JD035742. DOI: 10.1029/2021JD035742.
- Johnson, E. and Rupper, S. (2020). "An Examination of Physical Processes That Trigger the Albedo-Feedback on Glacier Surfaces and Implications for Regional Glacier Mass Balance Across High Mountain Asia." *Frontiers Earth Science* 8 (129). DOI: 10.3389/feart.2020.00129.
- Jouvet, G., Huss, M., Funk, M., and Blatter, H. (2011). "Modelling the retreat of Grosser Aletschgletscher, Switzerland, in a changing climate." *Journal of Glaciology* 57 (206), pp. 1033–1045. DOI: 10.3189/002214311798843359.
- Knap, W. H. and Reijmer, C. H. (1998). "Anisotropy of the Reflected Radiation Field Over Melting Glacier Ice: Measurements in Landsat TM Bands 2 and 4." *Remote Sensing of Environment* 65 (1), pp. 93–104. DOI: 10.1016/S0034-4257(98)00015-7.
- Kokhanovsky, A., Box, J. E., Vandecrux, B., Mankoff, K. D., Lamare, M., Smirnov, A., and Kern, M. (2020). "The Determination of Snow Albedo from Satellite Measurements Using Fast Atmospheric Correction Technique." *Remote Sensing* 12 (2), p. 234. DOI: 10.3390/rs12020234.
- Kruskal, W. H. and Wallis, W. A. (1952). "Use of Ranks in One-Criterion Variance Analysis." *Journal of the American Statistical Association* 47 (260), pp. 583–621. DOI: 10.2307/2280779.
- König, M., Winther, J.-G., and Isaksson, E. (2001). "Measuring snow and glacier ice properties from satellite." *Reviews of Geophysics* 39 (1), pp. 1–27. DOI: 10.1029/1999RG000076.

- Landsat Missions (n.d.). *CFMask Algorithm*. URL: <https://www.usgs.gov/landsat-missions/cfmask-algorithm> (Accessed: 06.01.2025).
- Lehner, B. and Grill, G. (2013). "Global river hydrography and network routing: baseline data and new approaches to study the world's large river systems." *Hydrological Processes* 27 (15), pp. 2171–2186. DOI: 10.1002/hyp.9740.
- Li, Y., Chen, J., Ma, Q., Zhang, H. K., and Liu, J. (2018a). "Evaluation of Sentinel-2A Surface Reflectance Derived Using Sen2Cor in North America." *IEEE Journal of Selected Topics in Applied Earth Observations and Remote Sensing* 11 (6), pp. 1997–2021. DOI: 10.1109/JSTARS.2018.2835823.
- Li, Z., Erb, A., Sun, Q., Liu, Y., Shuai, Y., Wang, Z., Boucher, P., and Schaaf, C. (2018b). "Preliminary assessment of 20-m surface albedo retrievals from Sentinel-2A surface reflectance and MODIS/VIIRS surface anisotropy measures." *Remote Sensing of Environment* 217, pp. 352–365. DOI: 10.1016/j.rse.2018.08.025.
- Liang, S. (2000). "Narrowband to broadband conversions of land surface albedo I Algorithms." *Remote Sensing of Environment* 76 (2), pp. 213–238. DOI: 10.1016/S0034-4257(00)00205-4.
- Liang, S., Shuey, C. J., Russ, A. L., Fang, H., Chen, M., Walthall, C. L., Daughtry, C. S., and Hunt, R. (2003). "Narrowband to broadband conversions of land surface albedo: II. Validation." *Remote Sensing of Environment* 84 (1), pp. 25–41. DOI: 10.1016/S0034-4257(02)00068-8.
- Mandanici, E. and Bitelli, G. (2016). "Preliminary Comparison of Sentinel-2 and Landsat 8 Imagery for a Combined Use." *Remote Sensing* 8 (12), p. 1014. DOI: 10.3390/rs8121014.
- Meals, D. W., Spooner, J., Dressing, S. A., and Harcum, J. B. (2011). *Statistical Analysis for Monotonic Trends (Tech Notes 6)*. Tech. rep. Fairfax, VA: Developed for U.S. Environmental Protection Agency by Tetra Tech, Inc. URL: <https://www.epa.gov/polluted-runoff-nonpoint-source-pollution/nonpoint-source-monitoringtechnical-notes>.
- MeteoSchweiz (2019). *Klimareport 2018*. Tech. rep. Zürich: Bundesamt für Meteorologie und Klimatologie MeteoSchweiz, p. 94.
- (2023). *Klimareport 2022*. Tech. rep. Zürich: Bundesamt für Meteorologie und Klimatologie MeteoSchweiz, p. 104.
- (2024). *Klimareport 2023*. Tech. rep. Zürich: Bundesamt für Meteorologie und Klimatologie MeteoSchweiz, p. 100.
- Naegeli, K. (2017). "State, Changes and Impact of Glacier Surface Albedo in the Swiss Alps." *Alpine Cryosphere and Geomorphology Studies* 5.
- Naegeli, K., Damm, A., Huss, M., Schaepman, M., and Hoelzle, M. (2015). "Imaging spectroscopy to assess the composition of ice surface materials and their impact on glacier mass balance." *Remote Sensing of Environment* 168, pp. 388–402. DOI: 10.1016/j.rse.2015.07.006.
- Naegeli, K., Damm, A., Huss, M., Wulf, H., Schaepman, M., and Hoelzle, M. (2017). "Cross-Comparison of Albedo Products for Glacier Surfaces Derived from Airborne and Satellite (Sentinel-2 and Landsat 8) Optical Data." *Remote Sensing* 9 (2), p. 110. DOI: 10.3390/rs9020110.
- Naegeli, K. and Huss, M. (2017). "Sensitivity of mountain glacier mass balance to changes in bare-ice albedo." *Annals of Glaciology* 58 (75pt2), pp. 119–129. DOI: 10.1017/aog.2017.25.
- Naegeli, K., Huss, M., and Hoelzle, M. (2019). "Change detection of bare-ice albedo in the Swiss Alps." *The Cryosphere* 13, pp. 397–412. DOI: 10.5194/tc-13-397-2019.

- Neeti, N. and Eastman, J. R. (2011). "A Contextual Mann-Kendall Approach for the Assessment of Trend Significance in Image Time Series." *Transactions in GIS* 15 (5), pp. 599–611. DOI: 10.1111/j.1467-9671.2011.01280.x.
- Oerlemans, J., Giesen, R., and Van Den Broeke, M. (2009). "Retreating alpine glaciers: increased melt rates due to accumulation of dust (Vadret da Morteratsch, Switzerland)." *Journal of Glaciology* 55 (192), pp. 729–736. DOI: 10.3189/002214309789470969.
- Olmedo, G. F., Ortega-Farías, S., Fuente-Sáiz, D. de la, Fonseca-Luego, D., and Fuentes-Peñailillo, F. (2016). "water: Tools and Functions to Estimate Actual Evapotranspiration Using Land Surface Energy Balance Models in R." *The R Journal* 8 (2), pp. 352–369. DOI: 10.32614/RJ-2016-051.
- Pasquarella, V. (2023). *All Clear with Cloud Score+*. URL: <https://medium.com/google-earth/all-clear-with-cloud-score-bd6ee2e2235e> (Accessed: 06.01.2025).
- Pasquarella, V. J., Brown, C. F., Czerwinski, W., and Rucklidge, W. J. (2023). "Comprehensive quality assessment of optical satellite imagery using weakly supervised video learning." *2023 IEEE/CVF Conference on Computer Vision and Pattern Recognition Workshops (CVPRW)*. Vancouver, BC, Canada: IEEE, pp. 2125–2135. DOI: 10.1109/CVPRW59228.2023.00206.
- Paul, F., Rastner, P., Azzoni, R. S., Diolaiuti, G., Fugazza, D., Le Bris, R., Nemec, J., Rabatel, A., Ramusovic, M., Schwaizer, G., and Smiraglia, C. (2019). *Glacier inventory of the Alps from Sentinel-2, shape files*. DOI: 10.1594/PANGAEA.909133.
- (2020). "Glacier shrinkage in the Alps continues unabated as revealed by a new glacier inventory from Sentinel-2." *Earth System Science Data* 12 (3), pp. 1805–1821. DOI: 10.5194/essd-12-1805-2020.
- RGI 7.0 Consortium (2023). *Randolph Glacier Inventory - A Dataset of Global Glacier Outlines, Version 7.0*. DOI: 10.5067/F6JMOVY5NAVZ.
- Ritter, F., Fiebig, M., and Muhar, A. (2012). "Impacts of Global Warming on Mountaineering: A Classification of Phenomena Affecting the Alpine Trail Network." *Mountain Research and Development* 32 (1), pp. 4–15. DOI: 10.1659/MRD-JOURNAL-D-11-00036.1.
- Rounce, D. R., Hock, R., Maussion, F., Hugonnet, R., Kochtitzky, W., Huss, M., Berthier, E., Brinkerhoff, D., Compagno, L., Copland, L., Farinotti, D., Menounos, B., and McNabb, R. W. (2023). "Global glacier change in the 21st century: Every increase in temperature matters." *Science* 379 (6627), pp. 78–83. DOI: 10.1126/science.abo1324.
- Rütte, F. von, Kahl, A., Rohrer, J., and Lehning, M. (2021). "How Forward-Scattering Snow and Terrain Change the Alpine Radiation Balance With Application to Solar Panels." *Journal of Geophysical Research: Atmospheres* 126 (15), e2020JD034333. DOI: 10.1029/2020JD034333.
- Schaeffer, M. S. and Levitt, E. E. (1956). "Concerning Kendall's tau, a nonparametric correlation coefficient." *Psychological Bulletin* 53 (4), pp. 338–346. DOI: 10.1037/h0045013.
- Sexton, D. J., Bentz, M. L., Welsh, R. M., Derado, G., Furin, W., Rose, L. J., Noble-Wang, J., Pacilli, M., McPherson, T. D., Black, S., Kemble, S. K., Herzegh, O., Ahmad, A., Forsberg, K., Jackson, B., and Litvintseva, A. P. (2021). "Positive Correlation Between Candida auris Skin-Colonization Burden and Environmental Contamination at a Ventilator-Capable Skilled Nursing Facility in Chicago." *Clinical Infectious Diseases* 73 (7), pp. 1142–1148. DOI: 10.1093/cid/ciab327.

- Shih, C.-L. and Hung, T.-Y. (2020). *Comparison of statistical methods for analysis of small sample sizes for detecting the differences in efficacy between treatments for knee osteoarthritis*. DOI: 10.21203/rs.2.20859/v1.
- Sommer, C., Malz, P., Seehaus, T. C., Lippl, S., Zemp, M., and Braun, M. H. (2020). "Rapid glacier retreat and downwasting throughout the European Alps in the early 21st century." *Nature Communications* 11, p. 3209. DOI: 10.1038/s41467-020-16818-0.
- Tedstone, A. J., Cook, J. M., Williamson, C. J., Hofer, S., McCutcheon, J., Irvine-Fynn, T., Gribbin, T., and Tranter, M. (2020). "Algal growth and weathering crust state drive variability in western Greenland Ice Sheet ice albedo." *The Cryosphere* 14, pp. 521–538. DOI: 10.5194/tc-14-521-2020.
- Traversa, G., Fugazza, D., Senese, A., and Frezzotti, M. (2021). "Landsat 8 OLI Broadband Albedo Validation in Antarctica and Greenland." *Remote Sensing* 13 (4), p. 799. DOI: 10.3390/rs13040799.
- Ultee, L., Coats, S., and Mackay, J. (2022). "Glacial runoff buffers droughts through the 21st century." *Earth System Dynamics* 13, pp. 935–959. DOI: 10.5194/esd-13-935-2022.
- U.S. Geological Survey (2019). *Landsat 8 (L8) Data Users Handbook*. URL: <https://www.usgs.gov/landsat-missions/landsat-8-data-users-handbook> (Accessed: 17.09.2024).
- (2022). *Landsat 9 Data Users Handbook*. URL: <https://www.usgs.gov/media/files/landsat-9-data-users-handbook> (Accessed: 17.09.2024).
- Winter, J. C. F. de, Gosling, S. D., and Potter, J. (2016). "Comparing the Pearson and Spearman correlation coefficients across distributions and sample sizes: A tutorial using simulations and empirical data." *Psychological Methods* 21 (3), pp. 273–290. DOI: 10.1037/met0000079.
- Yu, P.-S., Yang, T.-C., and Kuo, C.-C. (2006). "Evaluating Long-Term Trends in Annual and Seasonal Precipitation in Taiwan." *Water Resources Management* 20, pp. 1007–1023. DOI: 10.1007/s11269-006-9020-8.
- Zhu, Z. and Woodcock, C. E. (2012). "Object-based cloud and cloud shadow detection in Landsat imagery." *Remote Sensing of Environment* 118, pp. 83–94. DOI: 10.1016/j.rse.2011.10.028.
- Žebre, M., Colucci, R. R., Giorgi, F., Glasser, N. F., Racoviteanu, A. E., and Del Gobbo, C. (2021). "200 years of equilibrium-line altitude variability across the European Alps (19012100)." *Climate Dynamics* 56, pp. 1183–1201. DOI: 10.1007/s00382-020-05525-7.

A Data

A.1 AWS Glacier de la Plaine Morte

The data from the ablation periods 2014–2017 is from Dr. Kathrin Naegeli within the scope of her PhD thesis at the University of Fribourg (Naegeli, 2017) and the **SEON project**.

Table 1: Data gaps in the record of the AWS on the Glacier de la Plaine Morte during the 2014-2017 ablation periods.

Recording Periods	Data Gaps Air temperature		Data Gaps SW Radiation	
	09.07.2014 - 28.09.2014	16.07.	1 record	16.07.
02.07.2015 - 23.08.2015		no missing records		no missing records
04.07.2016 - 06.10.2016	04.-05.07. 06.-19.07. 02.08.	66 records 1'893 records 13 records	04.-05.07. 06.-19.07. 02.08.	66 records 1'893 records 13 records
06.07.2017 - 19.09.2017	06.-07.07. 11.-13.07.	99 records 276 records	06.-07.07. 11.-13.07.	99 records 276 records

The AWS data for 2016-2024 is from Gugerli et al. (2019).

Table 2: Data gaps in the record of the AWS on the Glacier de la Plaine Morte from October 2016 to date.

Recording Periods	Data Gaps Air temperature		Data Gaps SW Radiation	
	03.10.2016 - 11.10.2017	05.10.16 18.-20.10.16	8 records 49 records	no records
11.10.2017 - 24.05.2024	11.-27.10.17 16.05.-19.06.19 02.07.-22.09.19 05.11.-18.12.19 15.-22.02.23 22.02.-16.03.23 25.05.-01.09.23 29.03.-05.04.24 30.04.-13.05.24 13.-24.05.24	375 records 815 records 1'987 records 1'023 records nights 525 records 2'365 records nights nights 260 records	02.07.-15.08.19 16.08.-22.09.19 23.02.-16.03.23	1'067 records 901 records 511 records

A.2 AWS Weissseespitze/Gepatschferner

The AWS Weissseespitze on the Hintereisferner is managed by the Institut für interdisziplinäre Gebirgsforschung, Universität Innsbruck. Data from 2017 to 2021 is freely available on **PAN-GAEA**. I received the data for 2017-2023 directly from Anna Baldo who used the data for her **Master's Thesis** in 2024 at University of Innsbruck.

Table 3: Data gaps in the record of the AWS on the Gepatschferner from October 2016 to date.

Recording Periods	Data Gaps		Data Gaps	
	Air temperature		SW Radiation	
31.10.2017 - 31.10.2023	17.-18.12.17	124 records	17.-18.12.17	124 records
	11.-18.11.18	1'003 records	11.-18.11.18	1'003 records
	18.-29.11.18	1'572 records	18.-29.11.18	1'572 records
	09.-12.12.18	407 records	09.-12.12.18	407 records
	07.-08.01.19	106 records	07.-08.01.19	106 records
	08.-12.01.19	529 records	08.-12.01.19	529 records
	12.-13.01.19	132 records	12.-13.01.19	132 records
	13.-14.01.19	122 records	13.-14.01.19	122 records
	14.-16.01.19	276 records	14.-16.01.19	276 records
	24.08.-01.10.19	5'541 records	24.08.-01.10.19	5'541 records
	14.05.-09.06.23	3'697 records	14.05.-09.06.23	3'697 records

A.3 AWS Hintereisferner

The AWS on the Hintereisferner is managed by the Department of Atmospheric and Cryospheric Sciences, Universität Innsbruck. The raw data used in this thesis is available at this [link](#).

Table 4: Data gaps in the record of the AWS next to the Hintereisferner from June 2013 to October 2024.

Recording Periods	Data Gaps	
	Air temperature	
01.06.2013 -	04.10.13-15.03.14	23'345 records
01.10.2020	23.08.-05.09.15	1'809 records
	16.-19.09.15	486 records
	06.05.-25.08.16	15'978 records
	10.-12.09.17	185 records
	13.-14.09.17	204 records
	21.09.-09.10.18	2'493 records
	21.01.-16.02.19	3'715 records
	10.06.-04.07.19	3'510 records
	27.-28.11.19	186 records
	29.-30.11.19	101 records
	13.-30.12.19	2'482 records
10.11.2020 -	11.11.20	144 records
31.10.2024	03.-05.04.21	419 records
	13.-14.05.21	221 records
	11.09.21	143 records
	26.09.21	143 records
	20.10.21	118 records

B Results

B.1 RQ1: Albedo comparison

B.1.1 AWS albedo vs. satellite albedo

Table 5: AWS vs. satellite albedo for pixels of all classes.

Correlation between AWS and Satellite retrieved SW albedo using different narrowband to broadband conversions											
	Landsat 8/9			Sentinel 2							
Narrowband to Broadband SW Albedo Conversion	Liang 2000	Feng et al. 2024	Olmedo et al. 2017	Liang 2000	Liang 2000 3x3 NBHD	Feng et al. 2024	Feng et al. 2024 NBHD	3x3	Bonafoni and Sekertekin 2020	Li et al. 2018 Snow Conditions	Li et al. 2018 Snowfree Conditions
	AWS Plaine Morte Ablation Periods 2014–2017			AWS Plaine Morte Ablation Period 2017							
No. of observations	7			3							
Kendall's Tau Correlation Coefficient	0.619	0.810	0.619	0.333	0.333	1.000	0.333	0.333	1.000	0.333	
$\alpha = 0.05$	no	yes	no	no	no	no	no	no	no	no	
MAE	0.032	0.155	0.039	0.062	0.070	0.144	0.147	0.061	0.043	0.043	
RMSE	0.044	0.165	0.055	0.068	0.078	0.173	0.167	0.068	0.043	0.047	
	AWS Plaine Morte Oct. 2017 – May 2024			AWS Plaine Morte Oct. 2017 – May 2024							
No. of observations	82			194							
Kendall's Tau Correlation Coefficient	0.58	0.58	0.58	0.53	0.53	0.59	0.59	0.52	0.53	0.53	
$\alpha = 0.05$	yes	yes	yes	yes	yes	yes	yes	yes	yes	yes	
MAE	0.10	0.24	0.10	0.08	0.08	0.23	0.23	0.08	0.08	0.09	
RMSE	0.12	0.26	0.13	0.12	0.12	0.25	0.25	0.12	0.12	0.13	
	AWS Weissseespitze Nov. 2017 – Oct. 2023			AWS Weissseespitze Nov. 2017 – Oct. 2023							
No. of observations	63			340							
Kendall's Tau Correlation Coefficient	0.33	0.29	0.33	0.22	0.21	0.25	0.25	0.21	0.23	0.22	
$\alpha = 0.05$	yes	yes	yes	yes	yes	yes	yes	yes	yes	yes	
MAE	0.17	0.22	0.19	0.11	0.11	0.21	0.21	0.11	0.10	0.12	
RMSE	0.20	0.27	0.22	0.15	0.15	0.24	0.24	0.15	0.14	0.16	

Table 6: AWS vs. satellite albedo for non-snow pixels.

Correlation between AWS and satellite retrieved SW non-snow class albedo using different narrowband to broadband conversions											
	Landsat 8/9			Sentinel 2							
Narrowband to Broadband SW Albedo Conversion	Liang 2000	Feng et al. 2024	Olmedo et al. 2017	Liang 2000	Liang 2000 3x3 NBHD	Feng et al. 2024	Feng et al. 2024 NBHD	3x3	Bonafoni and Sekertekin 2020	Li et al. 2018 Snow Conditions	Li et al. 2018 Snowfree Conditions
	AWS Plaine Morte Ablation Periods 2014–2017			AWS Plaine Morte Ablation Period 2017							
No. of observations	5			2							
Kendall's Tau Correlation Coefficient	0.20	0.60	0.20	-1.00	-1.00	1.00	-1.00	-1.00	1.00	-1.00	
$\alpha = 0.05$	no	no	no	no	no	no	no	no	no	no	
MAE	0.02	0.12	0.02	0.04	0.05	0.08	0.09	0.04	0.04	0.05	
RMSE	0.02	0.12	0.02	0.05	0.05	0.08	0.09	0.05	0.04	0.05	
	AWS Plaine Morte Oct. 2017 – May 2024			AWS Plaine Morte Oct. 2017 – May 2024							
No. of observations	13			36							
Kendall's Tau Correlation Coefficient	0.62	0.41	0.59	0.68	0.69	0.61	0.70	0.67	0.67	0.67	
$\alpha = 0.05$	yes	no	yes	yes	yes	yes	yes	yes	yes	yes	
MAE	0.06	0.16	0.05	0.07	0.07	0.13	0.13	0.07	0.07	0.08	
RMSE	0.07	0.17	0.06	0.13	0.13	0.18	0.17	0.13	0.13	0.15	
	AWS Weissseespitze Nov. 2017 – Oct. 2023			AWS Weissseespitze Nov. 2017 – Oct. 2023							
No. of observations	6			14							
Kendall's Tau Correlation Coefficient	0.60	0.47	0.60	0.44	0.42	0.49	0.57	0.42	0.38	0.42	
$\alpha = 0.05$	no	no	no	yes	yes	yes	yes	yes	no	yes	
MAE	0.26	0.43	0.25	0.19	0.19	0.25	0.26	0.19	0.20	0.21	
RMSE	0.31	0.48	0.30	0.28	0.28	0.32	0.32	0.28	0.28	0.29	

Table 7: AWS vs. satellite albedo for snow class pixels.

Correlation between AWS and satellite retrieved SW snow class albedo using different narrowband to broadband conversions										
	Landsat 8/9			Sentinel 2						
Narrowband to Broadband SW Albedo Conversion	Liang 2000	Feng et al. 2024	Olmedo et al. 2017	Liang 2000	Liang 2000 3x3 NBHD	Feng et al. 2024	Feng et al. 2024 3x3 NBHD	Bonafoni and Sekertekin 2020	Li et al. 2018 Snow Conditions	Li et al. 2018 Snowfree Conditions
	AWS Plaine Morte Ablation Periods 2014–2017			AWS Plaine Morte Ablation Period 2017						
No. of observations	2			1						
Kendall's Tau Correlation Coefficient	1.00	1.00	1.00	-	-	-	-	-	-	-
$\alpha = 0.05$	<i>no</i>	<i>no</i>	<i>no</i>	-	-	-	-	-	-	-
MAE	0.06	0.24	0.09	0.10	0.11	0.28	0.26	0.10	0.04	0.03
RMSE	0.07	0.24	0.10	0.10	0.11	0.28	0.26	0.10	0.04	0.03
	AWS Plaine Morte Oct. 2017 – May 2024			AWS Plaine Morte Oct. 2017 – May 2024						
No. of observations	69			158						
Kendall's Tau Correlation Coefficient	0.42	0.43	0.42	0.36	0.36	0.46	0.46	0.35	0.36	0.36
$\alpha = 0.05$	<i>yes</i>	<i>yes</i>	<i>yes</i>	<i>yes</i>	<i>yes</i>	<i>yes</i>	<i>yes</i>	<i>yes</i>	<i>yes</i>	<i>yes</i>
MAE	0.10	0.25	0.12	0.09	0.09	0.25	0.25	0.09	0.08	0.09
RMSE	0.13	0.27	0.14	0.12	0.12	0.27	0.27	0.12	0.12	0.13
	AWS Weissseespitze Nov. 2017 – Oct. 2023			AWS Weissseespitze Nov. 2017 – Oct. 2023						
No. of observations	57			326						
Kendall's Tau Correlation Coefficient	0.34	0.27	0.34	0.18	0.18	0.22	0.22	0.18	0.19	0.18
$\alpha = 0.05$	<i>yes</i>	<i>yes</i>	<i>yes</i>	<i>yes</i>	<i>yes</i>	<i>yes</i>	<i>yes</i>	<i>yes</i>	<i>yes</i>	<i>yes</i>
MAE	0.16	0.20	0.18	0.10	0.10	0.21	0.21	0.10	0.10	0.11
RMSE	0.19	0.24	0.21	0.14	0.14	0.24	0.24	0.14	0.14	0.15

B.2 RQ2: Glacier trends

B.2.1 Glacier de la Plaine Morte

Glacier de la Plaine Morte (CH)

22.08.2023

Sentinel 2 accessed with GEE

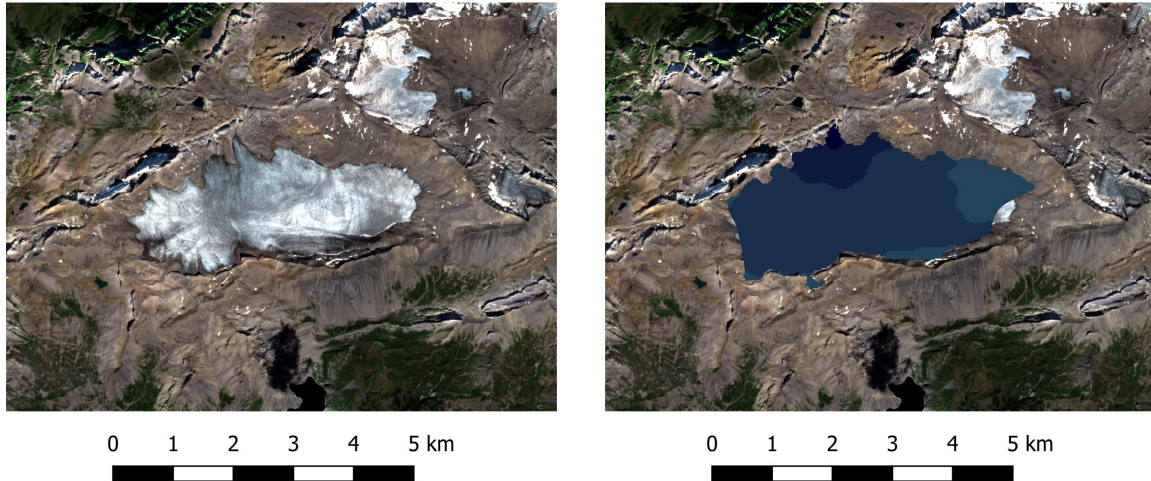


Figure 1: Satellite image of Glacier de la Plaine Morte (left image) and the elevation bands used for the trend analysis in different shades of blue (right image). The darkest shade marks the lowest elevation while the lightest shade marks the highest elevation.

Table 8: Mann-Kendall test with monthly mean albedo values in at least three years per elevation band to detect interannual trends.

Elevation band	June	July	August	September	October
2466.86	no test	no test	no trend	no test	no test
2566.86	no test	no test	no test	no test	no test
2666.86	no test	no test	no test	no test	no test
2766.86	no test	no test	no trend	no trend	no test

Table 9: Kruskal-Wallis test per elevation band and year to detect significant sub-seasonal albedo differences between June and October.

Elevation band	2013	2014	2015	2016	2017	2018	2019	2020	2021	2022	2023	2024
2466.86	no	no	no	no	no	no	yes	no	no	yes	no	no
2566.86	no											
2666.86	no											
2766.86	no	yes	no	no								

B.2.2 Kanderfirn

Kanderfirn (CH)
23.08.2024
Sentinel 2 accessed with GEE

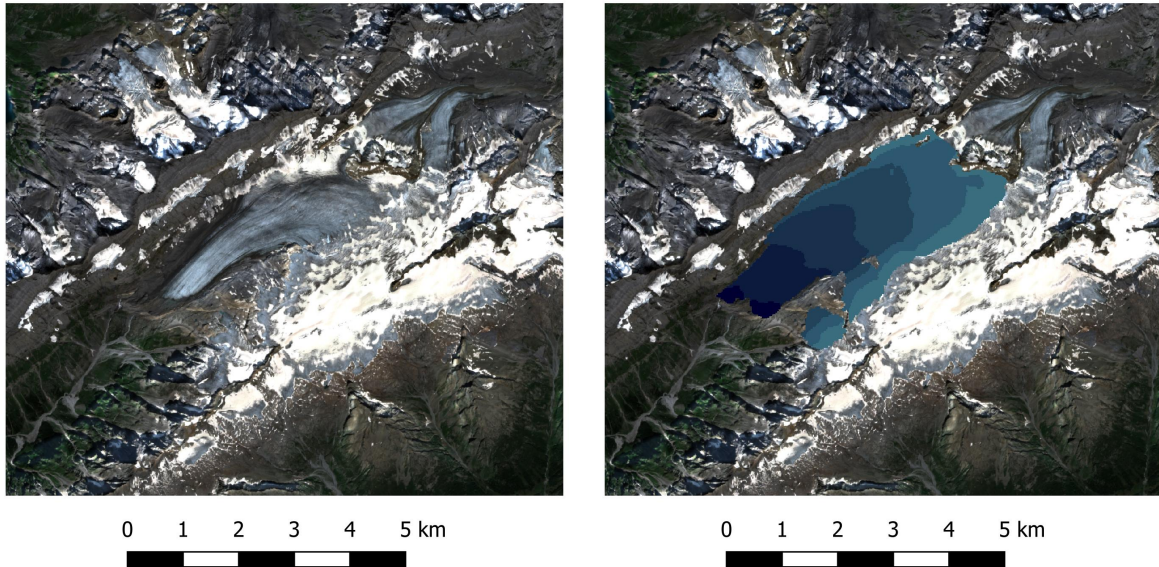


Figure 2: Satellite image of Kanderfirn (left image) and the elevation bands used for the trend analysis in different shades of blue (right image). The darkest shade marks the lowest elevation while the lightest shade marks the highest elevation.

Table 10: Mann-Kendall test with monthly mean albedo values in at least three years per elevation band to detect interannual trends.

Elevation band	June	July	August	September	October
2292.94	no trend	no trend	no trend	no trend	no trend
2392.94	no test	no trend	no trend	no trend	no trend
2492.94	no test	no trend	no trend	no trend	no trend
2592.94	no test	no trend	no trend	no trend	no test
2692.94	no test	no test	no trend	no trend	no test
2792.94	no test	no test	no trend	no trend	no test

Table 11: Kruskal-Wallis test per elevation band and year to detect significant sub-seasonal albedo differences between June and October.

Elevation band	2013	2014	2015	2016	2017	2018	2019	2020	2021	2022	2023	2024
2292.94	no	no	no	no	no	yes	yes	no	no	no	no	no
2392.94	no	no	no	no	no	yes	no	no	no	yes	no	no
2492.94	no	no	no	no	no	yes	no	no	no	yes	no	no
2592.94	no											
2692.94	no											
2792.94	no											

B.2.3 Unteraargletscher

Unteraargletscher (CH)
23.08.2024
Sentinel 2 accessed with GEE

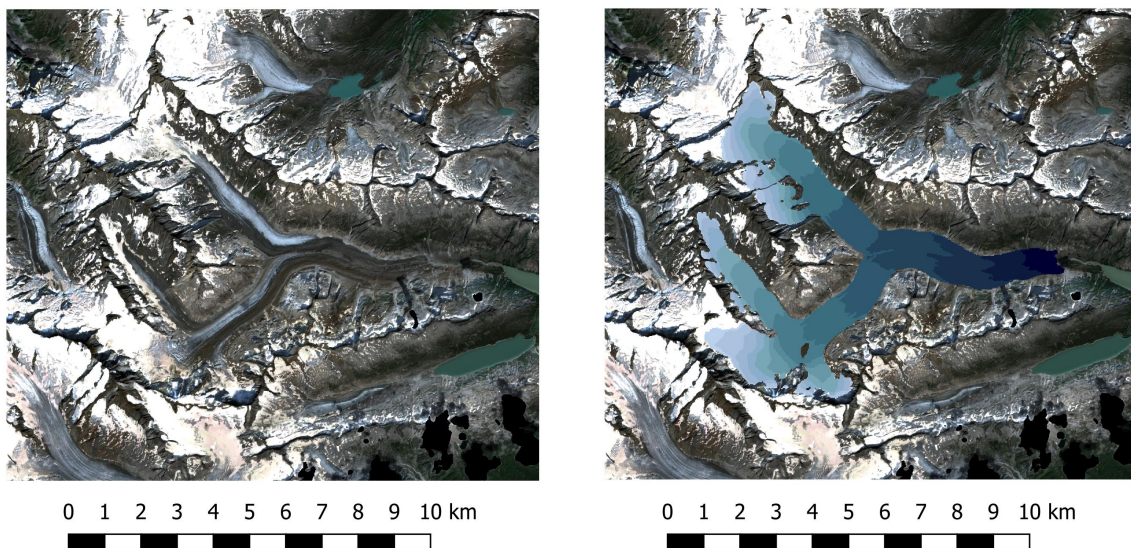


Figure 3: Satellite image of Unteraargletscher (left image) and the elevation bands used for the trend analysis in different shades of blue (right image). The darkest shade marks the lowest elevation while the lightest shade marks the highest elevation.

Table 12: Mann-Kendall test with monthly mean albedo values in at least three years per elevation band to detect interannual trends.

Elevation band	June	July	August	September	October
1930.99	no test	no test	no test	no test	no test
2030.99	no test	no test	no test	no test	no test
2130.99	no test	no test	no test	no test	no test
2230.99	no trend	no trend	no trend	no trend	no trend
2330.99	no trend	no trend	no trend	no trend	no trend
2430.99	no test	no trend	no trend	no trend	no test
2530.99	no test	no trend	no trend	no trend	no test
2630.99	no test	no test	no trend	no trend	no test
2730.99	no test	no test	no trend	no trend	no test
2830.99	no test	no test	no test	no trend	no test
2930.99	no test	no test	no test	no test	no test
3030.99	no test	no test	no test	no test	no test
3130.99	no test	no test	no test	no test	no test
3230.99	no test	no test	no test	no test	no test

Table 13: Kruskal-Wallis test per elevation band and year to detect significant sub-seasonal albedo differences between June and October.

Elevation band	2013	2014	2015	2016	2017	2018	2019	2020	2021	2022	2023	2024
1930.99	no											
2030.99	no	no	no	no	no	no	yes	no	no	no	no	no
2130.99	no											
2230.99	no	no	no	no	no	yes	no	no	yes	yes	no	no
2330.99	no	no	no	no	no	yes	no	no	yes	yes	yes	yes
2430.99	no	no	no	no	no	yes	no	no	yes	yes	no	no
2530.99	no	yes	yes	yes	no							
2630.99	no	no	no	no	no	yes	no	no	no	yes	no	no
2730.99	no											
2830.99	no											
2930.99	no	yes	no									
3030.99	no											
3130.99	no											
3230.99	no											

B.2.4 Hüfifirn

Hüfifirn (CH)
06.08.2024
Sentinel 2 accessed with GEE

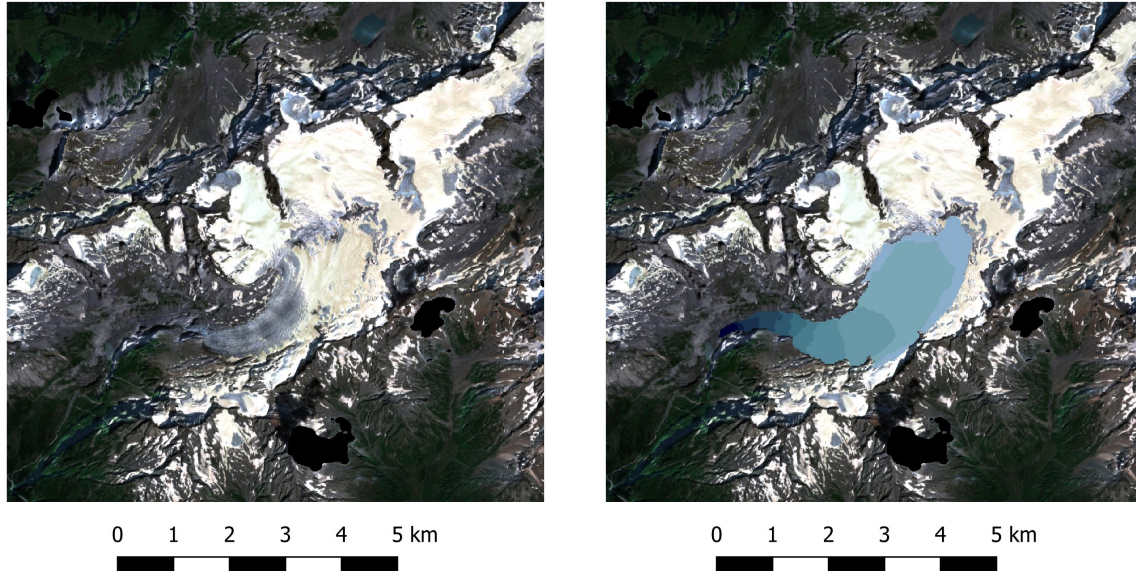


Figure 4: Satellite image of Glacier de la Plaine Morte (left image) and the elevation bands used for the trend analysis in different shades of blue (right image). The darkest shade marks the lowest elevation while the lightest shade marks the highest elevation.

Table 14: Mann-Kendall test with monthly mean albedo values in at least three years per elevation band to detect interannual trends.

Elevation band	June	July	August	September	October
1637.16	no test	no test	no test	no test	no test
1737.16	no test	no test	no test	no test	no test
1837.16	no trend	no test	no test	no test	no test
1937.16	no trend	no trend	no trend	no trend	no test
2037.16	no trend	no trend	no trend	no trend	no test
2137.16	no test	no trend	no trend	no trend	no trend
2237.16	no test	no trend	no trend	no trend	no trend
2337.16	no test	no trend	no trend	no trend	no trend
2437.16	no test	no trend	no trend	no trend	no test
2537.16	no test	no test	decreasing (-1.000)	no trend	no test
2637.16	no test	no test	no trend	no trend	no test

Table 15: Kruskal-Wallis test per elevation band and year to detect significant sub-seasonal albedo differences between June and October.

Elevation band	2013	2014	2015	2016	2017	2018	2019	2020	2021	2022	2023	2024
1637.16	no											
1737.16	no											
1837.16	no											
1937.16	no	no	no	no	no	yes	no	no	yes	no	no	no
2037.16	no	no	no	no	no	yes	no	yes	no	yes	no	no
2137.16	no	no	no	no	no	yes	no	no	no	no	yes	no
2237.16	no	yes	no									
2337.16	no	no	no	no	no	no	yes	no	no	yes	yes	no
2437.16	no	yes	no	no	yes	no						
2537.16	no											
2637.16	no	yes	no									

B.2.5 Ochsentaler Gletscher

Ochsentaler Gletscher (AT)
 23.08.2024
 Sentinel 2 accessed with GEE

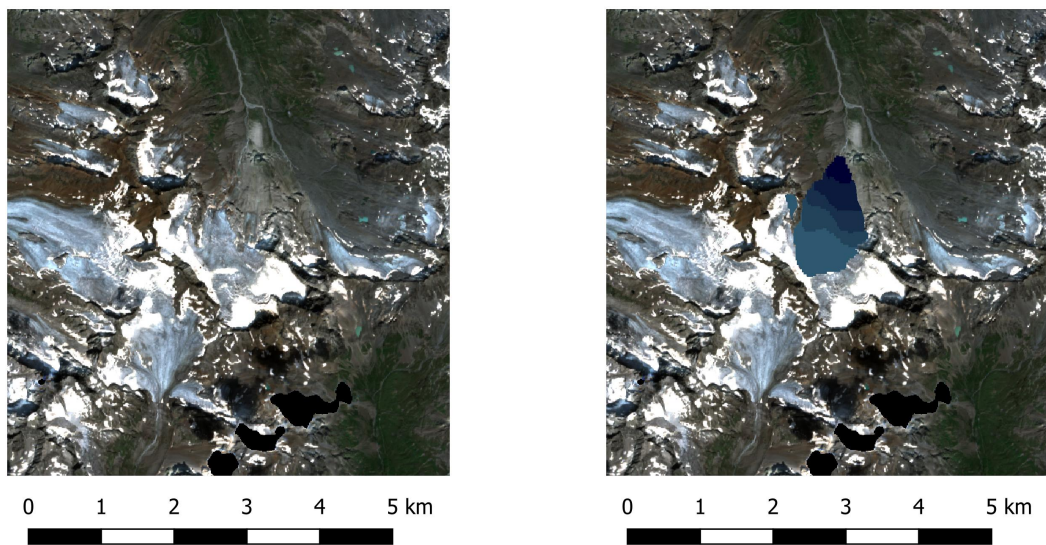


Figure 5: Satellite image of Ochsentaler Gletscher (left image) and the elevation bands used for the trend analysis in different shades of blue (right image). The darkest shade marks the lowest elevation while the lightest shade marks the highest elevation.

Table 16: Mann-Kendall test with monthly mean albedo values in at least three years per elevation band to detect interannual trends.

Elevation band	June	July	August	September	October
2395.70	no test	no test	no test	no test	no test
2495.70	no test	no test	no test	no trend	no test
2595.70	no test	no test	no test	no test	no test
2695.70	no test	no test	no trend	no trend	no test
2795.70	no test	no test	no trend	no test	no test

Table 17: Kruskal-Wallis test per elevation band and year to detect significant sub-seasonal albedo differences between June and October.

Elevation band	2013	2014	2015	2016	2017	2018	2019	2020	2021	2022	2023	2024
2395.70	no											
2495.70	no											
2595.70	no											
2695.70	no											
2795.70	no											

B.2.6 Rhonegletscher

Rhonegletscher (CH)
06.08.2024
Sentinel 2 accessed with GEE

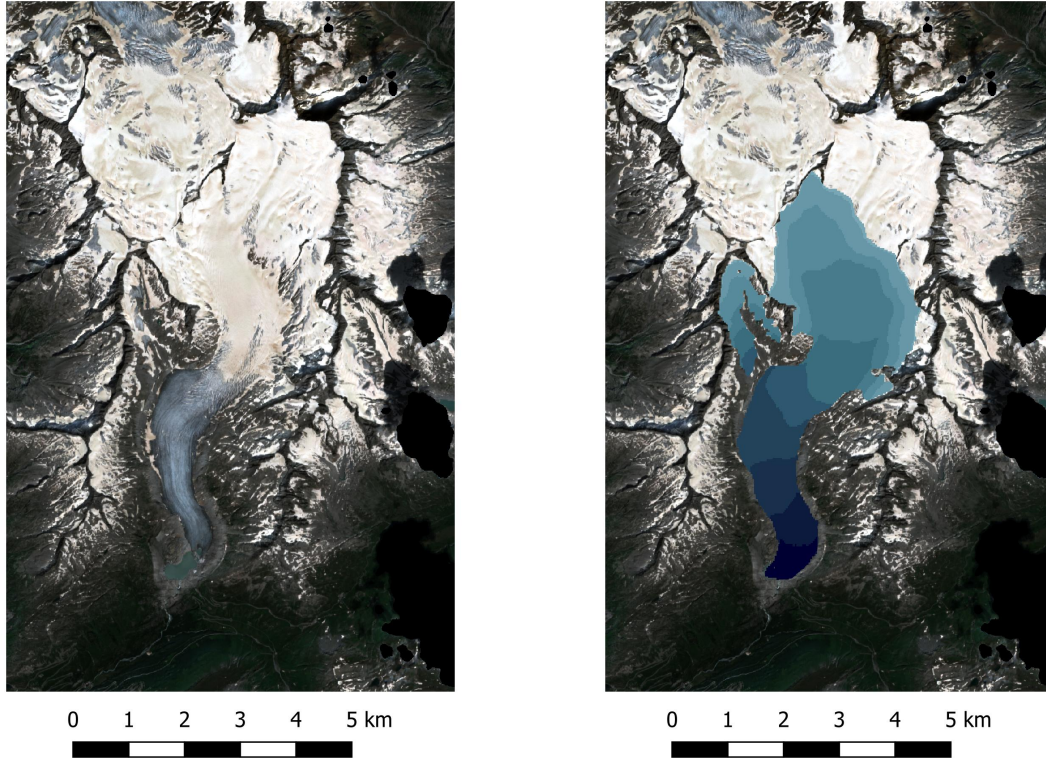


Figure 6: Satellite image of Rhonegletscher (left image) and the elevation bands used for the trend analysis in different shades of blue (right image). The darkest shade marks the lowest elevation while the lightest shade marks the highest elevation.

Table 18: Mann-Kendall test with monthly mean albedo values in at least three years per elevation band to detect interannual trends.

Elevation band	June	July	August	September	October
2207.01	no test	no test	no test	no test	no test
2307.01	no test	no trend	no trend	no test	no trend
2407.01	no test	no trend	no trend	no test	no test
2507.01	no test	no trend	no trend	no test	no test
2607.01	no test	no trend	no trend	no test	no test
2707.01	no test	no test	no trend	no test	no test
2807.01	no test	no test	no trend	no test	no test
2907.01	no test	no test	no test	no test	no test
3007.01	no test	no test	no test	no test	no test
3107.01	no test	no test	no test	no test	no test

Table 19: Kruskal-Wallis test per elevation band and year to detect significant sub-seasonal albedo differences between June and October.

Elevation band	2013	2014	2015	2016	2017	2018	2019	2020	2021	2022	2023	2024
2207.01	no											
2307.01	no	no	no	no	no	no	yes	no	no	yes	yes	no
2407.01	no	yes	no	no								
2507.01	no	yes	no	no								
2607.01	no	yes	yes	no								
2707.01	no											
2807.01	no											
2907.01	no											
3007.01	no											
3107.01	no											

B.2.7 Grosser Aletschgletscher

Grosser Aletschgletscher (CH)

15.09.2024

Sentinel 2 accessed with GEE

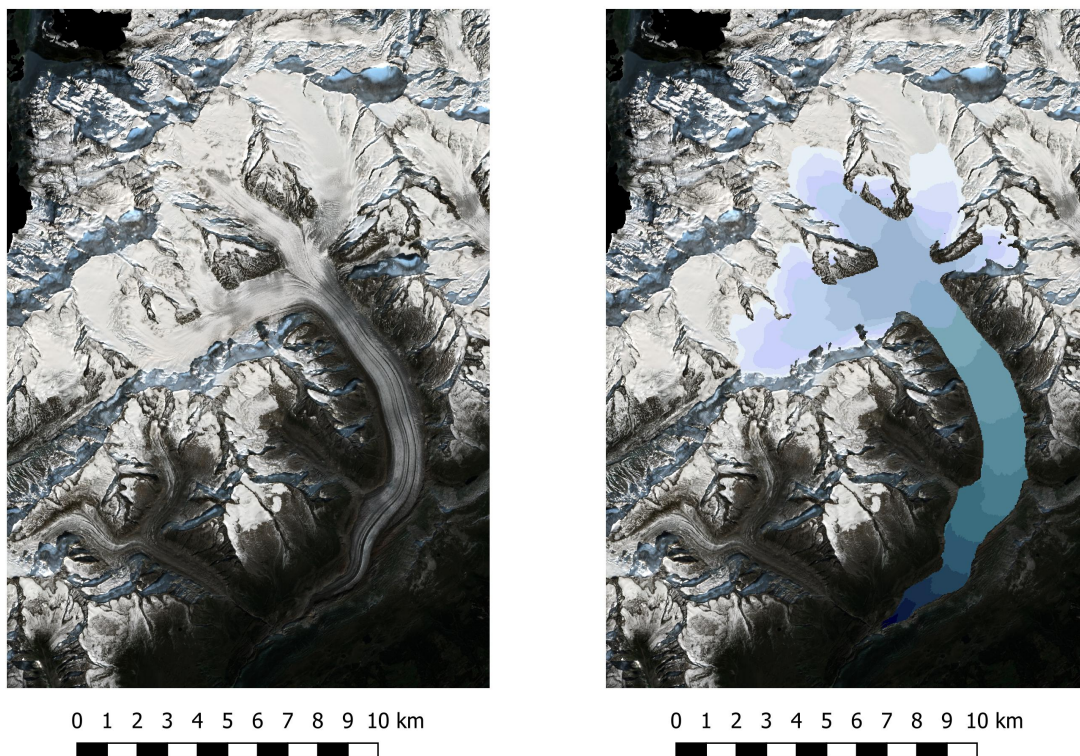


Figure 7: Satellite image of Grosser Aletschgletscher (left image) and the elevation bands used for the trend analysis in different shades of blue (right image). The darkest shade marks the lowest elevation while the lightest shade marks the highest elevation.

Table 20: Mann-Kendall test with monthly mean albedo values in at least three years per elevation band to detect interannual trends.

Elevation band	June	July	August	September	October
1578.35	no test	no test	no test	no test	no test
1678.35	no test	no test	no test	no test	no test
1778.35	no test	no trend	no trend	no trend	no trend
1878.35	no trend	no trend	no trend	no trend	no trend
1978.35	no trend	no trend	no trend	no trend	no trend
2078.35	no trend	no trend	no trend	no trend	no trend
2178.35	no trend	no trend	no trend	no trend	no trend
2278.35	no trend	no trend	no trend	no trend	no trend
2378.35	no trend	no trend	no trend	increasing (0.714)	no trend
2478.35	no trend	no trend	no trend	no trend	no trend
2578.35	no test	no trend	no trend	no trend	no trend
2678.35	no test	no trend	no trend	no trend	no test
2778.35	no test	no trend	no trend	no trend	no test
2878.35	no test	no test	no trend	no trend	no test
2978.35	no test	no test	no test	no trend	no test
3078.35	no test	no test	no test	no test	no test
3178.35	no test	no test	no test	no test	no test

Table 21: Kruskal-Wallis test per elevation band and year to detect significant sub-seasonal albedo differences between June and October.

Elevation band	2013	2014	2015	2016	2017	2018	2019	2020	2021	2022	2023	2024
1578.35	no											
1678.35	no											
1778.35	no	no	no	no	no	yes	no	no	no	no	no	no
1878.35	no											
1978.35	no	yes										
2078.35	no	yes	no	yes								
2178.35	no	no	no	no	no	yes	yes	no	yes	yes	no	yes
2278.35	no	no	no	no	yes	yes	no	no	yes	yes	no	yes
2378.35	no	no	no	no	yes	yes	yes	yes	yes	yes	no	no
2478.35	no	no	no	no	no	yes	no	no	yes	no	no	yes
2578.35	no	no	no	no	yes							
2678.35	no	no	no	no	no	yes	no	no	no	yes	yes	no
2778.35	no	no	no	no	no	yes	no	yes	no	yes	yes	no
2878.35	no	yes	no									
2978.35	no											
3078.35	no	yes	no									
3178.35	no											

B.2.8 Gornergletscher

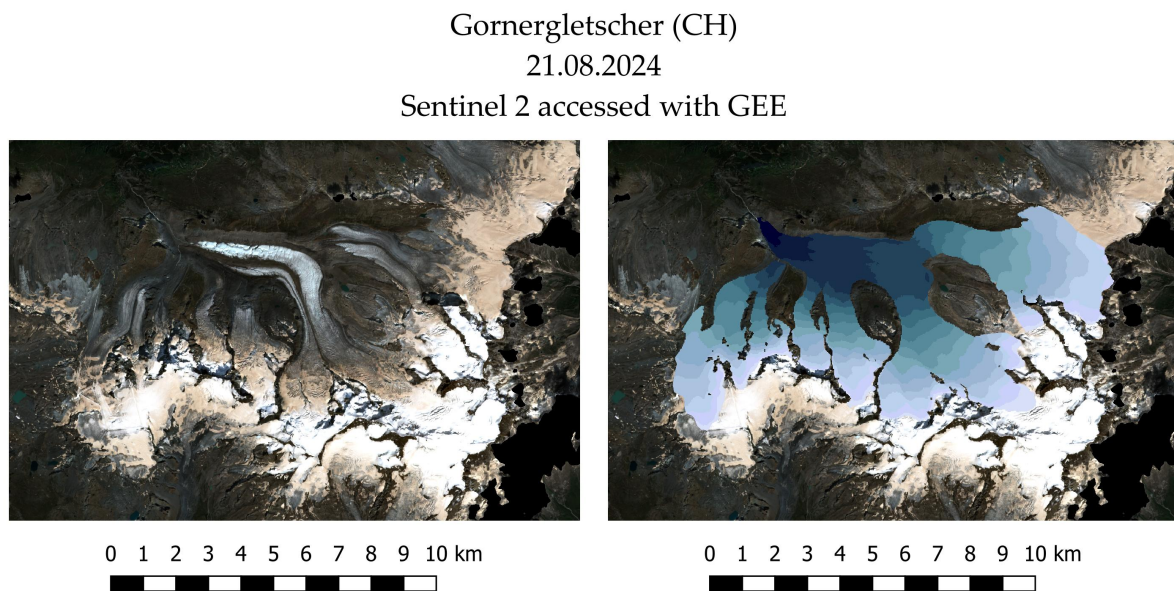


Figure 8: Satellite image of Glacier de la Plaine Morte (left image) and the elevation bands used for the trend analysis in different shades of blue (right image). The darkest shade marks the lowest elevation while the lightest shade marks the highest elevation.

Table 22: Mann-Kendall test with monthly mean albedo values in at least three years per elevation band to detect interannual trends.

Elevation band	June	July	August	September	October
2181.58	no trend	no trend	no trend	no test	no test
2281.58	no trend	no trend	no trend	no trend	no trend
2381.58	no trend	no trend	no trend	no trend	no trend
2481.58	no trend	no trend	no trend	increasing (0.714)	no trend
2581.58	no trend	no trend	no trend	increasing (0.857)	no trend
2681.58	no trend	no trend	no trend	increasing (0.714)	no trend
2781.58	no trend	no trend	no trend	no trend	no trend
2881.58	no test	no trend	no trend	no trend	no test
2981.58	no test	no trend	decreasing (-0.786)	no trend	no test
3081.58	no test	no test	no trend	no trend	no test
3181.58	no test	no test	no trend	no trend	no test
3281.58	no test	no test	no trend	no test	no test
3381.58	no test	no test	no test	no test	no test
3481.58	no test	no test	no test	no test	no test
3581.58	no test	no test	no test	no test	no test
3681.58	no test	no test	no test	no test	no test

Table 23: Kruskal-Wallis test per elevation band and year to detect significant sub-seasonal albedo differences between June and October.

Elevation band	2013	2014	2015	2016	2017	2018	2019	2020	2021	2022	2023	2024
2181.58	no											
2281.58	no	no	no	no	no	yes	no	no	no	no	no	no
2381.58	no	no	no	no	yes	yes	no	no	no	no	no	no
2481.58	no	no	no	no	yes	no	no	no	no	yes	no	no
2581.58	no	no	no	no	no	yes	no	yes	yes	yes	yes	no
2681.58	no	no	no	no	no	yes	no	no	no	yes	no	yes
2781.58	no	no	no	no	yes	yes	no	no	no	yes	yes	yes
2881.58	no	no	no	no	no	yes	no	yes	no	yes	yes	yes
2981.58	no	yes	no	yes	yes	yes						
3081.58	no	yes	no									
3181.58	no	yes	yes	no								
3281.58	no	yes	yes	no								
3381.58	no											
3481.58	no											
3581.58	no											
3681.58	no											

B.2.9 Mer de Glace

Mer de Glace (FR)
21.08.2024
Sentinel 2 accessed with GEE

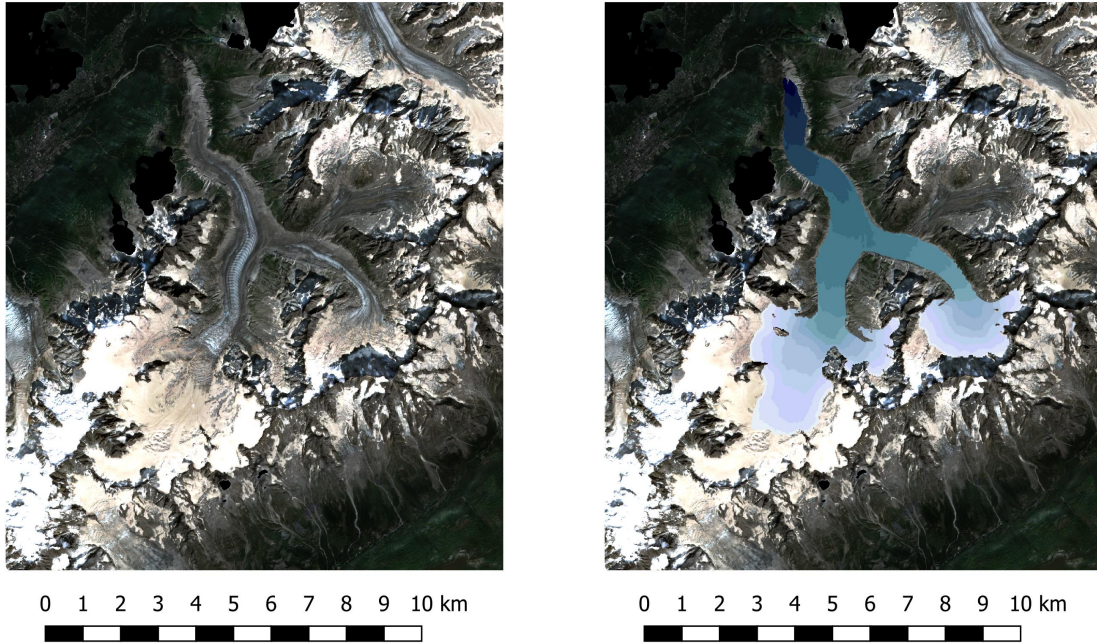


Figure 9: Satellite image of Mer de Glace (left image) and the elevation bands used for the trend analysis in different shades of blue (right image). The darkest shade marks the lowest elevation while the lightest shade marks the highest elevation.

Table 24: Mann-Kendall test with monthly mean albedo values in at least three years per elevation band to detect interannual trends.

Elevation band	June	July	August	September	October
1486.59	no test	no test	no test	no test	no test
1586.59	no test	no test	no test	no test	no test
1686.59	no test	no test	no test	no test	no test
1786.59	decreasing (-1.000)	no trend	no trend	no trend	no test
1886.59	no trend	no trend	no trend	no trend	no trend
1986.59	no trend	no trend	no trend	no trend	no trend
2086.59	no test	no trend	no trend	no trend	no trend
2186.59	no trend	no trend	no trend	increasing (0.714)	no trend
2286.59	no test	no trend	no trend	no trend	no test
2386.59	no test	no trend	no trend	no trend	no test
2486.59	no test	no trend	no trend	no trend	no test
2586.59	no test	no test	no trend	no trend	no test
2686.59	no test	no test	no trend	no trend	no test
2786.59	no test	no test	no trend	no trend	no test
2886.59	no test	no test	no test	no test	no test
2986.59	no test	no test	no test	no test	no test
3086.59	no test	no test	no test	no test	no test

Table 25: Kruskal-Wallis test per elevation band and year to detect significant sub-seasonal albedo differences between June and October.

Elevation band	2013	2014	2015	2016	2017	2018	2019	2020	2021	2022	2023	2024
1486.59	no											
1586.59	no											
1686.59	no											
1786.59	no											
1886.59	no	yes	yes									
1986.59	no	yes										
2086.59	no	yes	no	no								
2186.59	no	no	no	no	no	yes	no	no	no	yes	no	yes
2286.59	no	yes	no	yes								
2386.59	no											
2486.59	no											
2586.59	no	yes	no	no								
2686.59	no	yes	no	no								
2786.59	no	yes	no	no								
2886.59	no											
2986.59	no											
3086.59	no											

B.2.10 Glacier Blanc

Glacier Blanc (FR)
10.09.2024
Sentinel 2 accessed with GEE

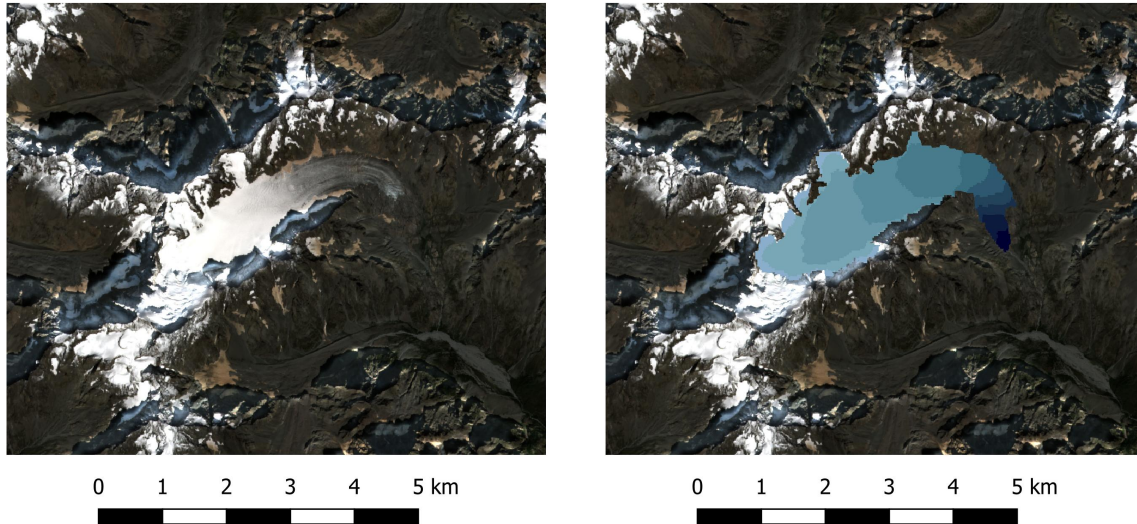


Figure 10: Satellite image of Glacier Blanc (left image) and the elevation bands used for the trend analysis in different shades of blue (right image). The darkest shade marks the lowest elevation while the lightest shade marks the highest elevation.

Table 26: Mann-Kendall test with monthly mean albedo values in at least three years per elevation band to detect interannual trends.

Elevation band	June	July	August	September	October
2345.61	no test	no test	no test	no test	no test
2445.61	no test	no test	no test	no test	no test
2545.61	no test	no trend	no test	no test	no test
2645.61	no trend	no trend	increasing (0.667)	no trend	no trend
2745.61	no test	no trend	no trend	no trend	no trend
2845.61	no test	no trend	no trend	no trend	no test
2945.61	no test	no trend	no trend	no trend	no test
3045.61	no test	no test	no trend	no trend	no test
3145.61	no test	no test	no test	no test	no test
3245.61	no test	no test	no test	no test	no test
3345.61	no test	no test	no test	no test	no test

Table 27: Kruskal-Wallis test per elevation band and year to detect significant sub-seasonal albedo differences between June and October.

Elevation band	2013	2014	2015	2016	2017	2018	2019	2020	2021	2022	2023	2024
2345.61	no											
2445.61	no											
2545.61	no											
2645.61	no	no	no	no	no	yes	yes	no	yes	yes	no	no
2745.61	no	yes	yes	yes								
2845.61	no	yes	yes	no								
2945.61	no	no	no	no	yes	no	no	no	no	yes	yes	yes
3045.61	no	no	no	no	yes	no	no	no	no	yes	no	yes
3145.61	no											
3245.61	no											
3345.61	no											

B.2.11 Ghiacciaio del Rutor

Ghiacciaio del Rutor (IT)
 21.08.2024
 Sentinel 2 accessed with GEE

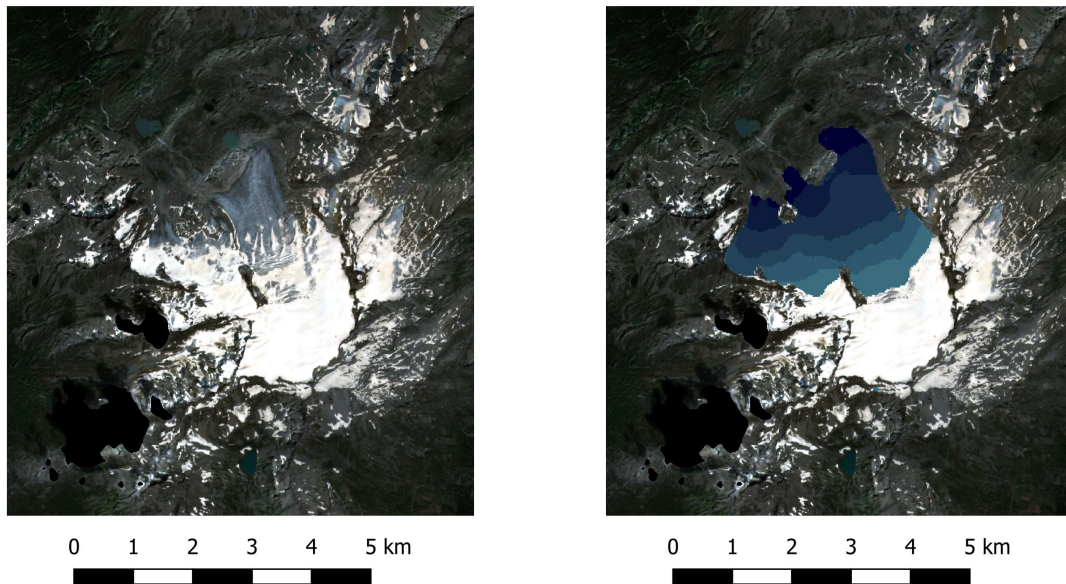


Figure 11: Satellite image of Ghiacciaio del Rutor (left image) and the elevation bands used for the trend analysis in different shades of blue (right image). The darkest shade marks the lowest elevation while the lightest shade marks the highest elevation.

Table 28: Mann-Kendall test with monthly mean albedo values in at least three years per elevation band to detect interannual trends.

Elevation band	June	July	August	September	October
2538.32	no test	no test	no test	no test	no test
2638.32	no test	no trend	no trend	no trend	no test
2738.32	no test	no test	no trend	no trend	no test
2838.32	no test	no test	no test	no trend	no test
2938.32	no test	no test	no test	no test	no test
3038.32	no test	no test	no test	no test	no test

Table 29: Kruskal-Wallis test per elevation band and year to detect significant sub-seasonal albedo differences between June and October.

Elevation band	2013	2014	2015	2016	2017	2018	2019	2020	2021	2022	2023	2024
2538.32	no											
2638.32	no											
2738.32	no											
2838.32	no											
2938.32	no											
3038.32	no											

B.2.12 Vadrec del Forno

Vadrec del Forno (CH)
 19.08.2023
 Sentinel 2 accessed with GEE

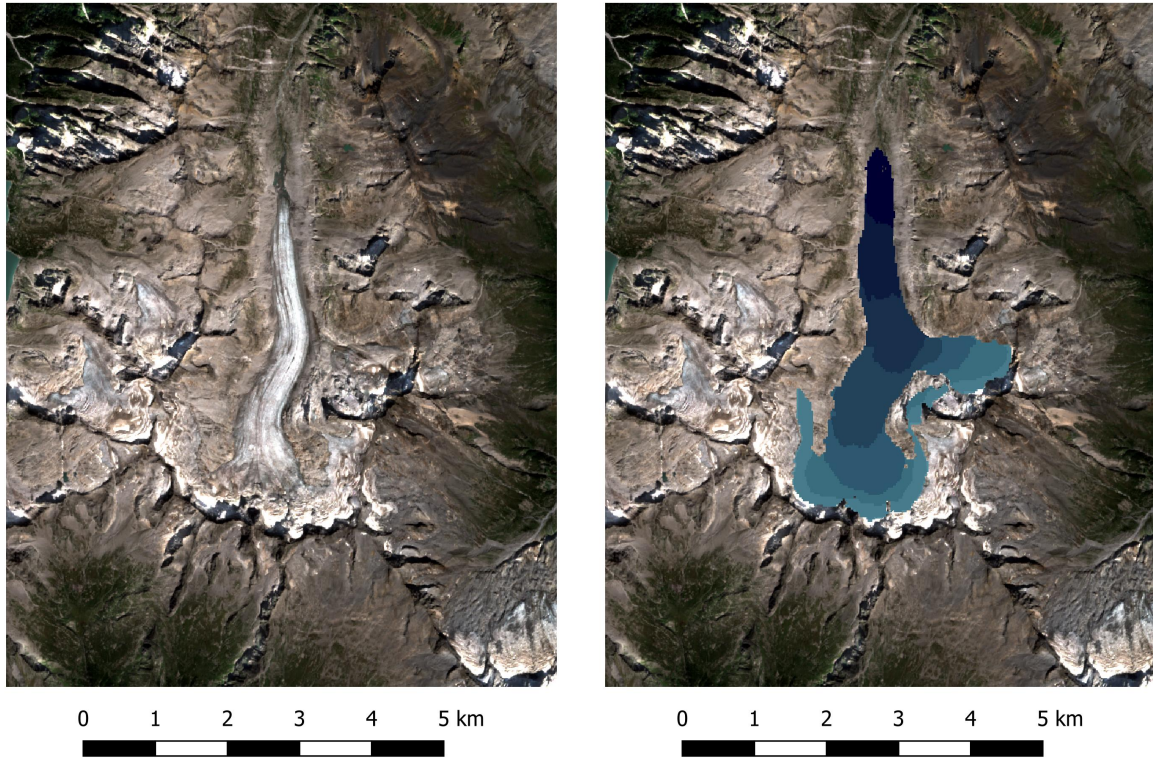


Figure 12: Satellite image of Vadrec del Forno (left image) and the elevation bands used for the trend analysis in different shades of blue (right image). The darkest shade marks the lowest elevation while the lightest shade marks the highest elevation.

Table 30: Mann-Kendall test with monthly mean albedo values in at least three years per elevation band to detect interannual trends.

Elevation band	June	July	August	September	October
2227.37	no test	no trend	no trend	no trend	no trend
2327.37	no trend	no trend	no trend	no trend	no trend
2427.37	no trend	no trend	no trend	no trend	no trend
2527.37	no test	no trend	no trend	no trend	no test
2627.37	no test	no trend	no trend	no trend	no test
2727.37	no test	no test	no test	no test	no test
2827.37	no test	no test	no test	no test	no test
2927.37	no test	no test	no test	no test	no test

Table 31: Kruskal-Wallis test per elevation band and year to detect significant sub-seasonal albedo differences between June and October.

Elevation band	2013	2014	2015	2016	2017	2018	2019	2020	2021	2022	2023	2024
2227.37	no	yes	no	yes	no							
2327.37	no	yes	yes									
2427.37	no	yes	no	no	yes	no						
2527.37	no	yes	no									
2627.37	no	no	no	no	no	yes	no	no	no	yes	yes	no
2727.37	no											
2827.37	no											
2927.37	no											

B.2.13 Ghiacciaio dei Forni

Ghiacciaio dei Forni (IT)

31.07.2024

Sentinel 2 accessed with GEE

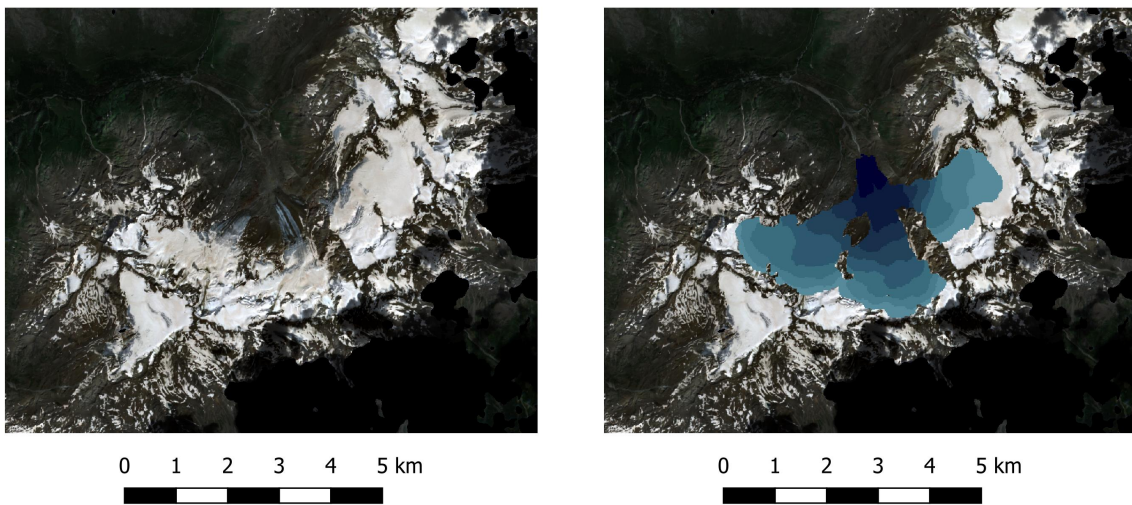


Figure 13: Satellite image of Ghiacciaio dei Forni (left image) and the elevation bands used for the trend analysis in different shades of blue (right image). The darkest shade marks the lowest elevation while the lightest shade marks the highest elevation.

Table 32: Mann-Kendall test with monthly mean albedo values in at least three years per elevation band to detect interannual trends.

Elevation band	June	July	August	September	October
2492.90	no test	no test	no test	no test	no trend
2592.90	no test	no trend	no trend	no trend	no trend
2692.90	no test	no trend	decreasing (-0.810)	no trend	no test
2792.90	no test	no trend	no trend	no trend	no test
2892.90	no test	no test	no trend	no trend	no test
2992.90	no test	no test	no test	no trend	no test
3092.90	no test	no test	no test	no test	no test
3192.90	no test	no test	no test	no test	no test

Table 33: Kruskal-Wallis test per elevation band and year to detect significant sub-seasonal albedo differences between June and October.

Elevation band	2013	2014	2015	2016	2017	2018	2019	2020	2021	2022	2023	2024
2492.90	no											
2592.90	no	no	no	no	no	yes	no	no	no	no	no	no
2692.90	no	yes	no	no								
2792.90	no	yes	no	no								
2892.90	no											
2992.90	no											
3092.90	no											
3192.90	no											

B.2.14 Ghiacciaio dell'Adamello

Ghiacciaio dell'Adamello (IT)

31.07.2024

Sentinel 2 accessed with GEE

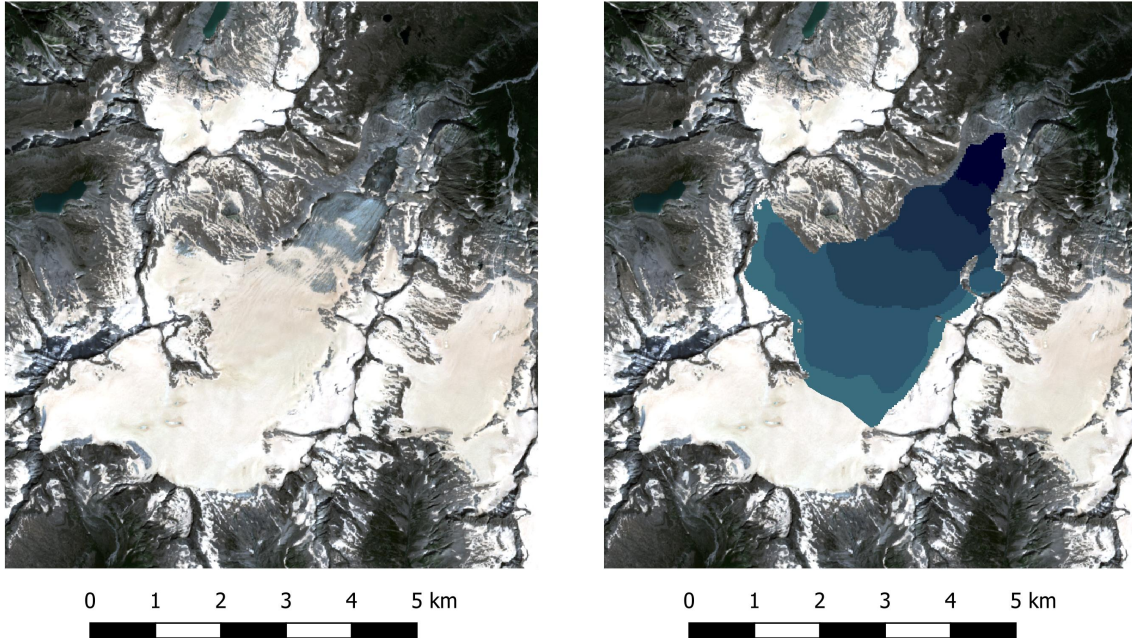


Figure 14: Satellite image of Ghiacciaio dell'Adamello (left image) and the elevation bands used for the trend analysis in different shades of blue (right image). The darkest shade marks the lowest elevation while the lightest shade marks the highest elevation.

Table 34: Mann-Kendall test with monthly mean albedo values in at least three years per elevation band to detect interannual trends.

Elevation band	June	July	August	September	October
2540.38	no test	no trend	no trend	no trend	no trend
2640.38	no test	no trend	no trend	no trend	no test
2740.38	no test	no trend	no trend	no trend	no test
2840.38	no test	no trend	no trend	no trend	no test
2940.38	no test	no trend	no trend	no trend	no test
3040.38	no test	no test	no trend	no test	no test

Table 35: Kruskal-Wallis test per elevation band and year to detect significant sub-seasonal albedo differences between June and October.

Elevation band	2013	2014	2015	2016	2017	2018	2019	2020	2021	2022	2023	2024
2540.38	no	no	no	no	no	yes	no	yes	no	yes	yes	no
2640.38	no	yes	no	yes	yes	no						
2740.38	no	yes	no	yes	yes	no						
2840.38	no	yes	no	yes	yes	no						
2940.38	no	yes	no	no	yes	no						
3040.38	no											

B.2.15 Vadret da Morteratsch

Vadret da Morteratsch (CH)

29.07.2024

Sentinel 2 accessed with GEE

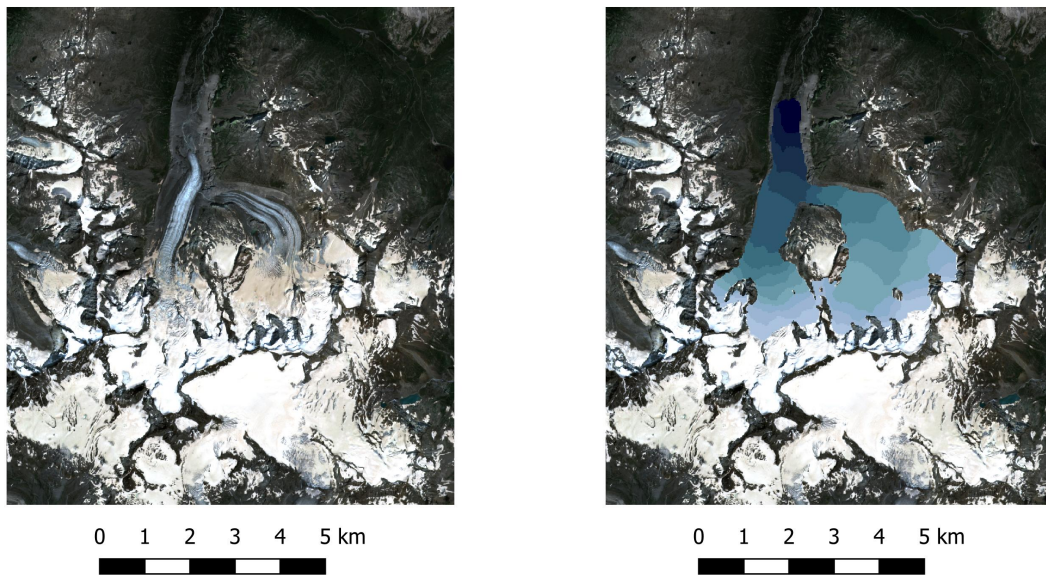


Figure 15: Satellite image of Vadret da Morteratsch (left image) and the elevation bands used for the trend analysis in different shades of blue (right image). The darkest shade marks the lowest elevation while the lightest shade marks the highest elevation.

Table 36: Mann-Kendall test with monthly mean albedo values in at least three years per elevation band to detect interannual trends.

Elevation band	June	July	August	September	October
2004.46	no test	no test	no test	no test	no test
2104.46	no test	no trend	no test	no trend	no test
2204.46	no trend	no trend	no trend	no trend	no trend
2304.46	no trend	no trend	no trend	no trend	no trend
2404.46	no trend	no trend	no trend	no trend	no trend
2504.46	no trend	no trend	no trend	no trend	no test
2604.46	no trend	no trend	no trend	no trend	no test
2704.46	no test	no trend	no trend	increasing (0.867)	no test
2804.46	no test	no trend	no trend	no trend	no test
2904.46	no test	no trend	no trend	no trend	no test
3004.46	no test	no test	no trend	no test	no test
3104.46	no test	no test	no trend	no test	no test
3204.46	no test	no test	no test	no test	no test
3304.46	no test	no test	no test	no test	no test

Table 37: Kruskal-Wallis test per elevation band and year to detect significant sub-seasonal albedo differences between June and October.

Elevation band	2013	2014	2015	2016	2017	2018	2019	2020	2021	2022	2023	2024
2004.46	no											
2104.46	no	no	no	no	no	no	yes	no	no	no	no	no
2204.46	no											
2304.46	no	yes	no									
2404.46	no	yes	no	yes	yes	no						
2504.46	no	yes	yes	no								
2604.46	no	yes	yes	no								
2704.46	no	yes	yes	no								
2804.46	no	yes	yes	no								
2904.46	no	yes	no									
3004.46	no											
3104.46	no											
3204.46	no											
3304.46	no											

B.2.16 Gepatschferner

Gepatschferner (AT)
10.08.2024
Sentinel 2 accessed with GEE

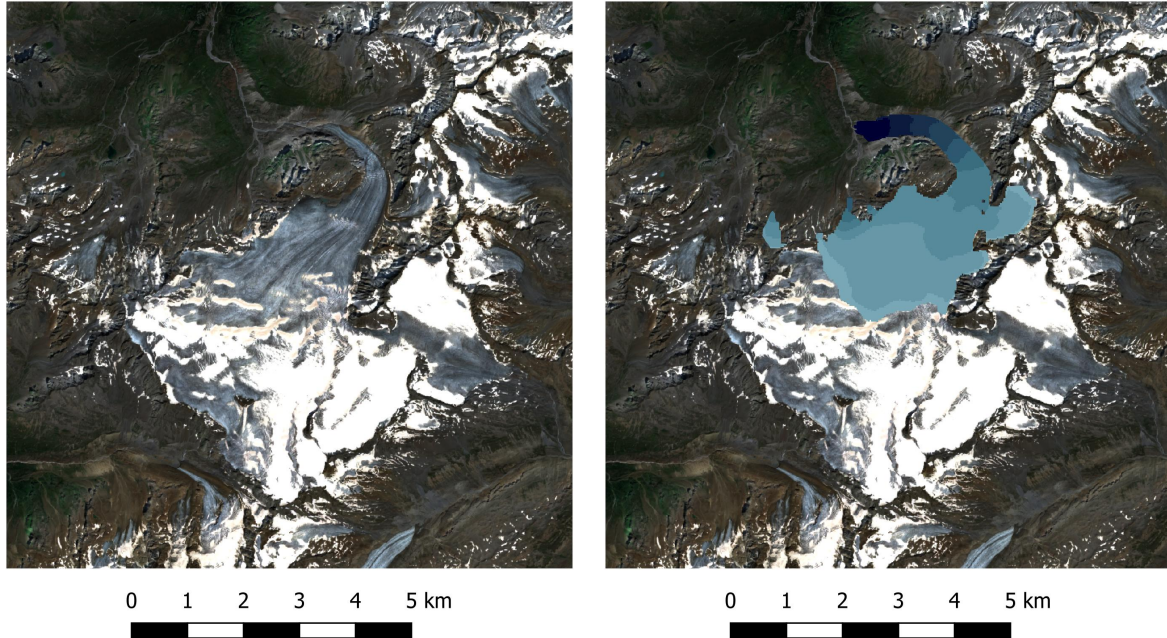


Figure 16: Satellite image of Gepatschferner (left image) and the elevation bands used for the trend analysis in different shades of blue (right image). The darkest shade marks the lowest elevation while the lightest shade marks the highest elevation.

Table 38: Mann-Kendall test with monthly mean albedo values in at least three years per elevation band to detect interannual trends.

Elevation band	June	July	August	September	October
2113.05	no test	no test	no test	no test	no test
2213.05	no trend	no trend	no trend	no trend	no test
2313.05	no trend	no trend	no trend	no trend	no test
2413.05	no trend	no trend	no trend	no trend	no trend
2513.05	no test	no trend	no trend	no trend	no test
2613.05	no trend	no trend	no trend	no trend	no test
2713.05	no test	no trend	no trend	no trend	no test
2813.05	no test	no trend	no trend	no trend	no test
2913.05	no test	no test	no trend	no trend	no test
3013.05	no test	no test	no trend	no trend	no test

Table 39: Kruskal-Wallis test per elevation band and year to detect significant sub-seasonal albedo differences between June and October.

Elevation band	2013	2014	2015	2016	2017	2018	2019	2020	2021	2022	2023	2024
2113.05	no											
2213.05	no	no	no	no	no	no	yes	no	no	no	no	no
2313.05	no	yes	no									
2413.05	no	no	no	no	no	yes	no	no	yes	no	no	yes
2513.05	no	no	no	no	no	yes	no	no	yes	no	yes	yes
2613.05	no	no	no	no	no	yes	no	no	yes	no	no	yes
2713.05	no	yes	yes	no	no							
2813.05	no	yes	no	no	yes	no						
2913.05	no	no	no	no	no	yes	no	no	no	no	yes	no
3013.05	no											

B.2.17 Hintereisferner

Hintereisferner (AT)
10.08.2024
Sentinel 2 accessed with GEE

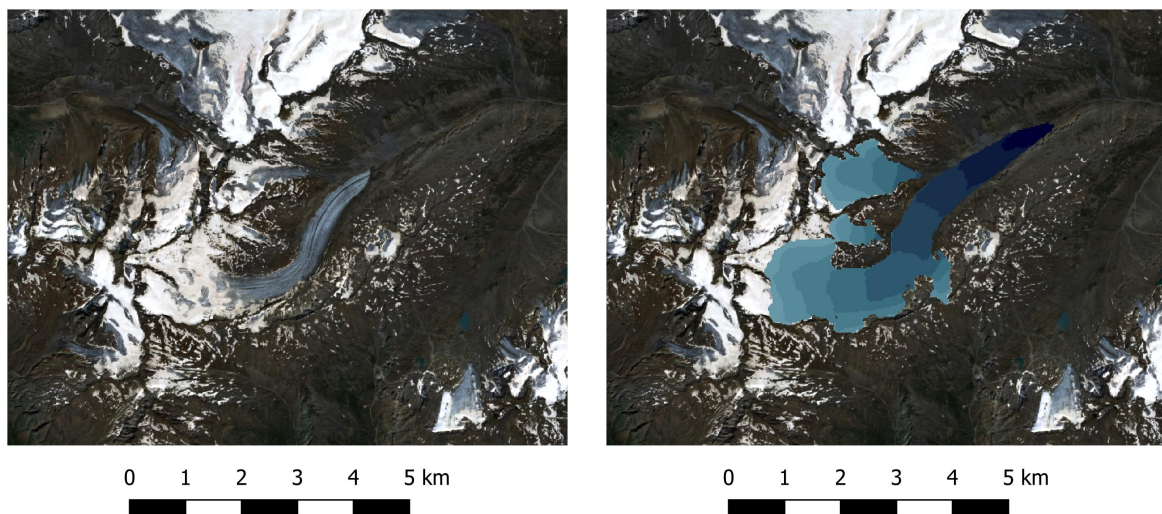


Figure 17: Satellite image of Hintereisferner (left image) and the elevation bands used for the trend analysis in different shades of blue (right image). The darkest shade marks the lowest elevation while the lightest shade marks the highest elevation.

Table 40: Mann-Kendall test with monthly mean albedo values in at least three years per elevation band to detect interannual trends.

Elevation band	June	July	August	September	October
2413.27	no test	no test	no test	no test	no test
2513.27	no test	no trend	no trend	no trend	no trend
2613.27	no trend	no trend	no trend	increasing (1.000)	no trend
2713.27	no test	no trend	no trend	no trend	no test
2813.27	no test	no trend	no trend	no trend	no test
2913.27	no test	no test	no trend	no trend	no test
3013.27	no test	no test	no test	no trend	no test
3113.27	no test	no test	no test	no test	no test
3213.27	no test	no test	no test	no test	no test

Table 41: Kruskal-Wallis test per elevation band and year to detect significant sub-seasonal albedo differences between June and October.

Elevation band	2013	2014	2015	2016	2017	2018	2019	2020	2021	2022	2023	2024
2413.27	no											
2513.27	no	yes	no	yes	no	no						
2613.27	no	no	no	no	no	yes	no	yes	no	yes	yes	no
2713.27	no	yes	no	no	yes	no						
2813.27	no	yes	no	no	yes	no						
2913.27	no	yes	no	no								
3013.27	no	yes	no									
3113.27	no											
3213.27	no											

B.2.18 Gefrorene Wand Kees

Gefrorene Wand Kees (AT)
 10.08.2024
 Sentinel 2 accessed with GEE

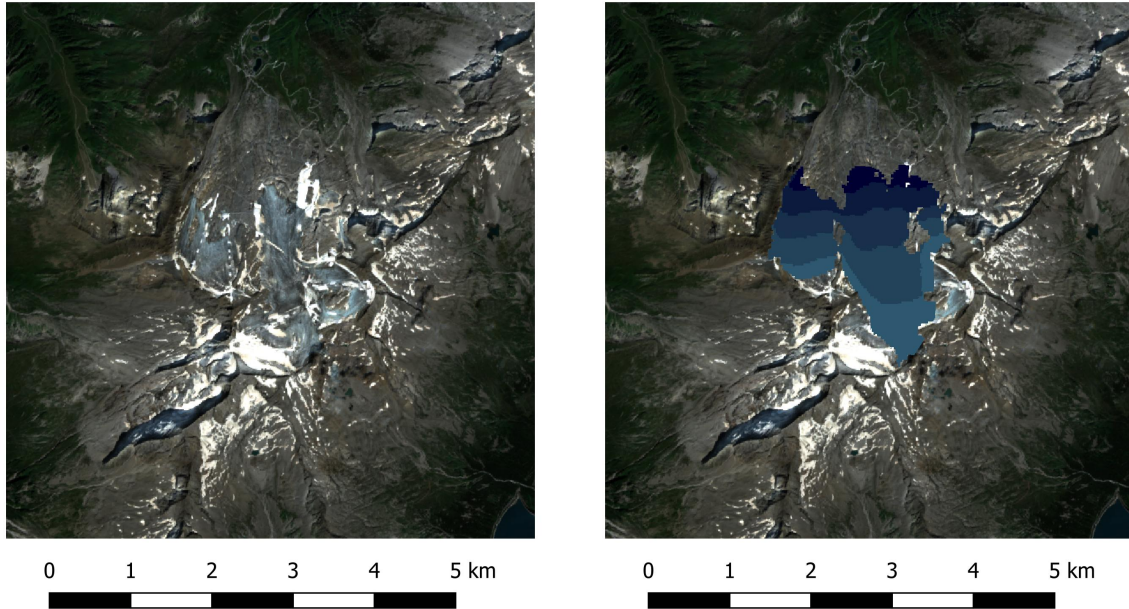


Figure 18: Satellite image of Gefrorene Wand Kees (left image) and the elevation bands used for the trend analysis in different shades of blue (right image). The darkest shade marks the lowest elevation while the lightest shade marks the highest elevation.

Table 42: Mann-Kendall test with monthly mean albedo values in at least three years per elevation band to detect interannual trends.

Elevation band	June	July	August	September	October
2591.47	no test	no test	no test	no test	no test
2691.47	no test	no test	no trend	no trend	no test
2791.47	no test	no test	no trend	no trend	no test
2891.47	no test	no test	no trend	no trend	no test
2991.47	no test	no test	no test	no test	no test

Table 43: Kruskal-Wallis test per elevation band and year to detect significant sub-seasonal albedo differences between June and October.

Elevation band	2013	2014	2015	2016	2017	2018	2019	2020	2021	2022	2023	2024
2591.47	no											
2691.47	no	yes	no									
2791.47	no	yes	no									
2891.47	no	yes	no									
2991.47	no	yes	no									

B.2.19 Hallstätter Gletscher

Hallstätter Gletscher (AT)
 11.09.2024
 Sentinel 2 accessed with GEE

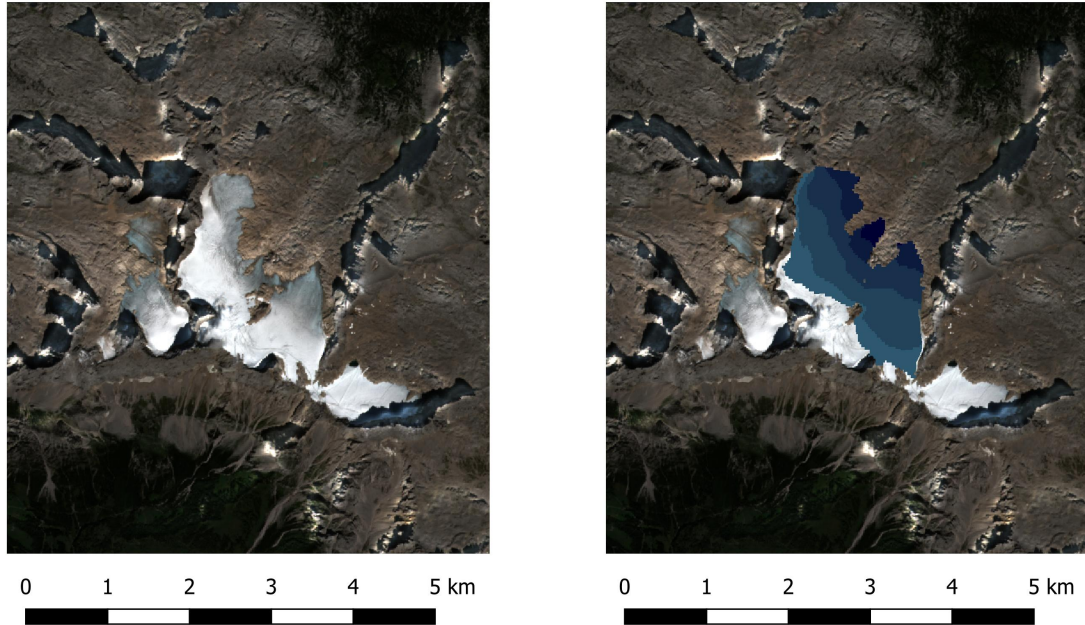


Figure 19: Satellite image of Hallstätter Gletscher (left image) and the elevation bands used for the trend analysis in different shades of blue (right image). The darkest shade marks the lowest elevation while the lightest shade marks the highest elevation.

Table 44: Mann-Kendall test with monthly mean albedo values in at least three years per elevation band to detect interannual trends.

Elevation band	June	July	August	September	October
2190.61	no test	no test	no test	no test	no test
2290.61	no test	no trend	no trend	increasing (0.714)	no test
2390.61	no test	no test	no trend	no trend	no test
2490.61	no test	no test	no test	no trend	no test
2590.61	no test	no test	no test	no trend	no test

Table 45: Kruskal-Wallis test per elevation band and year to detect significant sub-seasonal albedo differences between June and October.

Elevation band	2013	2014	2015	2016	2017	2018	2019	2020	2021	2022	2023	2024
2190.61	no											
2290.61	no	no	no	no	no	yes	no	no	no	yes	yes	no
2390.61	no	yes	no									
2490.61	no	no	no	no	no	yes	no	no	no	no	no	no
2590.61	no											

B.2.20 Umbal Kees

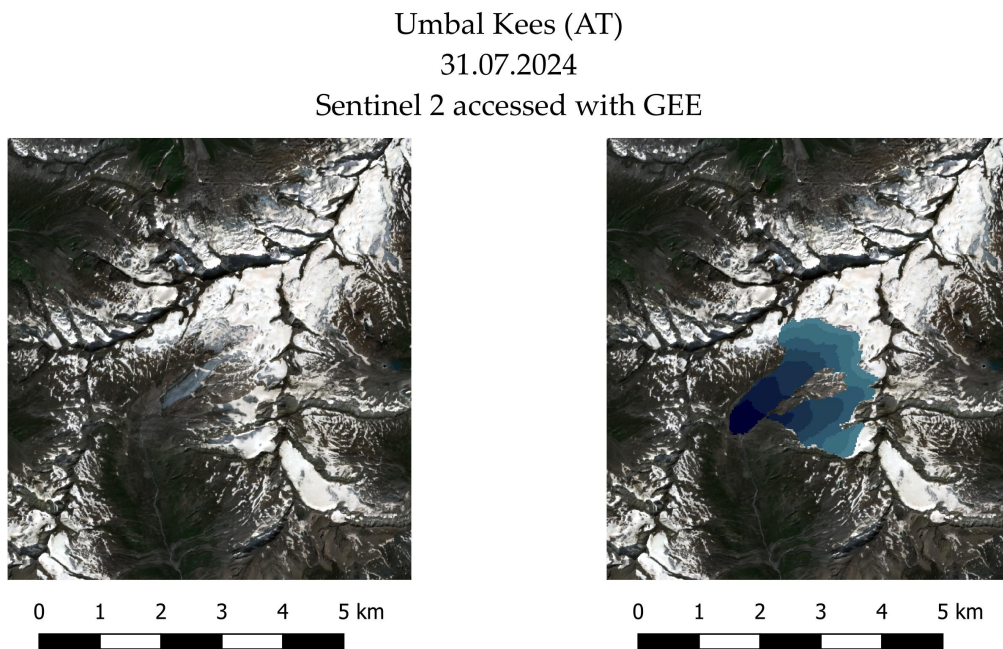


Figure 20: Satellite image of Umbal Kees (left image) and the elevation bands used for the trend analysis in different shades of blue (right image). The darkest shade marks the lowest elevation while the lightest shade marks the highest elevation.

Table 46: Mann-Kendall test with monthly mean albedo values in at least three years per elevation band to detect interannual trends.

Elevation band	June	July	August	September	October
2453.07	no test	no test	no test	no test	no trend
2553.07	no test	no test	no test	no trend	no test
2653.07	no test	no test	no trend	no trend	no test
2753.07	no test	no test	no test	no trend	no test
2853.07	no test	no test	no test	no test	no test
2953.07	no test	no test	no test	no test	no test
3053.07	no test	no test	no test	no test	no test

Table 47: Kruskal-Wallis test per elevation band and year to detect significant sub-seasonal albedo differences between June and October.

Elevation band	2013	2014	2015	2016	2017	2018	2019	2020	2021	2022	2023	2024
2453.07	no											
2553.07	no											
2653.07	no											
2753.07	no											
2853.07	no											
2953.07	no											
3053.07	no											

B.2.21 Schlaten Kees

Schlaten Kees (AT)
31.07.2024
Sentinel 2 accessed with GEE

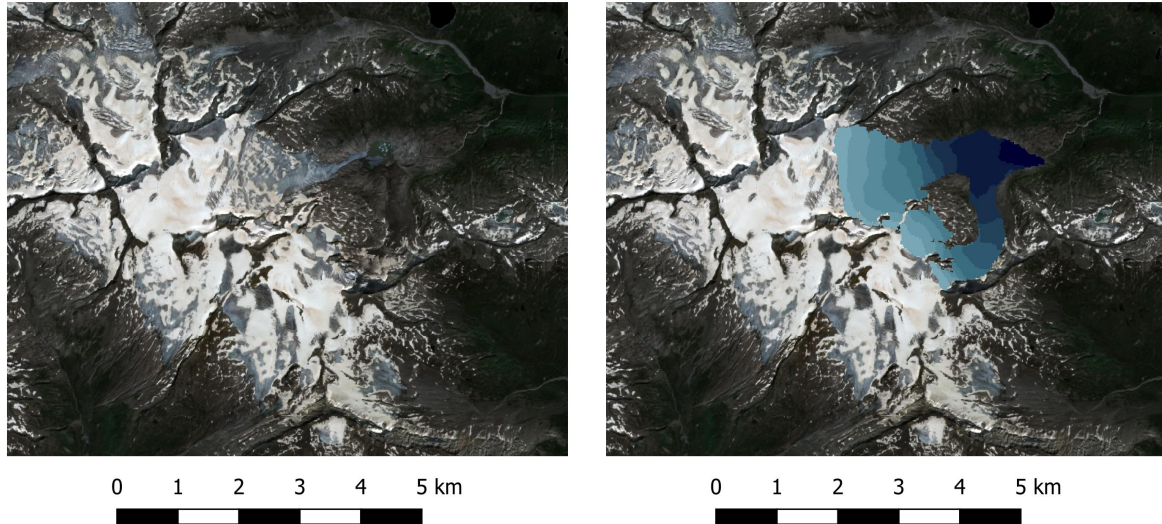


Figure 21: Satellite image of Schlaten Kees (left image) and the elevation bands used for the trend analysis in different shades of blue (right image). The darkest shade marks the lowest elevation while the lightest shade marks the highest elevation.

Table 48: Mann-Kendall test with monthly mean albedo values in at least three years per elevation band to detect interannual trends.

Elevation band	June	July	August	September	October
2132.90	no test	no test	no test	no test	no test
2232.90	no test	no test	no test	no trend	no test
2332.90	no test	no test	no trend	no trend	no test
2432.90	no test	no test	no trend	no test	no test
2532.90	no test	no test	no test	no test	no test
2632.90	no test	no test	no trend	no test	no test
2732.90	no test	no test	no trend	no test	no test
2832.90	no test	no test	no trend	no test	no test
2932.90	no test	no test	no test	no trend	no test
3032.90	no test	no test	no test	no test	no test

Table 49: Kruskal-Wallis test per elevation band and year to detect significant sub-seasonal albedo differences between June and October.

Elevation band	2013	2014	2015	2016	2017	2018	2019	2020	2021	2022	2023	2024
2132.90	no											
2232.90	no											
2332.90	no											
2432.90	no											
2532.90	no											
2632.90	no											
2732.90	no	no	no	no	no	yes	no	no	no	no	yes	no
2832.90	no	no	no	no	no	yes	no	no	no	no	no	no
2932.90	no											
3032.90	no											

B.2.22 Pasterze

Pasterze (AT)
31.07.2024
Sentinel 2 accessed with GEE

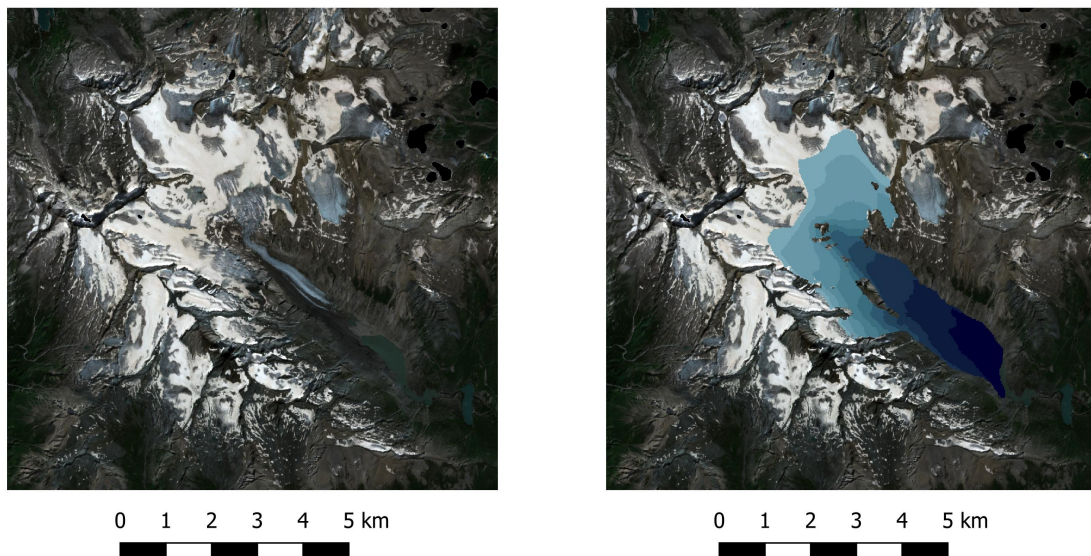


Figure 22: Satellite image of Glacier de la Plaine Morte (left image) and the elevation bands used for the trend analysis in different shades of blue (right image). The darkest shade marks the lowest elevation while the lightest shade marks the highest elevation.

Table 50: Mann-Kendall test with monthly mean albedo values in at least three years per elevation band to detect interannual trends.

Elevation band	June	July	August	September	October
2069.50	no test	no test	no test	no test	no test
2169.50	no test	no test	no test	no trend	no test
2269.50	no test	no test	no trend	no trend	no test
2369.50	no test	no trend	no trend	no trend	no test
2469.50	no test	no trend	no trend	no trend	no test
2569.50	no test	no test	no test	no test	no test
2669.50	no test	no test	no trend	no test	no test
2769.50	no test	no test	no test	no trend	no test
2869.50	no test	no test	no test	no test	no test
2969.50	no test	no test	no test	no test	no test

Table 51: Kruskal-Wallis test per elevation band and year to detect significant sub-seasonal albedo differences between June and October.

Elevation band	2013	2014	2015	2016	2017	2018	2019	2020	2021	2022	2023	2024
2069.50	no											
2169.50	no											
2269.50	no											
2369.50	no	yes	no									
2469.50	no	yes	no	no	yes	no						
2569.50	no											
2669.50	no											
2769.50	no											
2869.50	no											
2969.50	no											

B.2.23 Hochalm Kees

Hochalm Kees (AT)
 21.07.2024
 Sentinel 2 accessed with GEE

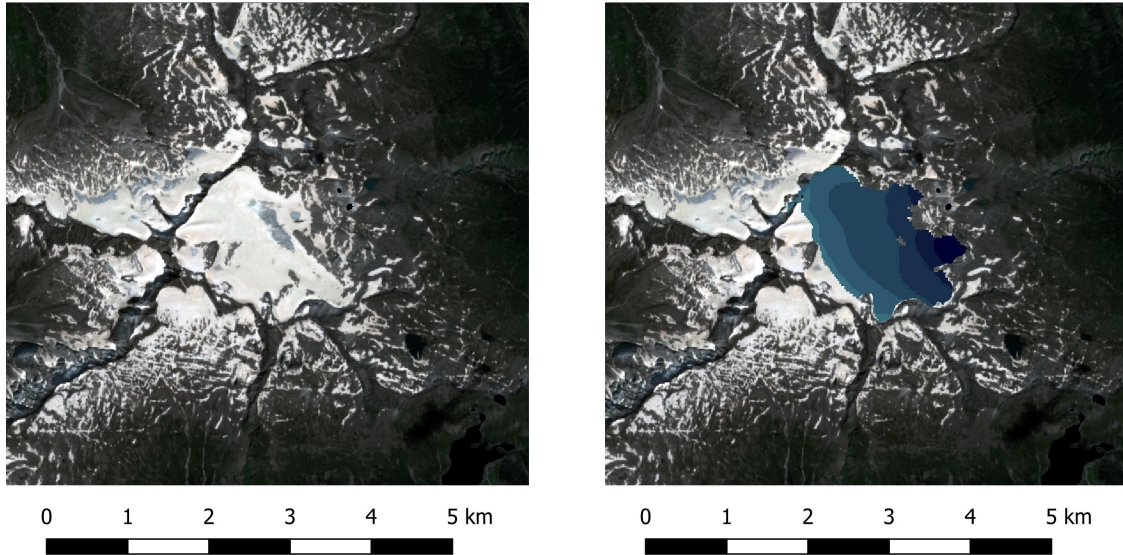


Figure 23: Satellite image of Hochalm Kees (left image) and the elevation bands used for the trend analysis in different shades of blue (right image). The darkest shade marks the lowest elevation while the lightest shade marks the highest elevation.

Table 52: Mann-Kendall test with monthly mean albedo values in at least three years per elevation band to detect interannual trends.

Elevation band	June	July	August	September	October
2511.62	no test	no test	no test	no test	no test
2611.62	no test	no test	no test	no test	no test
2711.62	no test	no test	no test	no trend	no test
2811.62	no test	no test	no test	no trend	no test
2911.62	no test	no test	no test	no test	no test
3011.62	no test	no test	no test	no test	no test

Table 53: Kruskal-Wallis test per elevation band and year to detect significant sub-seasonal albedo differences between June and October.

Elevation band	2013	2014	2015	2016	2017	2018	2019	2020	2021	2022	2023	2024
2511.62	no											
2611.62	no	yes	no									
2711.62	no	yes	no									
2811.62	no	yes	no									
2911.62	no	yes	no									
3011.62	no											

B.3 RQ3: Drivers of albedo change

Table 54: The results of the analysis of the drivers of albedo change for the AWS Weissseespitze/Gepatschferner for the years 2017–2023. This table shows the results for the station in place on the glacier since 2017.

Weissseespitze/Gepatschferner 2017-2023	Kendall's Tau	Significance $\alpha = 0.05$	Strength of Correlation	Number of Observations
Mean Temp. 6h	-0.15	no	low	21
Mean Temp. 12h	-0.10	no	low	21
Mean Temp. 24h	-0.03	no	none	21
Mean Temp. 48h	0.07	no	none	18
Mean Temp. 72h	0.01	no	none	17
Temp. Range 12h	-0.09	no	none	21
Temp. Range 24h	0.10	no	low	21
Temp. Range 48h	-0.08	no	none	18
Neg. Temp. Hours 12h	-	-	-	0
Neg. Temp. Hours 24h	-	-	-	0
Neg. Temp. Hours 48h	-	-	-	0
Nighttime Min. Temp.	-0.09	no	none	21
Nighttime Max. Temp.	-0.03	no	none	21
Zero Deg. Cross. 12h	-0.30	no	moderate	6
Zero Deg. Cross. 24h	-0.21	no	low	7
Zero Deg. Cross. 48h	-0.20	no	low	8
Σ SW Rad. 6h	0.00	no	none	21
Σ SW Rad. 24h	-0.03	no	none	21
Σ SW Rad. 48h	0.16	no	low	21
Σ SW Rad. 72h	0.21	no	low	21
Land Surf. Temp.	-0.67	no	high	4

Table 55: The results of the analysis of the drivers of albedo change for the AWS Glacier de la Plaine Morte for the years 2014–2017. This table shows the results for the station that was on the glacier during the ablation periods 2014–2017.

Glacier de la Plaine Morte 2014-2017	Kendall's Tau	Significance $\alpha = 0.05$	Strength of Correlation	Number of Observations
Mean Temp. 6h	-0.62	yes (0.10)	high	7
Mean Temp. 12h	-0.52	yes (0.15)	high	7
Mean Temp. 24h	-0.43	no	moderate	7
Mean Temp. 48h	-0.43	no	moderate	7
Mean Temp. 72h	-0.62	yes (0.10)	high	7
Temp. Range 12h	-0.33	no	moderate	7
Temp. Range 24h	-0.10	no	low	7
Temp. Range 48h	0.05	no	none	7
Neg. Temp. Hours 12h	-	-	-	0
Neg. Temp. Hours 24h	-	-	-	0
Neg. Temp. Hours 48h	-	-	-	0
Nighttime Min. Temp.	-0.62	yes (0.10)	high	7
Nighttime Max. Temp.	-0.43	no	moderate	7
Zero Deg. Cross. 12h	-	-	-	0
Zero Deg. Cross. 24h	-	-	-	1
Zero Deg. Cross. 48h	-	-	-	1
Σ SW Rad. 6h	-0.33	no	moderate	5
Σ SW Rad. 24h	0.05	no	none	7
Σ SW Rad. 48h	-0.05	no	none	7
Σ SW Rad. 72h	-0.14	no	low	7
Land Surf. Temp.	-0.40	no	moderate	5

C Code

C.1 Google Earth Engine

The base code to access the satellite data through the GEE was provided by Dr. Hendrik Wulf.

The code used to download the Satellite Albedo and Glacier Albedo datasets (Table 5.3) can be accessed **here**. The AWS locations are added as an asset to the code and can be retrieved **here**.

The code to download the Elevation Bands Albedo dataset can be accessed **here**.

C.2 AWS Quality Control

The quality control is based on the **code** by Anna Baldo used for her **Master's Thesis**.

AI Declaration

I hereby declare that artificial intelligence tools have been used during the preparation of this thesis. Specifically, the following tools and methods were used:

- **AI Writing Assistance:** DeepL Write Pro and ChatGPT (4o and 4o-mini) were used to refine the text and improve grammar.
- **Code Assistance:** ChatGPT (4o and 4o-mini) was used to help develop and debug the code used in the Google Earth Engine and for analysis in Python.
- **Literature Search Assistance:** Scite.ai was used to support parts of the literature research by addressing specific questions, identifying relevant sources for particular statements, and verifying whether existing literature backed the conclusions. This complemented the literature already gathered through my own searches.

Date

30 January 2025

Signature



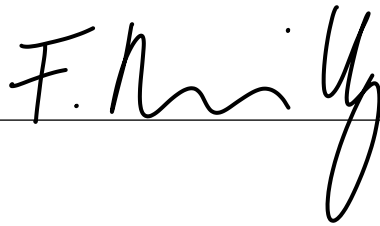
Personal Declaration

I hereby declare that the submitted thesis is the result of my own, independent work. All external sources are explicitly acknowledged in the thesis.

Date

30 January 2025

Signature

A handwritten signature in black ink, appearing to read 'F. Niig', is written over a horizontal line. The signature is cursive and stylized, with a large loop at the end of the last letter.